

University of Kentucky

UKnowledge

Theses and Dissertations--Physics and
Astronomy

Physics and Astronomy

2024

Exploring the Hot and Gaseous Universe from Infrared to X-ray

Chamani Gunasekera

cmgunasekera@uky.edu

Author ORCID Identifier:

 <https://orcid.org/000-0002-4634-5966>

Digital Object Identifier: <https://doi.org/10.13023/etd.2024.129>

[Right click to open a feedback form in a new tab to let us know how this document benefits you.](#)

Recommended Citation

Gunasekera, Chamani, "Exploring the Hot and Gaseous Universe from Infrared to X-ray" (2024). *Theses and Dissertations--Physics and Astronomy*. 122.

https://uknowledge.uky.edu/physastron_etds/122

This Doctoral Dissertation is brought to you for free and open access by the Physics and Astronomy at UKnowledge. It has been accepted for inclusion in Theses and Dissertations--Physics and Astronomy by an authorized administrator of UKnowledge. For more information, please contact UKnowledge@lsv.uky.edu.

STUDENT AGREEMENT:

I represent that my thesis or dissertation and abstract are my original work. Proper attribution has been given to all outside sources. I understand that I am solely responsible for obtaining any needed copyright permissions. I have obtained needed written permission statement(s) from the owner(s) of each third-party copyrighted matter to be included in my work, allowing electronic distribution (if such use is not permitted by the fair use doctrine) which will be submitted to UKnowledge as Additional File.

I hereby grant to The University of Kentucky and its agents the irrevocable, non-exclusive, and royalty-free license to archive and make accessible my work in whole or in part in all forms of media, now or hereafter known. I agree that the document mentioned above may be made available immediately for worldwide access unless an embargo applies.

I retain all other ownership rights to the copyright of my work. I also retain the right to use in future works (such as articles or books) all or part of my work. I understand that I am free to register the copyright to my work.

REVIEW, APPROVAL AND ACCEPTANCE

The document mentioned above has been reviewed and accepted by the student's advisor, on behalf of the advisory committee, and by the Director of Graduate Studies (DGS), on behalf of the program; we verify that this is the final, approved version of the student's thesis including all changes required by the advisory committee. The undersigned agree to abide by the statements above.

Chamani Gunasekera, Student

Dr. Gary J. Ferland, Major Professor

Dr. Christopher Crawford, Director of Graduate Studies

Exploring the Hot and Gaseous Universe from Infrared to X-ray

DISSERTATION

A dissertation submitted in partial
fulfillment of the requirements for
the degree of Doctor of Philosophy
in the College of Arts and Sciences
at the University of Kentucky

By
Chamani M. Gunasekera
Lexington, Kentucky

Co-Directors: Dr. Gary J. Ferland, Professor of Physics & Astronomy
and Dr. Marios Chatzikos, Professor of Physics & Astronomy
Lexington, Kentucky
2024

Copyright© Chamani M. Gunasekera 2024
<https://orcid.org/0000-0002-4634-5966>

ABSTRACT OF DISSERTATION

Exploring the Hot and Gaseous Universe from Infrared to X-ray

Over 90% of baryonic matter in the universe exists as astrophysical plasmas. The gas is often far from thermodynamic equilibrium, so numerical non-equilibrium spectral synthesis simulations are used to understand observations. CLOUDY simulates various physical conditions, providing spectra predictions. This thesis aims to meet the challenge of new observatories like the *JWST* (James Webb Space Telescope) and *XRISM* (X-Ray Imaging Spectroscopy Mission). These simulations are no better than the underlying atomic and molecular database and the fourth chapter details a long-needed update to an evolving database. The predicted spectra are strongly affected by the composition of the gas, which is determined in part by the condensation of certain elements into solid particles called “dust grains”. I showed the effects of self-consistently depleting abundances within H II regions, using the Orion Nebula to demonstrate changes to the spectrum as the degree of dust depletion is altered. Next, an analysis of emergent strong spectral-line intensities is obtained by calculating the abundances into CLOUDY models of a family of extragalactic H II regions. These predictions are then compared with Sloan observations to constrain the depletion strength for a large sample of extragalactic H II regions. These two projects impact the interpretation of *JWST* observations. Finally, I improved the treatment of one-electron doublets, allowing us to simulate observations from the new generation of X-ray microcalorimeters. These advances impact projects using NASA’s most recent orbital observatories, *JWST* and *XRISM*.

KEYWORDS: ISM abundances, ultraviolet, ISM dust, atomic data, X-rays, software simulations

Chamani M. Gunasekera

January 8, 2024

Exploring the Hot and Gaseous Universe from Infrared to X-ray

By
Chamani M. Gunasekera

Dr. Gary J. Ferland
Co-Director of Thesis

Dr. Marios Chatzikos
Co-Director of Thesis

Dr. Christopher Crawford
Director of Graduate Studies

January 8, 2024
Date

Dedicated to my loving parents and husband.

ACKNOWLEDGMENTS

I want to thank my advisors Dr. Gary Ferland and Dr. Marios Chatzikos, who taught me valuable lessons and were kind and supportive throughout my Ph.D. I also want to thank them for their constant encouragement, patience, and guidance. I will always cherish Gary's insights into life and astronomy. I am grateful for Marios' insightful feedback, which pushed me to reach for my full potential. I am grateful to Dr. Peter van Hoof for his help and collaboration during the last years of my Ph.D. I am also thankful to Dr. Renbin Yan and Dr. Xihan Ji for their collaboration and insights during the first project of my Ph.D. I want to thank Dr. Ron Wilhelm for his guidance as my advisor at the beginning of my research career as a graduate student. I want to thank Dr. Christopher Crawford for taking a chance on me and letting me sit in on his class even before I was a graduate student.

My deepest thanks go to my loving husband, Dr. Noah Speeter. Without his love, support, encouragement, and unwavering belief in me through all of the difficult times, I would not have made it this far. I am beyond grateful to my parents, Jeevani and Wimal, for all their sacrifices to give me this opportunity. They are always so supportive of the path I chose and did all they could to provide me with the best opportunities. I am also deeply thankful for my mother-in-law, Lea, and my father-in-law, Bob, for their kindness, and generosity, and for being my family in this foreign country. I also want to thank my cat, Anakin, for keeping me company through the long work days, and for the occasional Zoom cameos.

Lastly, I want to acknowledge support by STScI (HST-AR-15018 and HST-GO-16196.003-A) and NASA (19-ATP19-0188).

TABLE OF CONTENTS

Acknowledgments	iii
List of Tables	vii
List of Figures	viii
Chapter 1 Introduction	1
1.1 Gaseous Nebulae	1
1.1.1 H II Regions	2
1.1.2 Star-forming regions	2
1.2 Observations in various wavelengths	3
1.2.1 How far we have come	3
1.2.2 X-ray	5
1.2.3 UV	6
1.2.4 Optical	6
1.2.5 IR	7
1.3 Predicting Emitted Spectra: Photoionization modeling	7
1.3.1 Physical Processes When Light Interacts with Gaseous Nebulae	7
1.3.2 From Atomic Data to Spectral Line Strengths	8
1.4 CLOUDY	8
Chapter 2 Self-consistent grain depletions and abundances I: The Orion Nebula as a test case	10
2.1 Introduction	10
2.2 Implementation details	10
2.2.1 Calculating Post-Depletion Abundances	12
2.3 Impact on the star forming H II region: Orion Nebula	12
2.4 Modifications to CLOUDY	13
2.4.1 Missing Elements	15
2.4.2 Limits of Depletions	16
2.4.3 Scaling Grains	16
2.5 Conclusions	20
Chapter 3 Self consistent grain depletions and abundances II: Effects on strong-line diagnostics of extragalactic H II regions	23
3.1 Introduction	23
3.2 Photoionization models	24
3.2.1 The Jenkins09 depletion model	24
3.2.2 Input parameters for photoionization models	26
3.3 Impact on a generalized H II region	27
3.3.1 Effect of depletion strength on temperature	28

3.3.2	Effect of depletion strength on emission line intensities	31
3.3.3	Effect of depletion strength & ionization parameter on BPT-like diagnostics	33
3.4	Impact of varying F_* on optical emission-line diagnostics of observed ionized regions	35
3.5	Discussions	39
3.6	Conclusions	41
Chapter 4	Creating a CLOUDY-Compatible Database with CHIANTI Ver- sion 10 Data	43
4.1	Introduction	43
4.1.1	The CHIANTI Database	43
4.2	Ingesting a Fluid Atomic Database	44
4.2.1	A Database Strategy	44
4.2.2	Interpolating Effective Collision Strengths	45
4.2.3	Data Truncation	47
4.3	Testing the Reformatted Database: Effect on CLOUDY Models	49
4.3.1	Time-Steady Model Simulations	53
4.3.2	Time-Dependent Model Simulations	54
4.4	Summary	58
Chapter 5	A $\sqrt{\pi}$ Error in Ly α Optical Depth Normalization	60
5.1	Introduction	60
5.2	Line transfer in dusty media	60
5.3	Lyman α Escape & Destruction Probability	61
5.4	Changes to Spectra	62
5.5	Summary	62
Chapter 6	Resolving One-electron fine-structure Lyman lines: Preparing Cloudy for high-resolution X-ray in the microcalorimeter era.	64
6.1	Introduction	64
6.2	One-electron Doublets in Cloudy	64
6.2.1	Radiative transfer	66
6.3	Energy Calculations	66
6.3.1	Fine-Structure Splitting	66
6.3.2	nP Level Energy Corrections	67
6.4	Incorporating into Cloudy	68
6.4.1	Energy Resolution & Accuracy	68
6.4.2	Transition Probabilities	70
6.4.3	Doublet Line Intensities	71
6.4.4	Escape & Destruction Probabilities	73
6.5	Results of Simulating high-resolution X-ray spectra	74
Chapter 7	Conclusions	76

Appendices	78
Appendix A: Bethe Logarithm	78
Appendix B: Perseus Photoionization Model	79
Appendix C: Burgess and Tully Scaling	79
Appendix D: CHIANTI File Formats	80
.	81
Bibliography	82
Vita	95

LIST OF TABLES

2.1	Calculated depletion parameters for missing elements from Jenkins09. . .	16
3.1	Reference abundance sets $(X_{gas}/H)_{\odot}^{(2003)}$ (Lodders, 2003), $(X_{gas}/H)_{\odot}^{(2009)}$ (Lodders and Palme, 2009), and GASS-Grevesse et al. (2010) are all available to be used with the CLOUDY grain depletion command. The models for this study have used the GASS abundances as the reference set. . . .	25
3.2	Photoionization model parameters	28
4.1	Wavelengths of electron-excitation transitions in the Ch10 database compared with the values in the Ch7 database.	51
4.2	A list of the spectral lines that differ in intensity (the normalization line intensities used are $H\alpha$ & $H\beta$) due to collisional data changes between Ch7 and Ch10, as calculated with the time-steady simulations in the CLOUDY test suite.	51
4.3	A list of the spectral transitions that differ in log luminosity due to collisional data changes between Ch7 and Ch10, as calculated by time-dependent test simulations in CLOUDY.	52
D1	Format variation from Ch10 to Ch7.	80

LIST OF FIGURES

1.1	Image (a) and spectrum (b) of the Orion Nebula. The image was taken by the Hubble Space Telescope.	2
1.2	Structure of ionized, neutral and molecular gas near ionizing source. . . .	3
1.3	An example BPT diagram obtained from de Souza et al. (2017), showing SDSS data. My adaptation of these diagnostic diagrams are in Figure 3.3 and Figure 3.4.	4
2.1	Interstellar element depletion scale factors $[X/H]_{F_*}$ (top panel) and predicted line strength ratios for the Orion nebula typically found in BPT plots subtracted by its own value at $F_* = 0.4$ (bottom panel) vs. depletion strength F_* . The red dashed line on the top panel represents the number of heavy element atoms locked in dust grains relative to the number of H atoms as a function of F_* . All data presented in this plot is obtained by output from CLOUDY. Note that the normalization of line ratios at $F_* = 0.4$ is to present the data in a way that is easily visually comparable. Furthermore, here grains are kept at their default Orion grain abundance.	14
2.2	Predicted line strength ratios for the Orion nebula typically found in BPT plots vs. depletion strength F_* . All data presented in this plot is obtained by output from CLOUDY. This is the same data that appears in the bottom panel of Figure 2.1, except without normalizing to intensities at $F_* = 0.4$.	17
2.3	Temperature profile of the H^+ layer across the $H\ II$ region. Panels from left to right indicate temperature profile with increasing depletion strength F_* . The dashed line corresponds to the models where grains were scaled as in Figure 2.2, and the solid line corresponds to grain abundance kept at CLOUDY's default Orion grain abundance.	18
2.4	IR emissions by dust in the H^+ layer across the $H\ II$ region, as grain abundance is scaled with F_* (solid line) and kept at default Orion grain abundance (dashed line), both relative to the $H\alpha$ line.	18
2.5	(a) Depletion strength F_* vs. color excess $E(B - V)$ per hydrogen column density N_H . (b) Color excess $E(B - V)$ vs. hydrogen column density N_H . Both plots show the same data. The data are obtained from the lines of sight listed in Jenkins09.	19

3.1	<p>Temperature profile of the cloud at varying metallicity values (listed on the right edge of the figure), ionization parameters (listed on the top edge of the figure), and depletion strength. Each line jumps by 0.125 change in F_*. The depth is taken from the illuminated face at 0 cm, increasing out to the H ionization front. The ionization front is seen where the temperature profile drops off. In the bottom-left most panel, the second bump in the profile indicates the He ionization front. Despite the x-axis scale, this figure can be related to the Strömngren length via the ionization parameter, see Equation (3.6).</p>	29
3.2	<p>Top panel: the depletion scale factor calculated from the Jenkins09 depletion model, and multiplies the reference abundance in logarithm scale as a function of F_*. The depletion scale factor D_X is defined using $(X_{gas}/H)_{F_*} \equiv (X/H)_\odot D_X$. In the case of the Jenkins09 depletion model we have that, $\log(D_X) = B_X + A_X(F_* - z_X)$. Bottom three panels: line ratio intensities obtained from the CLOUDY model predictions as a function of F_*, for the three different metallicity values indicated. These line ratios correspond to fixed ionization parameter at $\log(U) = -3.0$.</p>	32
3.3	<p>BPT-like plots using the spectral line ratio predictions for models of varying $(O/H)/(O/H)_\odot$ (top to bottom rows of plots), varying depletion strength F_* (coloured lines), and varying U (black lines) in [N II]-, [S II]-, and [O I]-BPT diagrams. The line ratios for varying F_* are the same ones depicted in Fig 3.2, and the colour coding for models of varying F_* is the same as that in Fig 3.1. Ghost plots of the reference metallicity (middle row) plots are included in the background of the highest (bottom row) and lowest (top row) metallicity plots to facilitate comparisons.</p>	34
3.4	<p>Photoionization models with $F_* = 0.0, 0.5, \text{ and } 1.0$ plotted in the [N II]-, [S II]-, and [O I]-BPT diagrams. The model grids are plotted by independently varying the metallicity and the ionization parameter. A sample of spatially resolved data from MaNGA is shown in the background, with the SF regions (identified by combining the [N II]- and [S II]-BPT diagrams) coloured from yellow to green, and the rest of the ionized regions coloured from white to black. We also plot demarcation lines from Kewley et al. (2001) (solid black lines), Kewley et al. (2006) (solid black lines), Kauffmann et al. (2003) (dashed black line), and Stasińska et al. (2006) (dash-dotted black line) for comparison.</p>	39

3.5	Distribution of MaNGA data in a specific projection (P_1 - P_2 projection; Ji and Yan (2020)) of a three-dimensional line ratio space. Here N2, S2, and R3 stand for $\log([\text{N II}]/\text{H}\alpha)$, $\log([\text{S II}]/\text{H}\alpha)$, and $\log([\text{O III}]/\text{H}\beta)$, respectively. The two axes P_1 and P_2 are linear combinations of N2, S2, and R3. The projection was constructed in a way that makes the data locus and the model appear nearly edge-on. The model grids are also projected into this plane but are first interpolated and then truncated so that only the parts of the models that cover the middle 98 percent of the data along the third dimension perpendicular to both P_1 and P_2 axes are shown. <i>Left:</i> Model grids with different F_* values. <i>Right:</i> A model grid with $F_* = 0.5$ but without depletion of sulfur onto dust grains. In addition, different from the models in the left-hand panel (whose parameters other than F_* are summarized in Table 3.2), it adopts an N/O versus O/H relation derived by Schaefer et al. (2020).	40
4.1	Each panel presents the collisional data of an example transition. The black plot line indicates the original data from the Ch10 database. The purple plot line indicates the evenly spaced collisional data interpolated from the original Ch10 transition. The pink plot line shows our best-fit results of the original Ch10 collision strengths.	47
4.2	Top panel: distribution between the interpolated collision strength χ error and the number of spline points used in the interpolation, per transition. The red line in the top panel indicates the fit error limit that is set in our script that converts Ch10 format to Ch7. Middle panel: histogram of interpolated collision strength fit errors. Bottom panel: histogram of the number of spline points used in the interpolation.	48
4.3	Cross-correlation between the recalculated collision strengths $>10^{-2}$ and the original Ch10 collision strengths $>10^{-2}$, both converted to physical space. The blue dashed line in the top panel is the $y = x$ plot, in our case it represents the recalculated Υ and original Υ that are in perfect agreement. The bottom two panels show relative deviation, which is the difference between each recalculated Υ and original Ch10 Υ , and divided by the latter. The red dashed line in the middle panel indicates a relative deviation of 10%. The data contained in the middle and bottom plots are the same, only differing in the scaling of the y-axis (log vs. linear).	50
4.4	Collision strength-temperature profiles in BT space for the botched transitions in the <code>pn_paris</code> and <code>nlr_paris</code> test simulations.	54
4.5	CLOUDY outputs of the <code>pn_paris</code> and <code>nlr_paris</code> test simulations.	55
4.6	Collision strength against temperature in BT space for botched Fe XII, Fe XIII, and Fe XIV electron transitions in the <code>time_cool_cd</code> test simulation. Green plot lines indicate equally spaced temperature grid data interpolated from the original source of the Ch10 data. The original data show all but the last data point, which corresponds to the point at the high-temperature limit.	57

4.7	Temperature as a function of time (in black), and total cooling as a function of temperature (in blue). Dashed lines indicate the output of the simulation utilizing atomic data from the Ch7 database, and solid lines indicate the output of the simulation utilizing the reprocessed Ch10 database. The black circles indicate the dominant coolant at that temperature and the following temperatures up to the next black circle. Free-free cooling is denominated by ‘FFc’.	58
5.1	A contour plot of H Ly α line intensity predicted by C23.01 relative to the same quantity from C23.00, for the baseline model <code>orion_hii_open.in</code> in the CLOUDY test suite. The ratio of ionizing photon flux $\phi(H)$ to hydrogen density $n(H)$ is effectively the ionization parameter U . The lower-right corner of the panels corresponds to high U , and the upper-left corner is low U .	63
6.1	<i>Top:</i> Contour plot of energy separation between the nP $_{1/2}$ and nP $_{3/2}$ levels. The white plot lines indicate the spectral resolution of the current microcalorimeter mission <i>XRISM</i> (R \sim 5 eV) and future mission <i>Athena</i> (R \sim 2.5 eV). <i>Bottom:</i> Contour plot showing the resolving power required to distinguish between the 2S $_{1/2}$ –nP $_{1/2}$ and 2S $_{1/2}$ –nP $_{3/2}$ transition energies, where $E_{2S_{1/2}} = 0$. For both plots the y-axis is the range of principle quantum numbers used in CLOUDY calculations, and the x-axis is the range of elements with atomic number Z used.	69
6.2	Energy scale accuracy of the updated nP $_{1/2}$ and nP $_{3/2}$ levels for H-like species in CLOUDY, using NIST as the authority. The expected accuracy for <i>XRISM</i> is 0.5 eV, which is well above those for any of our new H-like nP $_j$ energy calculations. The dots indicate the accuracy for $j = 1/2$, and crosses indicate those for $j = 3/2$. The colors going from purple to green indicate increasing principle quantum number n .	70
6.3	Energy level diagram showing the fine-structure levels of angular momentum quantum number $l > 1$. Note, the level ordering is consistent with energy levels of lighter H-like species. For higher- Z 1-electron atomic species, energy of level 2P $_{1/2}$ is higher than that of 2P $_{3/2}$, although this swap is not predicted in Yerokhin and Shabaev (2015).	71
6.4	(a) The ratio between transition probability (A_{ul}) for the 1S–2P transition to collisional rate coefficients (q_{ul}) for j-changing collisions as a function of temperature for four different H-like ions. <i>Top panel:</i> ratio involving Einstein A values for 2P $_j = 3/2$, <i>bottom:</i> for $j = 3/2$. The dashed lines indicate the ratio involving proton-impact j-changing collisions (indicated with q_{ul}^p), the solid lines are for electron-impact collisions. (b) Transition rate coefficient as a function of temperature. The dashed, dotted, and solid lines indicate values corresponding to proton-impact 2–4 transition, electron-impact 2–4 transition and electron-impact 1–2 transition, respectively. The electron-impact data was obtained from Mao et al. (2022) and the proton-impact values from Zygelman and Dalgarno (1987).	72

6.5	Cloudy predicted X-ray spectra of the Perseus Cluster. <i>Red</i> :Spectra simulated using the C23.01 release of CLOUDY that does not have H-like fine-structure splitting of the nP levels. <i>Black</i> :Spectra simulated using the current development version of CLOUDY with the one-electron fine-structure Lyman doublets.	75
1	Log fit of the exponential of the Bethe logarithm values presented in Drake and Swainson (1990) for orbital angular quantum number $l = 1$	78

Chapter 1 Introduction

Most of the baryonic matter present in the Universe exists in the form of astrophysical plasmas. Astrophysical plasmas are generally present in extreme environments, such as strong magnetic fields, extreme gravity or explosive forces. When matter is heated up it gets ionized and forms plasmas. In the young Universe, much of the baryonic mass of a galaxy was found in the gas of the interstellar medium (hereafter ISM). The ISM constitutes the gas and dust found between stars. About 91% by number of the ISM gas is hydrogen, followed by helium making up 8.9%, and the remaining 0.1% is the heavy elements.

As galaxies evolve, stars are born out of the gas and dust in the ISM, making it one of the most important components of a galaxy. The baryonic matter in galaxies is also what makes them visible to us. When stars emit light, it passes through the interstellar region surrounding the star before it reaches us here on Earth (this light also passes through the Galactic ISM, which has to be corrected for). During this course, the material in the ISM absorbs and scatters the starlight. So, understanding the physical processes within the ISM can help reveal information about the stars it surrounds and the galaxy it resides in.

1.1 Gaseous Nebulae

Gaseous nebulae, also known as emission nebulae, are luminous objects in the sky consisting of ionized gas and dust. Nearly all gaseous nebulae are ionized by energetic radiation from hot stars near or in the nebulae, and so these nebulae emit in the full range of the electromagnetic spectrum. Both strong H I recombination lines, H β and H α are characteristic features of their. Additionally, spectra of emission nebulae are dominated by forbidden lines of abundant ions such as [O III] $\lambda\lambda$ 4959,5007, [N II] $\lambda\lambda$ 6548,6583, [S III] $\lambda\lambda$ 9069,9523, and [O II] $\lambda\lambda$ 3726,3729. These emission lines are essential for classifying the type of gaseous nebula and can be used to determine other physical parameters of the nebulae.

Gaseous nebulae can be classified into two classical types, H II regions and planetary nebulae. The former will be discussed in the sub-section below. The latter is an isolated nebulae that are shells of gas ejected from red giant stars (Osterbrock and Ferland, 2006). Planetary nebulae consist of gas that is more highly ionized than H II regions, and therefore contain stronger [O III] and [Ne III] lines. Besides these two types, supernova remnants and active galactic nuclei (AGN) are also photoionized nebulae that produce emission-line spectra.

Many gaseous nebulae contain dust grains. As the gas evolves, atomic species in the nebulae transition out of their gas phase and condense onto dust grains. This process is termed grain depletion. Dust grains cause reddening and extinction of the starlight passing through the nebulae, by absorbing the incident starlight and emitting IR radiation. Line photons emitted by the gas can also be lost by grain absorption.

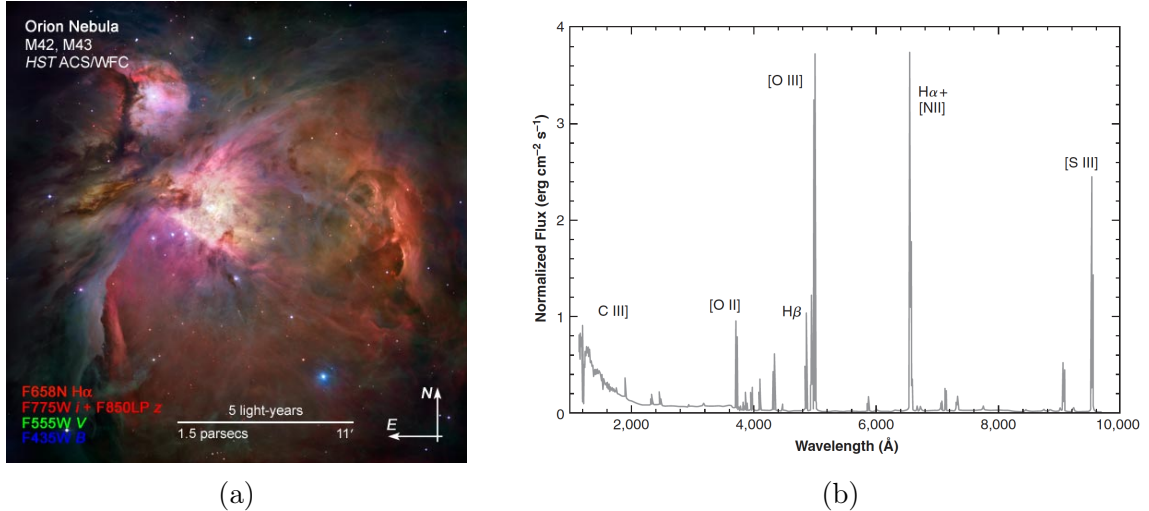


Figure 1.1: Image (a) and spectrum (b) of the Orion Nebula. The image was taken by the Hubble Space Telescope.

1.1.1 H II Regions

H II regions, also known as diffuse nebulae, are regions of interstellar matter found near stars of high surface temperature $3 \times 10^3 \text{ K} < T_* < 5 \times 10^4 \text{ K}$, i.e. O, B type stars (Spitzer, 1978). A typical HII region has temperatures $\sim 10^4 \text{ K}$ and densities $0.3 < n_H < 10^4 \text{ cm}^{-3}$ (Draine, 2011). The gas in these regions is photoionized by the energetic radiation emitted by their exciting stars. Thus, this gas contains ionized H, singly-ionized He, and single or doubly ionized heavy elements, and typically emits in the optical and infrared regions. Among those features mentioned previously, some of the most notable emission features from H II regions are [O III] λ 5007, [N II] λ 6583, [S II] λ λ 6716,6731, H β , H α (Osterbrock and Ferland, 2006). One of the most well-studied H II regions is the Orion nebula. Figure 1.1 shows an image of the Orion Nebula taken with the Hubble Space Telescope, showing its brightly lit center.

As starlight passes through the H II region, there eventually comes a point far enough from the illuminated face of the cloud where the remaining photons no longer have enough energy to ionize H. This boundary is called the H-ionization front. Beyond this boundary is the neutral medium, also known as the H I region, where the gas has temperatures drop to $T \leq 10^{3.7} \text{ K}$. Beyond the neutral medium, we encounter the molecular cloud, where much of the hydrogen is in H_2 molecules. This gas has temperatures of $10 \leq T \leq 50 \text{ K}$, and $10^2 \text{ cm}^{-3} < n_H < 10^6 \text{ cm}^{-3}$ (Draine, 2011). So, it is heavily obscured by dust. Figure 1.2 shows an illustration of these different nebular regions. Much of the radiation reaching these clouds is either reflected back towards the illuminated face of H II regions or absorbed.

1.1.2 Star-forming regions

Star-forming galaxies have optical spectra dominated by emission lines from H II regions. However, large galaxies can have emission lines originating from multiple

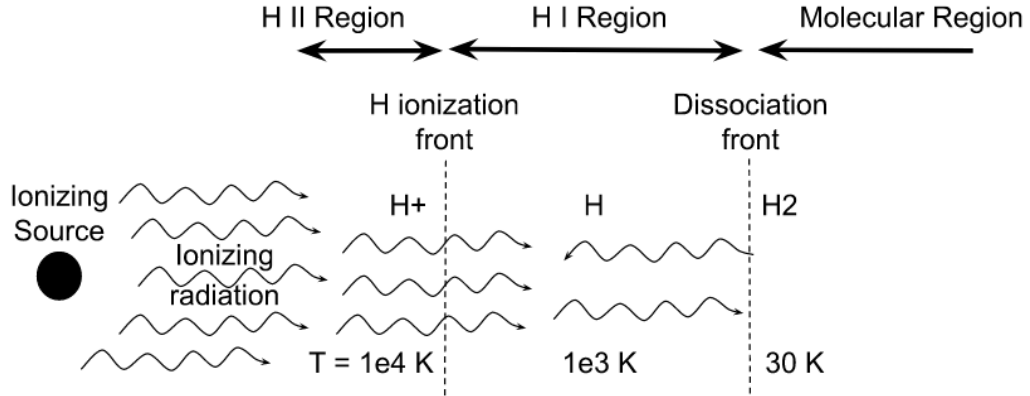


Figure 1.2: Structure of ionized, neutral and molecular gas near ionizing source.

different emitting regions, and disentangling this can prove difficult. The overall spectra even in star-forming galaxies can be dominated by emission lines from AGN. An AGN typically consists of a central black hole that accretes material, which results in a radiation field that is much harder than the standard hot star. So the gas photoionized by radiation from AGN are in the X-ray regime, with strong emission lines from ions at high ionization stages such as C IV and Ne V.

In order to distinguish between these different types of galaxies, Baldwin, Phillips & Terlevich developed a diagnostic diagram that compares the relative strengths of pairs of strong emission lines (Baldwin et al., 1981; Veilleux and Osterbrock, 1987; Ho et al., 1997, hereafter BPT diagram). The typical BPT diagram compares $[\text{O III}]\lambda 5008/\text{H}\beta$ vs. $[\text{N II}]\lambda 6585/\text{H}\alpha$. Since $[\text{O III}]\lambda 5008$ is one of the strongest emission lines from H II regions, BPT diagrams are potent tool in studying H II region spectra. Figure 1.3 shows a typical example of a BPT diagram obtained from de Souza et al. (2017). This figure shows how based on the region of the diagram that, an observed pair of $[\text{O III}]$ and $[\text{N II}]$ lines fall on, helps determine the type of object in consideration.

1.2 Observations in various wavelengths

1.2.1 How far we have come

“Nebula” is the Latin word for “cloud”. Even ancient Arabic astronomers used the Arabic word for cloud to describe nebulae. Before the use of telescopes, naked-eye observations were not able to distinguish nebulae from other extended objects in the sky. So, nebulae were blurry patches of light distinct from stars, which referred to anything between distant galaxies and/or star clusters (Hafez, 2010). Dating back to around 964 AD, Abd Al-Rahman Al-Sufi was the first known author to describe a true nebula in his book “Book of the Fixed Stars” (Hafez, 2010). He was an Iranian astronomer who drew his work from, Alexandrian astronomer, Claude Ptolemy’s “Almegeest” (Ferrière, 2001). The “Almegeest” is the first known astronomical treatise, dating back to around 137 AD. Al-Sufi was part of the court of the emir of his time and

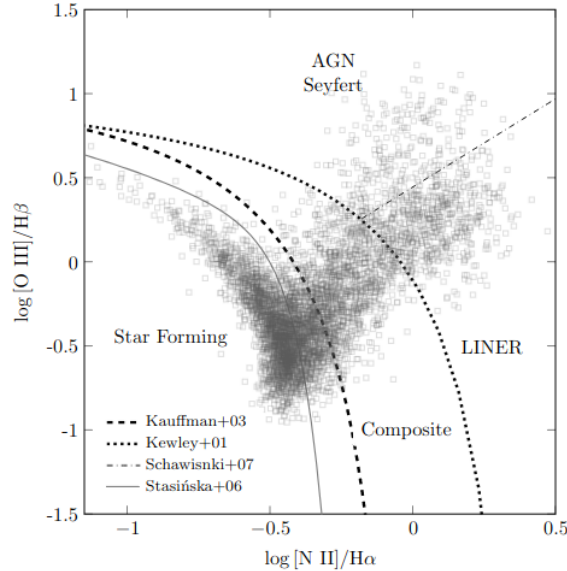


Figure 1.3: An example BPT diagram obtained from de Souza et al. (2017), showing SDSS data. My adaptation of these diagnostic diagrams are in Figure 3.3 and Figure 3.4.

worked on ancient Greek astronomical texts. He became an influential astronomer who greatly contributed to the development of astronomy as a science.

The earliest observation of a nebula using a telescope was of the Crab nebula. Supposedly, naked-eye sightings of the Crab Nebula date back to 1054, by Chinese and Japanese astronomers who mistook it for a star (Mayall, 1939). The object had disappeared in the middle of the 11th century, and subsequently, the records of its sighting did not receive any attention. This nebula is a supernova remnant, and the bright apparition noted in 1054 was the corresponding supernova explosion. However, the credit for its discovery is often awarded to English physician, John Belvis, in 1731.

In 1610, Nicolas-Claude Fabri de Peiresc, a prominent French astronomer, became the earliest known observer of the Orion Nebula, using a refracting telescope (Muench et al., 2008). Upon his first observation, he was apparently surprised to see a “small illuminated cloud” surrounding the central star of the sword of the Orion constellation (Harrison, 1984). The Orion nebula is now one of the most well-studied H II regions, having revealed information about star and planetary formation, gas photoionization, gas dynamics, and much more.

By the 18th century, astronomers were compiling lists of astronomical objects, including of nebulae. In 1774, french astronomer Charles Messier and his assistant Pierre Méchain, published a catalogue of non-comet objects in their “Catalogue of Nebulae and Star Clusters”, which included the Crab Nebulae as M1 (Messier, 1781). In 1786, siblings Caroline and William Herschel published “The Catalogue of One Thousand New Nebulae and Clusters of Stars” (Herschel, 1786). Their catalogue continued to be updated over the years, and by 1802, their final catalogue had about 2500 objects (Herschel, 1802). Herschel’s catalogue classified nebulae into galactic

and non-galactic, and further categorized galactic nebulae into diffuse and planetary nebulae, while there were spiral, elongated, globular and irregular non-galactic nebulae.

Following Herschels' revolutionary catalogue, astronomers began to distinguish nebulae from other astrophysical objects using their observed spectra. In 1864, British astronomer, Sir William Huggins, studied the spectra of stars and nebulae and paved the way for astronomical spectroscopy. His work shows that the spectra of some nebulae matched the emission spectra of a gas, while others had a continuous spectrum similar to that of a group of stars (Huggins and Miller, 1864; Huggins, 1868). Subsequently, Edwin Hubble, amongst his other famous works, extensively studied the observed spectra of galactic and extragalactic nebulae. He found that the radiation from galactic nebulae is a re-emission of starlight illuminating the nebulae (Hubble, 1922).

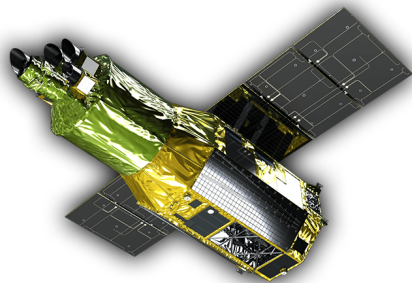
1.2.2 X-ray

Astrophysical plasmas that are heated to about $\geq 10^6$ K emit in the X-ray region of the electromagnetic spectrum. Plasmas are heated to such high temperatures by being exposed to extreme environmental conditions, such as strong magnetic fields from neutron stars, extreme gravity like that from black holes in AGN or explosive forces by supernovae (Raymond and Smith, 1977). So X-ray studies of gaseous nebulae provide information on the most energetic processes in our Universe.

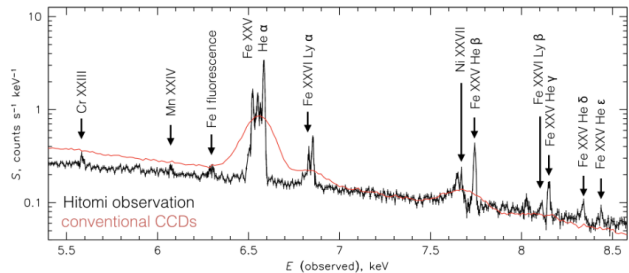
The Earth's atmosphere absorbs X-ray radiation, so X-rays cannot be observed from the ground. The first X-ray missions used sounding rockets, which provided little detail of the X-ray emitting source. With the development of proportional counters, such as in *Uhuru* and *Einstein*, the spectral resolution of X-ray observations increased to $R = E/\Delta E \sim 10$ (Giacconi et al., 1971). *Uhuru* detected over 300 X-ray sources during its three-year mission, including the first X-ray source outside of our own galaxy. *ROSAT* expanded the number of known X-ray sources to 125,000.

As technology developed, and greater spectral resolutions of X-ray observation were achieved, greater strides in our understanding of X-ray emitting plasmas were made. The CCD cameras and grating spectrometers in *Chandra X-ray Observatory* and *XMM-Newton* provided a spectral resolution of about $R > 300$ at 0.4 – 2.5 keV (Garmire et al. (2003); Strüder et al. (2001)). The improved resolutions led to detailed studies of formation and evolution of galaxy clusters, heavy-element abundance measurements in the afterglow of gamma-ray bursts (GRB) and supernova remnants, spectra of AGN, and so much more (Weisskopf et al., 2002; Polletta et al., 2007).

The state-of-the-art in X-ray detection, to date, is microcalorimeter technology. A microcalorimeter detector's ability to measure the energy of a single X-ray photon, is what makes this technology highly anticipated in X-ray astronomy. It yields an unprecedented spectral resolution over a wide range of X-ray energies. The first mission with this technology onboard, *Hitomi*, crashed in 2016 having only observed the Perseus galaxy cluster (Takahashi et al., 2018). This single observation revealed the potency of using microcalorimeter observations to conduct X-ray studies. The



(a) An image of the *XRISM* telescope.



(b) Spectrum from the core of Perseus, observed with *Hitomi* (in red) overlaid with an observation from Suzaku X-ray mission. Suzaku hosted a CCD spectrometer and was launched in 2005.

second attempt at a mission with this technology was launched earlier this year, *XRISM* (Tashiro, 2023). Figure 1.4a shows an image of *XRISM* telescope.

1.2.3 UV

Emission lines from ions in high-ionization stages in warm ionized gas, absorption lines from a broad range of atoms/ions, and continua from atomic processes can all be found in the UV regime (Osterbrock and Ferland, 2006). Hence, UV spectroscopy is a useful tool for determining the chemical composition, density, and temperature of the ISM. Since the Earth's atmosphere absorbs most light at UV wavelengths, UV observations must be made in space. Both *HST* and *FUSE* (Far UV Spectroscopic Explorer) have been very successful UV telescopes.

1.2.4 Optical

Emission lines from warm ionized gas, absorption lines from ions/atoms in the ISM, continua from atomic process, and continua from scattered starlight all appear in the visible region of the electromagnetic spectrum (Osterbrock and Ferland, 2006). Optical astronomy is the primary method by which to study the gaseous contents of galaxies. The first telescope invented, an optical refracting telescope, is credited to spectacle maker Hans Lippershey, in the Netherlands in 1608 (Rudd, 1993). Having such a rich and extensive history, there are many optical observing facilities available today.

The Hubble Space Telescope (*HST*) is one of the largest and most versatile space-based telescopes, launched in 1990. It remains in operation today, and mainly observes in the ultraviolet regime, although it also has instruments that observe in optical and near-IR. Since *HST* is in space, it can reach higher resolutions with a smaller aperture than any ground-based telescope, making it highly competitive in conducting optical observations. Some notable ground-based optical telescopes are the Very Large Telescope (VLT), the Giant Magellanic Telescope GMT, and Keck. A highly anticipated ground-based optical telescope, the Simonyi Survey Telescope

(LSST), at the Rubin Observatory, will be launching soon. It is projected to host the largest camera ever built for astronomical observations.

1.2.5 IR

Emission lines from ions/atoms with a wide range of ionization potentials, molecular rovibrational transitions & continua from atomic processes, and thermal grain emission can all be observed in IR wavelengths (Osterbrock and Ferland, 2006). Additionally, dust grains in astrophysical gases absorb more in the optical wavelengths than in IR, making IR observations an especially powerful tool in probing dust-obscured objects.

In 1830, astronomers initiated efforts to detect IR radiation from astronomical sources other than the Sun. By 1983, the first all-sky survey in IR, the Infrared Astronomical Satellite (*IRAS*) was launched (Neugebauer et al., 1984). *IRAS* discovered many IR emitting objects, including comets and asteroids. *SOFIA*, the Spitzer Space Telescope, and *JWST* are all important modern-day IR telescopes. The high sensitivity and resolution of *JWST*, makes it an especially powerful tool in probing high-redshift environments, and also in probing objects enshrouded in dust.

1.3 Predicting Emitted Spectra: Photoionization modeling

1.3.1 Physical Processes When Light Interacts with Gaseous Nebulae

Starlight incident on the cloud is absorbed and/or scattered by the material in the gas. Since most ionizing sources radiate in UV or X-rays, the incident photons have sufficient energy to photoionize the gas. Recombinations of electrons with ions counterbalances the photoionizations, thus setting an ionization equilibrium at each point in the nebula. This is parameterized using the ionization parameter U , which is the ratio of ionizing photon flux to electron density of the cloud. The finite source of ionizing photons determines the size of the ionized region. The overall structure of the photoionized cloud is thus determined by the photoionization cross-section and recombination coefficients for the ionized atoms. Additionally, photoionization is the primary heating mechanism, while recombinations along with radiation from the nebula cools the gas. Thus the balance between photoionizations and recombinations also determines the thermal balance, and, consequently the temperature of the ionized cloud.

Supplementary to the stellar radiation field, radiative processes in the gas also produce a diffuse component of the total radiation field from a cloud. This diffuse field can further be broken down into line radiation, and continuum radiation. Line radiation is produced in recombinations leading to bound-bound transitions, or in collisional excitation of atoms/ions in the gas. Recombination lines of H I, He I, and He II are all characteristic features of nebulae spectra. Electron recombinations to excited levels of H^+ lead to radiative transitions by the atom as it cascades down to the ground level, resulting in the characteristic $H\alpha$, $H\beta$ recombination lines. Electron- and proton-impact collisions with atoms/ion excite levels within a few volts of the

ground level, leading to radiative decays which produce collisionally excited line photons. In ordinary optical nebulae, these low-lying excited levels of abundant ions come from the same electron configuration as the ground level, and violates the parity selection rule. Thus, historically, these types of nebular lines were called forbidden lines.

The emitted radiation from a cloud of a certain volume is dependent on the element abundances, gas evolutionary history, the local ionization, density and temperature of the gas. In very low-density gas, the nebula is optically thin to all H I resonance lines, and only radiative processes leading from recombinations need to be considered. So, a good approximation is the “case A” condition, where all line photons are assumed to escape the nebula without absorption. The other end of the extreme case is high-density gas, which has large optical depths in H I Lyman resonance lines. In this case, an approximation termed “case B”, assumes that Lyman line photons are absorbed immediately near the site of emission. When proton densities are large, collisional excitations dominate the radiative process taking place, and the emission coefficients are dependent on gas density. In both of these extreme cases, radiative transfer effects do not need to be considered. However, in intermediate densities, as may be the situation in a real nebula, the solution is somewhere in between the extreme cases of case A and case B. Resonance lines of abundance atoms have large optical depths through continuous absorption processes. Thus in this regime, we have to consider the effects of radiative transfer, scattering, and absorption. Lyman lines that don’t escape the nebula are absorbed by another H atom, leading to resonant scattering or resonant fluorescence excitation of another H I line.

1.3.2 From Atomic Data to Spectral Line Strengths

According to the principle of detailed balance, in thermodynamic and statistical equilibrium, each process is balanced by its inverse. Thus detailed balance equations can be used with atomic data, to determine the rate of excitations and/or deexcitation of each transition considered and the population of each level. This information can then be used to find the emission coefficient for each line, and, subsequently the line strengths.

1.4 CLOUDY

CLOUDY is an open-source spectral synthesis code that simulates a range of nebular conditions (Ferland et al., 1998, 2013, 2017; Chatzikos et al., 2023). It was originally designed for the UV, optical, and IR regime, but as its uses have broadened the code has been expanded to cover all of the electromagnetic spectrum. The code is an *ab initio* calculation of the gas properties and its spectrum, for one and two-electron atoms, all thermodynamic limits over an extremely wide range of gas and radiation density. The potency of CLOUDY as a research tool comes from its design to solve plasma, chemistry, radiation transport, and dynamics problems simultaneously and self-consistently, building from the foundation of individual atomic and molecular processes. It is suitable for application to a very wide range of astronomical prob-

lems from intergalactic, interstellar media to the gas surrounding AGN and those in supernova remnants.

Nature Astronomy published their second article on CLOUDY in their new column, “Access Code”, highlighting the importance of the code to the larger astronomical community. They note that “the US Decadal Survey on Astronomy and Astrophysics 2020 makes a point: “Despite the increasing importance of software development and developers for the advancement of the field, neither are sufficiently funded or supported by existing structures [...]. Funding for software maintenance and for open-source software projects, which have been transformative for astronomical science over the past decade, could pay major dividends in the future.” Woods (2023).

This work presents how light can be analyzed to gain information on nature. This was done by studying the structure, chemical composition, and physical processes occurring in hot gaseous nebulae, via improvements and additions to the CLOUDY code.

- In Chapter 2, I incorporate a new formalism into the CLOUDY to obtain a self-consistent set of dust depletions for the various elements according to the recently published model presented in Jenkins (2009). I examine whether there is any change to the spectral line ratio predictions from a photoionization model of the Orion H II region when the degree of dust depletions is altered.
- In Chapter 3, using the new dust depletion model as discussed in the preceding chapter, I show how strong-line spectra varies with the dust depletion strength, the ionization parameter and metallicity. These theoretical results are then compared with a sample of observed spectra from star-forming H II regions obtained from the Mapping Nearby Galaxies at Apache Point Observatory survey (MaNGA).
- In Chapter 4, I present the work to recast data from the latest version of CHIANTI atomic database to a common format used by CLOUDY and other codes. This chapter outlines the steps taken by the script for this version format change, and discusses the improvements to CLOUDY predictions as a result of using the new atomic database.
- In Chapter 5, presents the C23.01 update of CLOUDY. This update corrects a simple coding error, present since ~ 1990 , which primarily affected the intensity of what is often the strongest line in the spectrum, H Ly α .
- In Chapter 6, I resolve the fine-structure energy levels computed within CLOUDY in order to obtain predictions of X-ray spectra that matches the resolution of microcalorimeter observations. With the launch of *XRISM* this year, soon there will be a need for simulations that allow us to extract information from these high-resolution data.

Chapter 2 Self-consistent grain depletions and abundances I: The Orion Nebula as a test case

2.1 Introduction

Emission line spectra emergent from the ionized ISM are affected by the heavy-element abundances in the gas phase. Since the ISM absorbs and re-emits energy generated in stellar objects altering it from its original source (Spitzer, 1978), the emission and absorption spectra of the ISM contain information on its physical conditions. Since such information obtained from emission lines is widely used by large fields of study i.e. star formation and galaxy evolution, the accuracy of the photoionization model for the ionized ISM has far-reaching consequences. This in turn demands an accurate representation of the gas chemical composition present in H II regions in order to ensure that model predictions are consistent with spectroscopic observations.

With the launch of *Copernicus* in 1972, stellar observations of high-precision far-UV spectrometry allowed for studies on ultra-violet interstellar absorption features from heavy elements (Jenkins et al., 1973; Morton et al., 1973; Rogerson et al., 1973a,b; Spitzer et al., 1973a). Previously, element abundances in the ISM were assumed to be similar to that of cosmic abundances (also called solar abundances, because it is the chemical composition determined from absorption line measures of the Sun, stars, and meteorites normalized to 12.00 for hydrogen (Spitzer, 1978)), since it has been found that solar abundances are very similar to that in O and early-B stars (near which interstellar H II regions are located) (Salpeter, 1977). *Copernicus* observations revealed that heavy element abundances are lower in the ISM than in solar abundances. The difference between the observed element composition and the solar abundances was established as being due to the depletion of gas-phase atoms onto dust grains within the ISM. These studies on *Copernicus* observations also found that the degree of depletion varied from one element to the next and that the collective depletion strengths of many heavy elements varied significantly across different sightlines. Numerous studies also found a correlation between the average hydrogen density per sight line and the depletion strength (Savage and Bohlin, 1979; Harris et al., 1984; Jenkins et al., 1986; Jenkins, 1987; Crinklaw et al., 1994). Although, the spectra of H II regions do not contain the absorption features studied in the *Copernicus* observations, various other studies of emission-features have revealed the presence of dust, and the depletion of gas-phase elements onto dust-grains in these ionized regions as well Spitzer (1978).

2.2 Implementation details

CLOUDY is a modeling software that simulates a broad range of conditions in the interstellar matter and outputs predictions of observations, mainly spectral lines. It has long included depletion by grains. The current CLOUDY command that depletes

elements onto grains is based on works by Jenkins (1987) and Cowie and Songaila (1986). The keyword `metals deplete` without numbers on the command line, instructs the code to multiply the input abundances, by a set of scale factors specified in *Hazy 1*, Table 7.8. This depletion pattern has a few inadequacies: i. It does not deplete *S* and *Ar*. Although debatable, there is evidence that these elements could have a considerable amount of depletion (Jenkins, 2009; Savage and Mathis, 1979). Despite being a noble gas element, there is evidence that Ar “sticks” to the surface of grains, effectively depleting from the gas-phase (Amayo et al., 2021; Duley, 1985). ii. The grain abundance can only be altered by the `grains` or `metals` and `grains` command, which multiplies the grain abundances by the number specified in the command line. Therefore, grain composition may not be consistent with the depletion pattern of heavy elements. iii. The grain mass is not consistent with the mass of depleted heavy elements since the code does not conserve mass. iv. There is only one built-in depletion pattern in CLOUDY. While in reality, there could be a variety of depletion patterns (Spitzer, 1978; Osterbrock and Ferland, 2006).

The work published in Jenkins (2009, hereafter Jenkins09) allows for a universal depletion pattern that is appropriate for any line of sight in an H I region and can be adapted for most ISM column densities. Using a comprehensive survey of previously measured depletions, Jenkins09 built an abstract model of the depletion pattern in the ISM, where the depletion of each element is described by a function of three simple parameters (A_X , B_X , z_X). Their framework also describes the collective depletion strength of the various elements using a single parameter denoted by F_* , which we call depletion strength. This new model of element depletion solves some of the previous problems present in the CLOUDY code and provides a more up-to-date depletion pattern. Thus, the purpose of the present study is to update the CLOUDY code, by incorporating an option that uses the depletion pattern as described by Jenkins09.

Note that I am using the Jenkins09 model derived from the observations of the cold and warm neutral ISM, in order to study H II regions, because it is the only unified one available. It should be a high priority to build a depletion model for H II regions such as Jenkins09 work did for H I regions and this work is a first step in that direction.

This chapter is organized as follows. Section 2.2.1 describes the new calculations adopted from Jenkins09 that are being incorporated into CLOUDY. I test the new depletion calculations against a model of the Orion Nebula, and a discussion of the results that follow are presented in Section 2.3. Lastly, Section 2.4 describes the new commands and filenames that utilizes the calculations from Section 2.2.1. Although the new depletion framework solves many of the previous issues in the code, there are yet some caveats that need to be supplemented. For example, depletions of some important elements are missing in the new depletion pattern, there are a few elements with negative depletions which is not physical and it is not apparent how to scale grain abundances the new depletions. The fixes in the code for these shortcomings are also described in Section 2.4.

2.2.1 Calculating Post-Depletion Abundances

The standard definition for gas depletion is, ¹

$$[X_{gas}/H] \equiv \log\{N(X)/N(H)\} - \log(X/H)_{\odot}, \quad (2.1)$$

where $(X/H)_{\odot}$ are the reference abundances adopted from Lodders (2003) and $N(X)/N(H)$ is the gas-phase abundance after depletion (Jenkins, 2009). While CLOUDY provides more recent reference abundance determinations, this study uses reference abundances from Lodders (2003) in keeping consistent with the Jenkins depletion model. I rename the post-depleted gas-phase abundance to (X_{gas}/H) . Then solving for it I find,

$$(X_{gas}/H) = (X/H)_{\odot} 10^{[X_{gas}/H]}. \quad (2.2)$$

Jenkins09 presents a generalized depletion strength F_* that provides an empirical relationship between the individual log depletion scale factors $[X_{gas}/H]$ of different elements. This result is given in their equation 10,

$$[X_{gas}/H]_{F_*} = B_X + A_X(F_* - z_X). \quad (2.3)$$

where B_X , A_X , and z_X are parameters given in Jenkins09 Table 4; the depletion parameters for the special case of S are provided in Section 9 of his paper. Parameters B_X , A_X simply relate the value of $[X_{gas}/H]_{F_*}$ for a given element to that of other elements; so are unique to each element. As such, these depletion parameters are what determines the depletion pattern of the system. The parameter z_X was introduced to make the uncertainties of B_X , A_X independent from each other.

2.3 Impact on the star forming H II region: Orion Nebula

The Orion Nebula is one of the nearest, brightest, and most observed H II regions. The nebula's element abundances have been well studied (Rubin et al., 1991; Baldwin et al., 1991; Peimbert and Torres-Peimbert, 1977) along with the grains. It is a blister H II region, which is an ionized layer on the surface of the background OMC1 molecular cloud. The well-understood geometry and the extensive literature makes the Orion Nebula a suitable candidate to investigate the impact of dust depletion strength on predicted emission line spectra. Baldwin et al. (1991) developed a photoionization model of the Orion nebula which accounts for the emission from ionized gas as well as dust grains. The input file `orion_hii_open.in` specifying the physical parameters of this model can be found under the CLOUDY repository `tsuite/auto`. In Figure 2.1, the top panel shows the log of the depletion scale factor of elements S, O, N, and H as a function of depletion F_* , and the bottom panel depicts the line ratios predicted by the Orion Nebula model.

Even at a glance, it is apparent that the line ratios are affected to varying degrees by altering the depletion strength. We see that Sulfur is increasingly depleted with

¹Unlike standard notations in astronomy, note that $[X/H]$ denotes log depletion of an element X , and not log abundance ratio. Abundances are denoted with curved parenthesis (X/H) on a linear scale.

an increase in the value of F_* , much more than the other elements in Figure 2.1. This same trend is mirrored by the $[\text{S II}]/\text{H}\alpha$ ratio, seen in the bottom panel of the figure. In contrast, although F_* has no effect on the depletion strength of Nitrogen, and little effect on Oxygen compared to that of Sulfur, there is notable change to the line ratios $[\text{N II}]/\text{H}\alpha$, $[\text{O III}]/\text{H}\beta$, $[\text{O II}]/\text{H}\beta$, and $[\text{O I}]/\text{H}\alpha$. Albeit, this change is little compared to $[\text{S II}]/\text{H}\alpha$, we point out that element abundances of Nitrogen and Oxygen are depleted whilst the intensity of their line ratios are increasing. This is a result of when the overall abundances of coolants decrease in the gas, the electron temperature rises (see Figure 2.3 and discussion in Section 2.4.3), which strengthens the collisionally excited lines from elements that are not significantly depleted. In fact, we observe two competing effects that result in different trends of line ratios with F_* , depending on the slope of the depletion scale factor (A_X). On one hand, the depletion of heavy elements in the gas phase decreases the corresponding line strengths ratios. On the other hand, a rise in grain abundance, and a decline in coolant abundances increase the temperature, which in turn enhances the collisionally-excited line strengths. Hence, $[\text{S II}]/\text{H}\alpha$ exhibits a different trend to those of $[\text{N II}]/\text{H}\alpha$, $[\text{O III}]/\text{H}\beta$, $[\text{O II}]/\text{H}\beta$, and $[\text{O I}]/\text{H}\alpha$.

While it is interesting to observe such drastic results with $[\text{S II}]/\text{H}\alpha$, we should proceed with caution. The depletion of Sulfur suffers from contradicting results between various studies. Both Calura et al. (2009) and Jenkins09 provide contrary findings to the more common consideration that sulfur is an element of zero depletion. However, even the Jenkins09 study labels Sulfur as a troublesome element, due to the low number of sightlines where the S depletion could be reliably determined. Since, Sulfur is an important coolant in H II regions, its level of depletion affects other collisionally excited lines. So this depletion model will benefit from future, more extensive studies on the depletion of sulfur.

Our investigation shows that the ratios of a number of important optical emission lines are notably affected by the strength of dust depletion. Dust depletion alters the chemical composition of the gas, which is reflected by the line ratios of different elements. Meanwhile, how the line ratios change with the depletion strength depends on whether the corresponding elements are heavily depleted. Furthermore, this work should not be mis-interpreted to mean that H II regions have large distribution in F_* . In fact, a recent study on the abundances of various elements for nine different H II regions, showed a small variation in these abundances (Arellano-Córdova et al., 2021). Hence it may be that real H II regions have a small variation in F_* . So specifying F_* can become a critically useful tool to adjust the depletion pattern, since a more accurate representation of the depletions in any photoionized region can be obtained by manipulating a single parameter.

2.4 Modifications to CLOUDY

CLOUDY (Ferland et al., 2017) currently provides the option to include dust depletion by using the `metals deplete` command. We want to add an option to this command in which the user may vary the level of depletion of metals according to the depletion pattern described in Jenkins09, specified by the collective depletion

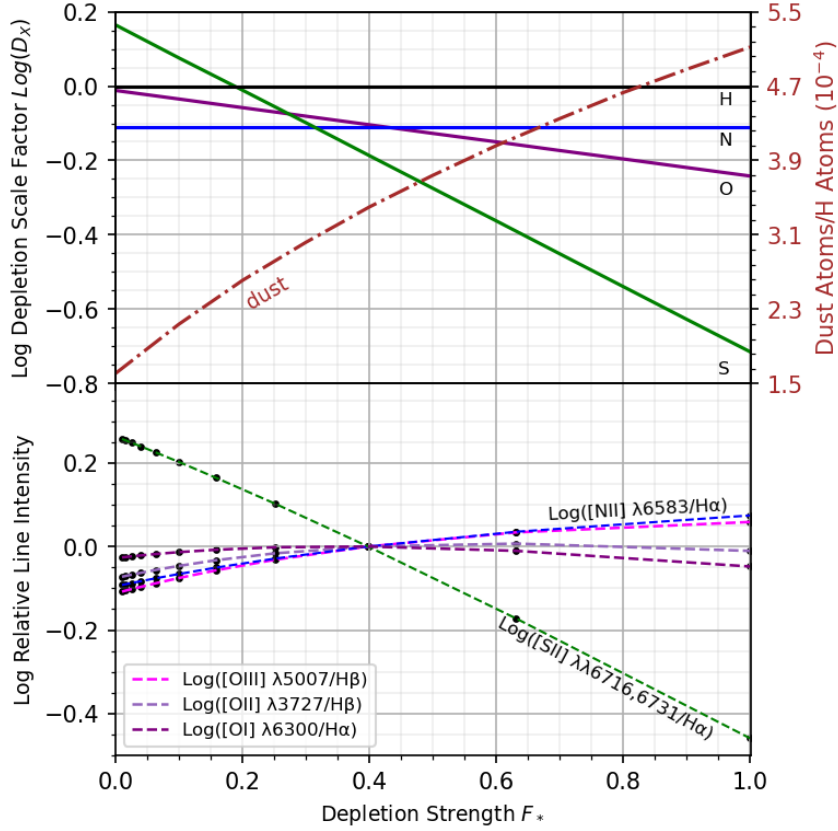


Figure 2.1: Interstellar element depletion scale factors $[X/H]_{F_*}$ (top panel) and predicted line strength ratios for the Orion nebula typically found in BPT plots subtracted by its own value at $F_* = 0.4$ (bottom panel) vs. depletion strength F_* . The red dashed line on the top panel represents the number of heavy element atoms locked in dust grains relative to the number of H atoms as a function of F_* . All data presented in this plot is obtained by output from CLOUDY. Note that the normalization of line ratios at $F_* = 0.4$ is to present the data in a way that is easily visually comparable. Furthermore, here grains are kept at their default Orion grain abundance.

strength F_* . This parameter is denoted by `Fstar` in the code, and it has observed limits $0 \leq F_* \leq 1$. Note that it is possible that a line of sight may have depletion strength outside this range, as these are not absolute limits. They represent the lowest (at $F_* = 0$) and highest (at $F_* = 1$) recorded depletion strengths for neutral gas with low uncertainties.

A version of the Jenkins09 Table 4, including S depletion parameters, is stored as a file called `Jenkins09_ISM_Tab4.dep` in the `data/abundances` directory. CLOUDY utilizes this input `.dep` file to compute the depletion scale factor D_X of an element X for a given F_* value using,

$$D_X = 10^{B_X + A_X(F_* - z_X)}. \quad (2.4)$$

This factor multiplies the reference abundance of X ,

$$(X_{gas}/H)_{F_*} = (X/H)_{\odot} D_X \quad (2.5)$$

to produce the post-depleted gas-phase abundance. The complete command syntax for this modification will be described in the next major release of CLOUDY. Note that this new command only depletes metals, while ISM grain abundances may be manipulated as before using the `grains` command.

Although the Jenkins09 investigation adopts their ISM reference abundances from Lodders (2003), the updated CLOUDY distribution will provide both the Lodders (2003) and Lodders and Palme (2009) versions of solar abundances already converted to a linear $H = 1$ scale. Users have the option of using one of the provided reference abundance files, or any other reference abundance file, by specifying it within the command, since the new depletion model is independent of the reference abundance set (because the depletion parameters in the Jenkins model were derived by analyzing differential changes in atomic gas abundances rather than studying the absolute depletions).

2.4.1 Missing Elements

The depletion parameters (A_X , B_X and z_X) of Li, B, Na, Al, Ar, K, Ca are important for a complete description of a photoionization model. However, Jenkins09 does not include the depletion of these elements in their depletion pattern. We supplement the depletion parameters of the above-mentioned heavy elements using data provided in Savage and Mathis (1979).

The $[X_{gas}/H]$ values for the elements listed above are provided by Savage and Mathis (1979) for two lines of sight, ζ Pup and ζ Oph. According to Jenkins09 Table 2, ζ Pup has an observed $F_* = 0.32$ and ζ Oph has an observed $F_* = 1.05$. Following that z_X is a parameter introduced simply to make the errors of A_X and B_X independent of each other, we set z_X to zero for the new elements. Since Equation 2.3 provides a linear relation between F_* and (X_{gas}/H) , we can backtrack our calculations from Section 2.2.1 in order to solve for the remaining two depletion parameters (A_X and B_X). We are then left with a simple system of equations to solve for.

$$A_X = ([X_{gas}/H]_{\zeta Oph} - [X_{gas}/H]_{\zeta Pup}) / (1.05 - 0.32), \quad (2.6)$$

$$B_X = [X_{gas}/H]_{\zeta Oph} - 1.05 A_X. \quad (2.7)$$

Note that Savage and Mathis (1979) do not provide the depletion value of Lithium for the ζ Oph sight line ($F_* = 1.05$), thus we require a different method for this element. Since lithium and silicon tend to have similar depletion values over many lines of sight (Savage and Mathis, 1979), we borrow the depletion parameter A_{Si} for that of Lithium. Then, using Equation 2.7 we have sufficient information to calculate B_{Li} . In addition to the above mentioned `.dep` file, we include another file with the calculated parameters of the supplemental elements called `Jenkins09_ISM_Gunasekera21.dep`.

Table 2.1: Calculated depletion parameters for missing elements from Jenkins09.

Elem.	$[X/H]_{F_*=0.32}$	$[X/H]_{F_*=1.05}$	A_X	B_X
(1)	(2)	(3)	(4)	(5)
Li	-1.439	-	-1.136	-0.245
B	-0.194	0.426	-0.849	0.698
Na	-0.884	-2.395	2.071	-3.059
Al	-3.318	-0.887	-3.330	0.179
Ar	-0.675	-0.298	-0.516	-0.133
K	-0.999	-0.902	-0.133	-0.859
Ca	-3.681	-2.351	-1.822	-1.768

NOTE – Data for columns (2) and (3) is taken from Savage and Mathis (1979), Fig. 3. Column (2) corresponds to ζ Pup, and column (3) corresponds to ζ Oph. Columns (4) and (5) are calculated using Eq. 2.6 and 2.7, respectively. For all the above-listed elements, z_X has been set to zero, since it is simply a parameter to separate the errors of A_X and B_X .

2.4.2 Limits of Depletions

CLOUDY users should make note that some $[X_{gas}/H]_{F_*}$ values for a few elements at low depletion strengths, are greater than 0. That is, at this particular depletion strength, these elements exhibit greater gas-phase abundance than their reference abundance (shown in the top panel of Figure 2.1, where the log depletion scale factor of Sulfur exceeds unity at $F_* < 0.2$). It is physically implausible to have more atoms of an element in the gas phase after depletions. In order to correct this error in our model, we have enabled CLOUDY users to provide a maximum cut off for $[X_{gas}/H]_{F_*}$, using the keyword LIMIT.

2.4.3 Scaling Grains

When the ISM gas is depleted by a higher degree, the number of atoms in the dust phase increases. This may result in a greater number of grains with the same grain properties, or larger-sized grains (Spitzer, 1978). Photoelectric heating by extra dust grains would then raise the equilibrium temperature, which in turn affects the strength of the collisionally excited lines. Therefore, in order to get accurate spectral line predictions for a given model, it is necessary to scale grain abundance in CLOUDY along with F_* .

Using the standard Orion grain abundance as the base value, we scaled the grain abundance for a set of F_* values according to following fraction,

$$fraction = \frac{\sum_X (X_{dust}/H)_{F_*}}{\sum_X (X_{dust}/H)_{0.5}}. \quad (2.8)$$

Here we assume that $F_* = 0.5$ represents the default set used by CLOUDY because Hensley and Draine (2021) adopts $F_* \approx 0.5$ for general star forming galaxies, and because both sets have similar depletions. Such an analysis yields Figure 2.2, where

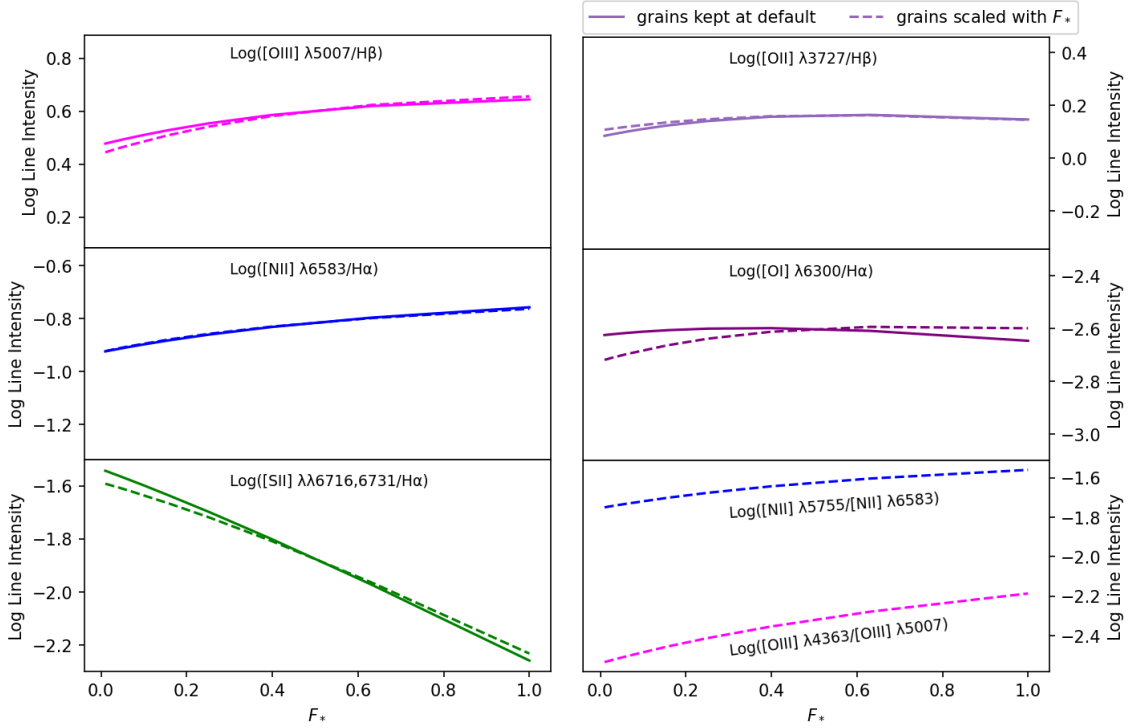


Figure 2.2: Predicted line strength ratios for the Orion nebula typically found in BPT plots vs. depletion strength F_* . All data presented in this plot is obtained by output from CLOUDY. This is the same data that appears in the bottom panel of Figure 2.1, except without normalizing to intensities at $F_* = 0.4$.

the solid lines represent the model results with grain abundance kept at its default CLOUDY value and the dashed-style lines represent results when grains are scaled as described above (see Section 2.3 for a more detailed discussion on the Orion nebula model in CLOUDY). In Figure 2.2, most line ratios exhibit little difference in intensities between the dashed and solid lines. In addition, most line ratios are slightly diminished when grains are scaled down at low F_* , and slightly enhanced when grains are scaled up at high F_* . Line ratios $[\text{N II}]/\text{H}\alpha$ and $[\text{O II}]/\text{H}\beta$ are exceptions to this. A possible explanation is that dust results in photo-electric heating of the gas, which in turn enhances forbidden lines. So when the dust is scaled down, less heating by dust causes less enhancement of line-ratios, and vice versa when the dust is scaled up for high F_* . The intensity of $[\text{N II}]$ is not changed by scaling grains since the strength of nitrogen depletion is constant at all F_* . Among line ratios checked, $[\text{O I}]/\text{H}\alpha$ exhibits the most change as we alter grain abundance. A discussion in the next paragraph involving temperature profiles helps explain some of this behavior. This change to the intensities of line ratios when grains are scaled compared to when they are not scaled is very minimal to none. This suggests that, under the assumption that grain abundance is directly proportional to the number of atoms in dust grains, scaling grains with F_* does not have a significant impact on the line intensities.

Scaling grains should affect the temperature profile on an H II region, as grains

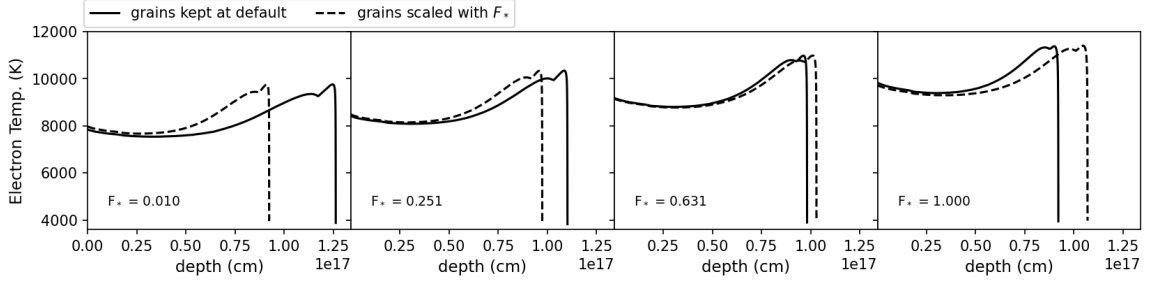


Figure 2.3: Temperature profile of the H^+ layer across the H II region. Panels from left to right indicate temperature profile with increasing depletion strength F_* . The dashed line corresponds to the models where grains were scaled as in Figure 2.2, and the solid line corresponds to grain abundance kept at CLOUDY’s default Orion grain abundance.

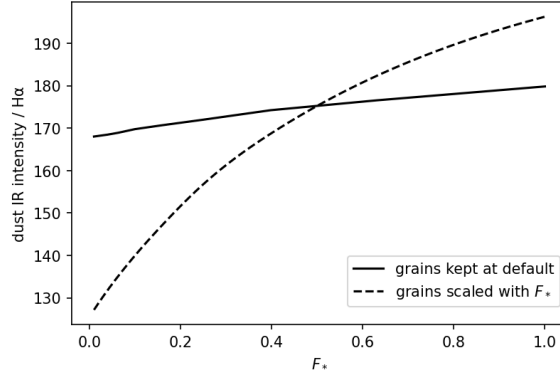


Figure 2.4: IR emissions by dust in the H^+ layer across the H II region, as grain abundance is scaled with F_* (solid line) and kept at default Orion grain abundance (dashed line), both relative to the $H\alpha$ line.

contribute to heating the ISM via photoelectric emissions, and change the location of the ionization front by reducing the number of ionizing photons. Dust absorbs far UV radiation from starlight, then re-radiates it as IR radiation. This results in the dust heating up, as well as the photo-ejected electrons heating up the gas (Spitzer, 1978). So, if an increase in F_* is expected to increase grain abundance, then we expect depletion strength to have a positive correlation with the overall temperature of the system.

The plots in Figure 2.3 and the bottom-most right panel in Figure 2.2 show that F_* has two effects on the temperature profile. The dashed lines in both figures correspond to the model results when grains were scaled as in Figure 2.2, and the solid line corresponds to when grains were left at their default Orion abundance. First, we observe that Figure 2.3 and the line ratios $[O\text{ II}]\lambda 4363/[O\text{ II}]\lambda 5007$ and $[N\text{ II}]\lambda 5755/[N\text{ II}]\lambda 6583$ (which are electron temperature tracers) agree with our expectation that increasing F_* will increase the overall temperature, for both scaled and non-scaled grain cases. Increasing depletion strength increases grain abundance while depleting coolants, thereby increasing the overall temperature of the H II region.

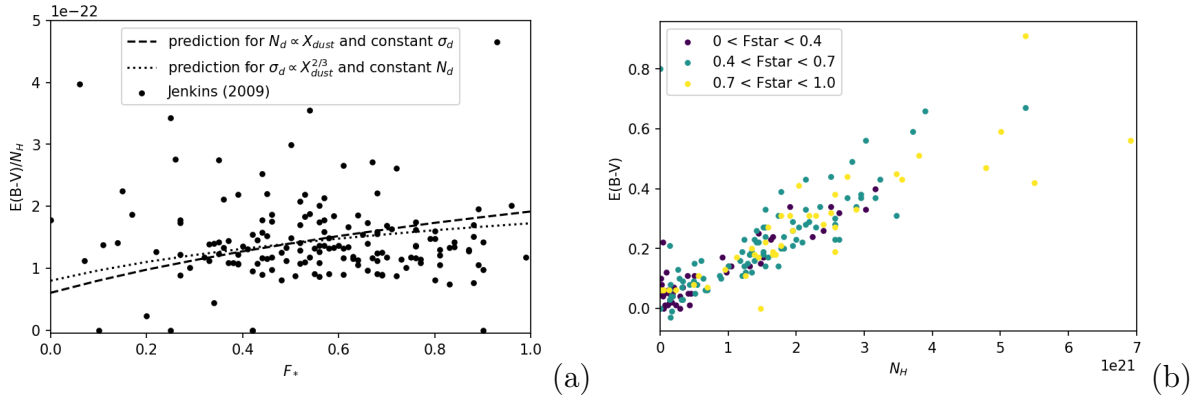


Figure 2.5: (a) Depletion strength F_* vs. color excess $E(B - V)$ per hydrogen column density N_H . (b) Color excess $E(B - V)$ vs. hydrogen column density N_H . Both plots show the same data. The data are obtained from the lines of sight listed in Jenkins09.

Second, scaling grains using our method has a significant effect on the location of the H ionization front. Figure 2.3 depicts that the H ionization front appears at greater depths for $F_* < 0.5$ when grains are scaled, compared to when they are not. In addition, increasing F_* for scaled grains decreases the depth of the H front. The opposite effect occurs when grains are not scaled with F_* , resulting in the H ionization front for scaled grains appearing at a shallower depth at $F_* > 0.5$, than that for non-scaled grains.

Notice in Figure 2.4 when grains are scaled, the IR emission from dust increase significantly with F_* relative to the emission when grains are not scaled. This demonstrates that as the dust abundance increases, it absorbs more ionizing photons, reducing the depth of the H^+ layer discussed in Figure 2.3. The ionization structure of the cloud is thus significantly affected once the grains are scaled. It is expected that the size of the hydrogen partially ionized zone (a.k.a H^+ layer across the H II region) inside the clouds may be sensitive to the changing number of ionizing photons. Since the line ratio $[O I]/H\alpha$ is more sensitive to the size of the partially ionized zone than the other line ratios, this may explain why the intensity of $[O I]/H\alpha$ is most affected by scaling grains as shown in Figure 2.2.

The absolute extinction of spectral lines emerging from a cloud is proportional to the product of the grain column density and the geometrical cross-section of a single grain (see equation (7-1) of Spitzer (1978)). Hence the grain abundance may be alternatively found indirectly via observing the variation of the extinction of the gas with depletion strength F_* . Figure 2.5 shows two plots comparing extinction to F_* for the set of sightlines listed in Jenkins09. The dashed line in Figure 2.5(a) represents the expected trend, if only the number of grains (N_d) changed with F_* with the size of individual grains kept constant. The dotted line represents the expected trend if only the geometrical cross-section of grains (σ_d) changed with F_* with a constant number of grains. Let $\sum_X (X_{dust}/H)_{F_*}$ denote the total number of atoms in dust phase at a specified F_* with X_{dust, F_*} . Given the Spitzer (1978) result $A_V \propto N_d \cdot \sigma_d$ and that

$N_d \propto X_{dust,F_*}$, $\sigma_d \propto (X_{dust,F_*})^{2/3}$, we expect the relations

$$E(B - V) = \bar{E}(B - V) \cdot \frac{X_{dust,F_*}}{X_{dust,0.5}}, \quad (2.9)$$

and

$$E(B - V) = \bar{E}(B - V) \cdot \left(\frac{X_{dust,F_*}}{X_{dust,0.5}} \right)^{2/3}, \quad (2.10)$$

respectively, where $\bar{E}(B - V)$ is the average color excess at $F_* = 0.5$. Here we have assumed that R_V does not change with F_* . Figure 2.5(b) shows the correlation between $E(B - V)$ and N_H for three different bins of F_* values. Both analyses show only random scatter, with no discernible correlation between F_* and $E(B - V)$. Although the expected lines have a small slope, the line of sight seems to concentrate around the average color excess for all values of F_* . In addition, there are many sightlines with low F_* but high $E(B - V)$ and many with high F_* but low $E(B - V)$. Figure 2.5(b) further establishes that there is no observable trend, as all three bins of F_* values seem to populate the higher and lower ratios of $E(B - V)$ to N_H . Hence at this moment, no clear relation between extinction and depletion strength can be established.

We conclude it is better not to include scaling grains with F_* in the current depletion model, since: 1. Scaling grain abundance using total atoms in the dust phase shows a minimal change in spectral line ratios. 2. We could not discern a relationship between depletion strength and extinction based on the current data to constrain the scaling relation for dust grains. Consequently, the new CLOUDY command depletes gas abundances only. Grain abundances can be manipulated at the user's discretion, as before using the `grains` command, independent of the new gas-depletion command.

2.5 Conclusions

The primary purpose of this study was to streamline the calculations of dust depletion as described by Jenkins09, making manipulation of depletion strength in a model much simpler. Although there have been various advances on the study of depletions of gas abundance onto dust grains, such depletions are seldom included in investigations as it has not been incorporated into any modeling software thus far to the best of our knowledge. The main outcomes of this investigation are as follows.

1. We have integrated into CLOUDY, the calculations of depleted abundances of 22 elements via the depletion scale factor D_X (see Eq. 2.4). The depletion pattern of 7 out of the 22 elements was determined using the published post-depleted abundances obtained from Savage and Mathis (1979). Whereas the depletion parameters (A_X , B_X , z_X) of the remaining 15 elements were provided in the published work of Jenkins09. As a result of some caveats in Jenkins' work, we have included a command to limit the maximum depletion of elements to remain within physically viable standards.

2. The predicted spectrum changes significantly with F_* . As depletion strength is altered, we have observed a significant change in $[\text{S II}]/\text{H}\alpha$, and comparatively little change in $[\text{N II}]/\text{H}\alpha$, $[\text{O III}]/\text{H}\beta$, $[\text{O II}]/\text{H}\beta$ as a result of two competing effects. One is the decrease of heavy elements in the gas phase which would decrease the line ratio intensity of an element. The other is the increase in temperature which would increase the collisionally-excited line strength. Depending on the value of A_X , the competing effects result in different trends of line-ratio versus F_* . This provides an explanation for $[\text{S II}]/\text{H}\alpha$ showing a different trend from $[\text{N II}]/\text{H}\alpha$, $[\text{O III}]/\text{H}\beta$, $[\text{O II}]/\text{H}\beta$, and $[\text{O I}]/\text{H}\alpha$.
3. Sulfur is a strong coolant, thus changing its depletion strength changes the intensity of other line ratios. Our results show that $[\text{S II}]/\text{H}\alpha$ is more sensitive to changes in F_* than the other line ratios, making S very important. However, Jenkins09 notes that determining the depletion pattern of this element is challenging and its depletion factors are more uncertain than for other elements. Furthermore, H II abundances are derived from emission lines, whereas solar abundances are from absorption lines, in which the biggest difference is the depletion of Sulfur. As such, to determine which of its results are truly compelling, the depletion of S merits further investigation.
4. F_* is negatively correlated with the depth at which the H ionization front occurs and is positively correlated to the overall temperature of ISM gas. Increasing F_* increases heating by dust, as well as reduces coolant abundances, thereby heating up the ISM. In addition, our analysis on scaling dust abundance with F_* reveals that only the depth at which the H ionization front occurs is altered, and not the overall temperature of the ISM. When grain abundance is scaled, the intensity of IR emissions from dust is positively correlated with F_* . Hence, lower grain abundance at low F_* results in less dust available to absorb ionizing photons resulting in a deeper H ionization front when grains are scaled with F_* . This also indicates the thickness of the hydrogen partially ionized region decreases with F_* . Further investigation on the correlation between dust IR emissions and a F_* for a statistical sample of H II regions, will be beneficial to establish this result.
5. Details of dust depletions are not yet well understood, and the new CLOUDY commands will provide a better way to study the subject. As atoms of elements removed from the gas phase can only go into dust phase, dust abundance must increase when elements are depleted to greater degrees. Our attempt at scaling dust depletion showed little change to line ratio intensities. Compared to the other line ratios, $[\text{O I}]/\text{H}\alpha$ was the most affected by scaling grains, which upon investigation was likely a result of a change in the hydrogen partially ionized zone size with change in grain abundance. In addition, as the dust has a hand in the extinction process of light from distant objects, it stands to reason that F_* must have some relation with $E(B - V)$. However, our analysis of color excess, gathered from the literature, has yielded no such relation. Therefore, at this moment, it is premature to include the scaling of grain abundance alongside

that of the gas-phase abundance. Further study is required to determine at which scale depletion strength F_* affects dust abundance.

The results contained in this study can be generalized to other H II regions since this method of defining dust depletion using F_* is appropriate for any line of sight. Consequently, as altering depletion strength has an impact on the predictions for even the most widely studied H II region - the Orion Nebula, so would it on other H II regions. Moreover, since F_* allows us to adjust the depletion pattern self-consistently using a single parameter, and since F_* affects predicted emission line spectra, which in turn impacts studies on star formation and galaxy evolution, we conclude that it is critical to specify F_* when utilizing the model of any H II region, regardless of the distribution of F_* in H II regions.

This investigation begins to realize the impact of depletion strength F_* on strong line spectra of H II regions. However, our depletion model yet has many gaps to be filled. Although we have shown that specifying F_* affects emission line spectra in the Orion Nebula model and speculated that it should generalize to other H II regions based on Jenkins09 work, we have not shown empirical evidence of this generalization. Furthermore, we also do not know the distribution of F_* for H II regions. The study of a statistical sample of H II regions may be of use to establish the general effect of F_* on the line ratios from these regions. Our main results for trends with F_* stems from two competing effects on the abundance of gas available to ionize, and on the abundance of coolants. A more in-depth investigation on the effects of F_* on the temperature profile, and an investigation of ionization parameter with F_* may be necessary to better solidify this result. Such investigations will be presented in a future publication.

Chapter 3 Self consistent grain depletions and abundances II: Effects on strong-line diagnostics of extragalactic H II regions

3.1 Introduction

The condensation of various elements into solid form, or grain depletion, is an important physical process in the interstellar medium (ISM). Observations have long found that the elemental abundance in the ISM is lower than the values in stars (Jenkins et al., 1973; Morton et al., 1973; Rogerson et al., 1973a,c; Spitzer et al., 1973b; Spitzer, 1978). Despite the large number of observations, the physics of grain depletion is still not well understood. Observations of the absorption of the UV spectra of stars in the ISM of the Milky Way Galaxy have revealed that the degree of depletion varies between different heavy elements and at different locations of the ISM Morton et al. (1973); Rogerson et al. (1973a,c); Jenkins et al. (1973). As a result, it is challenging to draw a consistent picture describing the depletion of all elements in the ISM. To solve the above problem, Jenkins09 studied the abundances along 243 different sight-lines from more than 100 papers and proposed a unified scheme of parameterizing the depletion factors for a set of 17 different elements. The fact that the depletion factors of various elements are positively correlated makes it possible to describe them using a single parameter, which is denoted as F_* by Jenkins09. The depletion factor (F_*) describes the overall dust depletion strength of a collection of elements, for a given line of sight. With the unification of the depletion patterns, it is now possible to estimate the typical level of depletion by using observations of a few lines.

Despite the important breakthrough by Jenkins09, this unified scheme for grain depletion has seldom been applied and studied in depth in works of theoretical photoionization modeling of the ionized ISM. This study is published as the second of a series ‘Self-consistent grain depletions and abundances’. The first paper Gunasekera et al. (2022) (presented in Chapter 2) implements the Jenkins09 depletion model in CLOUDY (a modeling software that can output spectral line predictions by simulating a broad range of conditions within the ISM Ferland et al. (2017)), to obtain photoionization model predictions of varying F_* on the Orion Nebula as a test case. This work shows that values of depletion factors have a nontrivial effect on the model predictions for the Orion Nebula. On the one hand, grain depletion affects the remaining gas abundance of the depleted elements directly. On the other hand, it also impacts the thermal balance of the whole ionized cloud by changing the relative abundance of the coolants. Inaccurate prescriptions of grain depletion would thus lead to unrealistic predictions on the emission-line spectra. As a consequence, the calibrations of various physical parameters in the ISM, including the gas-phase metallicity, would suffer from large uncertainties. Therefore, it is important to understand the effect of grain depletion on the theoretically predicted emission line spectra and the relevant emission line diagnostics.

To better understand the effect of grain depletion on emission-line spectra and establish the results in Chapter 2, the first part of this study extends the analysis used

on the Orion Nebula to a more generalized photoionization model. Such an investigation utilizing a large range of F_* values in conjunction with a range of ionization parameters and metallicities was made possible by the integration of the Jenkins09 model into CLOUDY (see Chapter 2 for further description of this new function). The second part of this study compares these model predictions to observations of a sample of H II regions obtained from the Mapping Nearby Galaxies at Apache Point Observatory survey (MaNGA)(Bundy et al., 2015; Yan et al., 2016). The goal was to constrain the grain depletion factor for the general population of H II regions indirectly. Interestingly, even the best-fit depletion factor we found does not provide a perfect match to the data in a multidimensional line-ratio space. This is likely due to the N/O prescription we use to construct the models does not fit the data locus perfectly after we apply the depletion.

This chapter is organized as follows. In Section 3.2, we describe the photoionization models we use and how we set-up the input parameters, especially the depletion factor. In Section 3.3, we present our results and show how the different line ratios depend on the depletion factor as well as its physical interpretation. In Section 3.4, we discuss the effect of grain depletion on optical diagnostics of ionized regions and use observed emission-line spectra to constrain the depletion factor in extra-galactic H II regions. We conclude in Section 3.6. For the frequently used logarithms of line ratios throughout this chapter, $\log([\text{O III}] \lambda 5007/\text{H}\beta)$, $\log([\text{N II}] \lambda 6583/\text{H}\alpha)$, $\log([\text{S II}] \lambda\lambda 6716,6731/\text{H}\alpha)$, and $\log([\text{O I}] \lambda 6300/\text{H}\alpha)$, we denote them as R3, N2, S2, and O1, respectively.

3.2 Photoionization models

The approach of this study is to use CLOUDY to run model grids simulating H II regions by varying the metallicity (hereafter $(\text{O}/\text{H})/(\text{O}/\text{H})_{\odot}$, which is equivalent to $(\text{O}/\text{H})_{gas}/(\text{O}/\text{H})_{ref}$), ionization parameter, and the collective elemental depletion (represented by the depletion factor F_*) and predict the corresponding emission line spectra. This is the same procedure as described in Chapter 2, but we generalized it for different ionization parameters and metallicities.

3.2.1 The Jenkins09 depletion model

In the ISM, depletion of an element into dust grains is defined as the reduction of abundance below the expected abundance level. These expected abundances will be referred to as reference abundances henceforth, and denoted as $(X/H)_{ref}$.

$$[X_{gas}/H]_{F_*} = \log(X_{gas}/H)_{F_*} - \log(X/H)_{ref}. \quad (3.1)$$

The study by Jenkins09 presents a linear relationship between the individual depletion of each element. They were able to find such a relation by introducing a generalized depletion strength F_* . This depletion strength describes the depletion of each element $[X_{gas}/H]_{F_*}$ as a linear relation to itself (F_*), and it is common to all elements

$$[X_{gas}/H]_{F_*} = B_X + A_X(F_* - z_X), \quad (3.2)$$

Table 3.1: Reference abundance sets $(X_{gas}/H)_{\odot}^{(2003)}$ (Lodders, 2003), $(X_{gas}/H)_{\odot}^{(2009)}$ (Lodders and Palme, 2009), and GASS-Grevesse et al. (2010) are all available to be used with the CLOUDY grain depletion command. The models for this study have used the GASS abundances as the reference set.

Elem.	$(X_{gas}/H)_{\odot}^{(2003)}$	$(X_{gas}/H)_{\odot}^{(2009)}$	GASS
H	1.00E+00	1.00E+00	1.00E-00
He	9.64E-02	8.43E-02	8.51E-02
Li	2.24E-09	1.90E-09	1.12E-11
Be	3.02E-11	2.09E-11	2.40E-11
B	7.08E-10	6.42E-10	5.01E-10
C	2.88E-04	2.45E-04	2.69E-04
N	7.94E-05	7.24E-05	6.76E-05
O	5.75E-04	5.36E-04	4.90E-04
F	3.39E-08	2.74E-08	3.63E-08
Ne	8.91E-05	1.12E-04	8.51E-05
Na	2.34E-06	1.97E-06	1.74E-06
Mg	4.17E-05	3.52E-05	3.98E-05
Al	3.47E-06	2.89E-06	2.82E-06
Si	4.07E-05	3.41E-05	3.24E-05
P	3.47E-07	2.83E-07	2.57E-07
S	1.82E-05	1.44E-05	1.32E-05
Cl	2.14E-07	1.76E-07	3.16E-07
Ar	4.17E-06	3.16E-06	2.51E-06
K	1.51E-07	1.28E-07	1.07E-07
Ca	2.57E-06	2.06E-06	2.19E-06
Sc	1.41E-09	1.17E-09	1.41E-09
Ti	1.00E-07	8.43E-08	8.91E-08
V	1.17E-08	9.76E-09	8.51E-09
Cr	5.25E-07	4.47E-07	4.37E-07
Mn	3.80E-07	3.15E-07	2.69E-07
Fe	3.47E-05	2.89E-05	3.16E-05
Co	9.55E-08	8.02E-08	9.77E-08
Ni	1.95E-06	1.67E-06	1.66E-06
Cu	2.19E-08	1.85E-08	1.55E-08
Zn	5.01E-08	4.44E-08	3.63E-08

where A_X, B_X and z_X (referred to as depletion parameters hereafter) are best-fit parameters found in table 4 of Jenkins09 for this linear relation. These depletion parameters are independent of the reference abundance because they were developed using differential changes in gas abundances as opposed to absolute depletions. Hence this study will use the Grevesse et al. (2010) reference abundances with Jenkins’ depletion model, although his model was built using reference abundances obtained from Lodders (2003).

3.2.2 Input parameters for photoionization models

The photoionization models in this study is generated using the development version of CLOUDY (Ferland et al., 2017, C17) (last described by <https://nublado.org/>). In addition to the overall chemical abundance and the dust prescription mentioned in the previous subsection, there are many other input parameters that impact the resulting emission line spectra. Here we summarize the values of the photoionization model parameters adopted in this work.

First, the ionization parameter (U) describes the relative strength of ionizing radiation in the H II region. U is defined as $U \equiv \frac{\Phi_{ion}}{n_H c}$, where Φ_{ion} is the flux of the hydrogen ionizing photons at the illuminated face of the cloud, n_H is the hydrogen density and c is the speed of light. This study varies the ionization parameter in the logarithmic space so that $-4.0 < \log(U) < -2.0$ with increments of 0.5. The shape of the radiation field is described using the stellar SEDs generated by the code STARBURST99 (Leitherer et al., 1999, 2014, v7.01). We adopt a Kroupa IMF (Kroupa, 2001), a continuous star formation history of 4 Myr, the Geneva evolutionary track with standard mass-loss rates, and the Pauldrach/Hiller model atmosphere (Pauldrach et al., 2001; Hillier and Miller, 1998). A total of six SEDs with stellar metallicities from $\log(Z/Z_\odot) = -1.3$ to $\log(Z/Z_\odot) = 0.5$ are considered. Since STARBURST99 only provides models with stellar metallicity up to $\log(Z/Z_\odot) \approx 0.3$, we compute the SED model with the highest stellar metallicity through linearly extrapolating the logarithmic fluxes. When these SEDs are used in our photoionization models, the gas-phase metallicity, $[O_{gas}/H]$, is ensured to match the stellar metallicity.

For the structure of the ionized cloud, a plane-parallel geometry was chosen and calculations are stopped when the temperature falls below 100 K. The equation of state is set to be isobaric and the initial hydrogen density is 14 cm^{-3} , which is the median density found in the SF regions of MaNGA (Ji et al., 2020). A detailed description of the MaNGA survey is delayed to Section 3.4.

To fix the collective depletion of the elements, we use the unified depletion model provided by Jenkins09 described in Section 3.2.1. Chapter 2 has introduced a command that implements this Jenkins09 model into CLOUDY, which streamlines the calculation of depleted gas-phase elemental abundances and allows for a grid of varying F_* values to be simulated. Since the equations and parameters used to calculate the input abundances are from the Jenkins09 study, the complete range of depletion factors used in this study is from $F_* = 0$ to 1.0. The present study breaks this F_* range into increments of 0.125. It should be noted that these upper and lower limits of F_* are not real physical limits; they are the highest and lowest observed depletions

from the observations compiled by Jenkins09. As such, $F_* = 0$ should be interpreted as the system having some small amount of depletion above no depletion.

The abundance of dust grains is scaled with F_* as described in Chapter 2. The default set of grain abundance used by CLOUDY is assumed to correspond to a depletion strength of $F_* = 0.5$, as before. The subsequent grain abundances for varying F_* are scaled with the fraction of total (X_{grains}/H) at a given F_* to the total (X_{grains}/H) at $F_* = 0.5$, as calculated using the Jenkins09 depletion function. Since any element that depletes from the gas phase should appear in the dust phase, we define grain abundance as,

$$(X_{grains}/H) \equiv 1 - (X_{gas}/H). \quad (3.3)$$

The metallicity $((O/H)/(O/H)_\odot)$ of the model input into CLOUDY was altered using the ‘metallicity scale factor’ command. CLOUDY multiplies the abundances given in the abundance file, by the value provided in this command line. Note that using $(O/H)/(O/H)_\odot = 1.00$ means that the model has gas abundances equivalent to the reference abundances. Although the Jenkins09 model was built using Lodders (2003) and a newer set of abundances are available from the same authors – Lodders and Palme (2009), we use the reference abundance set of GASS. All three reference abundance sets are summarized in Table 3.1. $(O/H)/(O/H)_\odot$ used in this study are 0.05 which represents a metal-poor system, 1.00 which keeps the reference abundance set unchanged, and 3.16 which represents a metal high set. The value of the factor for the highest metallicity model, 3.16, is derived from extrapolating the SED of starburst99 in order to cover the whole data space used in Section 3.4. Models with metallicity scale factors 0.20, 0.40 and 2.00 were also studied, but are only shown and discussed in Section 3.4 for the sake of brevity.

Finally, the abundances of some specific elements require additional treatments. For helium, we consider the cosmic plus nuclear synthesis production of these elements using the formula of Dopita et al. (2002)

$$He/H = 0.0737 + 0.024(Z/Z_\odot). \quad (3.4)$$

For secondary elements including carbon and nitrogen, we use the prescription of Dopita et al. (2013) while refitting their relation using a second-order polynomial function

$$N/O = 0.0096 + 72 \cdot O/H + 1.46 \times 10^4 \cdot (O/H)^2, \quad (3.5)$$

which gives the N/O ratio at each metallicity. In addition, we fixed C/N to be the reference abundance value, as did Dopita et al. (2013). We note that this relation only describes the nitrogen-to-oxygen ratio before depletion.

A summary of all the model parameters can be found in Table. 3.2.

3.3 Impact on a generalized H II region

The collisionally-excited lines we study in this work are produced by collisions between heavy element atoms and free electrons that result in the excitation of an atomic electron, followed by its radiative deexcitation. Various factors can alter the rate of

Table 3.2: Photoionization model parameters

Parameter	Input value
F_*	0, 0.125, 0.25, 0.375, 0.5, 0.625, 0.75, 0.875, 1
Z/Z_\odot	0.05, (0.20, 0.40), 1.00, (2.00), 3.16
$\log(U)$	-4.0, -3.5, -3.0, -2.5, -2.0
SED	Continuous star formation over 4 Myr (generated by STARBURST99)
Secondary element prescriptions	Same as the ones adopted by Dopita et al. (2013)
Background radiation	Cosmic ray background at $z = 0$
Geometry	Plane-parallel
Initial hydrogen density	14 cm^{-3}
Equation of state	Constant gas pressure

these collisions, such as increasing temperature which increases the rate of collisions, and changing the abundance of atoms per H available for collisions. Since variations in the depletion strength, F_* , within a gas cloud alters the abundance pattern, we expect that F_* affects both of the above-mentioned factors. An analysis of how the gas temperature and the emission line spectra behave with variations in F_* in conjunction with variations in ionization parameter and metallicity should provide insight into how these parameters may be constrained in photoionization models.

The calculation of post-depletion abundance of each element has been streamlined by incorporating the Jenkins09 depletion model and their depletion parameters into the widely used program CLOUDY as described by Chapter 2. That paper provides a preliminary study into how the depletion factor F_* affects the spectra of a benchmark H II region – the Orion Nebula. In the present study, we shall extend this work to a more generalized H II region. In doing so, we have run the photoionization model described in Section 3.2.2 with three variable dimensions – F_* , U , and metallicities. The resulting spectral line intensities of R3, N2, S2, and O1, as well as the electron temperature profiles obtained are discussed in the following sections.

3.3.1 Effect of depletion strength on temperature

The equilibrium temperature of an interstellar cloud in (or close to) thermal balance should remain relatively constant over time, i.e. the cooling mechanisms should balance the heating mechanisms of the gas. In H II regions photoionization of H atoms dominate in heating the gas, while inelastic collisions between electrons and ions dominate in cooling the gas. Sulfur, oxygen and nitrogen are important coolants in the H II region. Therefore, we expect temperature changes to be dominated by changes in the gas-phase abundances, particularly of S and O. In Chapter 2, we showed that changing F_* had two effects on the temperature profile of the Orion model. Higher depletion strengths both increase the overall temperature of the Orion model and cause the H ionization front to occur at shallower depths. Since the depletion strength affects the abundance of gas-phase elements, which includes the abundance

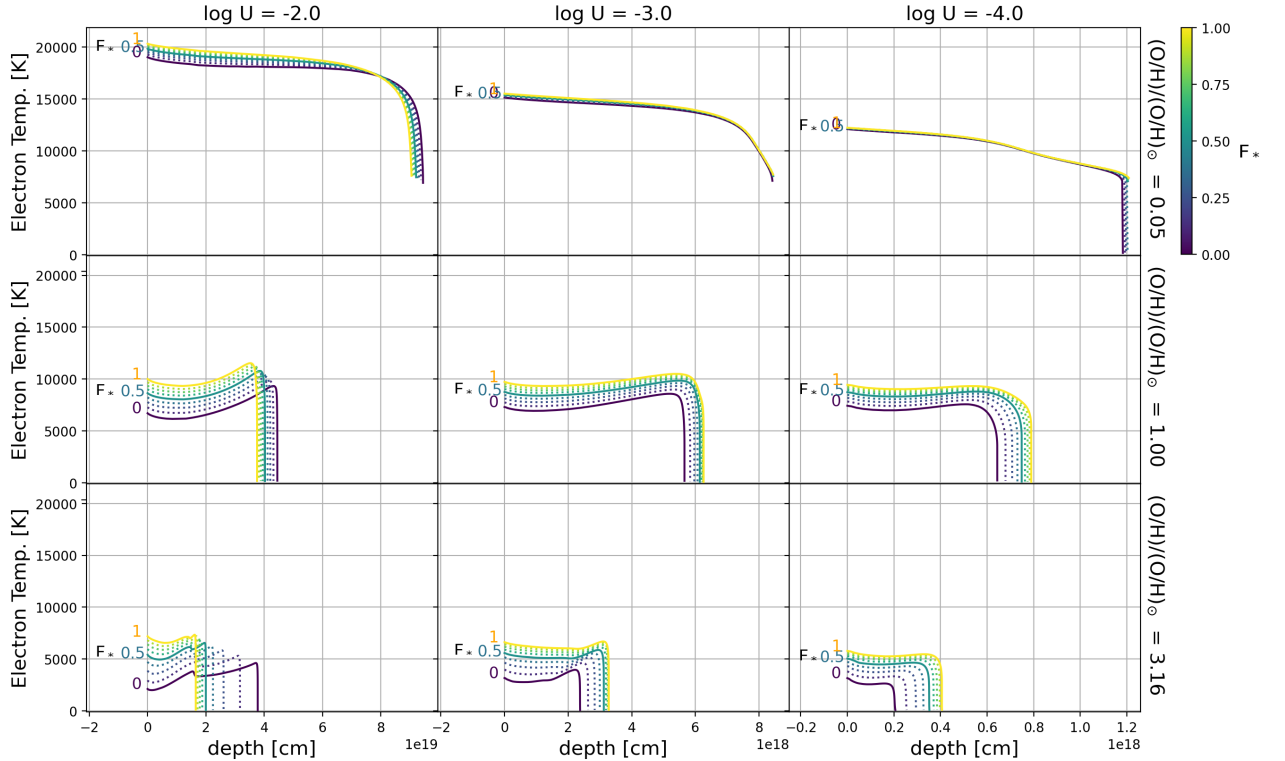


Figure 3.1: Temperature profile of the cloud at varying metallicity values (listed on the right edge of the figure), ionization parameters (listed on the top edge of the figure), and depletion strength. Each line jumps by 0.125 change in F_* . The depth is taken from the illuminated face at 0 cm, increasing out to the H ionization front. The ionization front is seen where the temperature profile drops off. In the bottom-left most panel, the second bump in the profile indicates the He ionization front. Despite the x-axis scale, this figure can be related to the Strömgren length via the ionization parameter, see Equation (3.6).

of the above-mentioned coolants, we expect a similar trend for the temperature profile in this model to that shown in Chapter 2.

Fig 3.1 presents the electron temperatures, T_e , as a function of depth of H II regions with varying U , $(\text{O}/\text{H})/(\text{O}/\text{H})_\odot$, and F_* . The electron temperature T_e , which is the kinetic temperature of charged particles, provides a measure of the H II region temperature. We vary two parameters in this study which were kept constant in Chapter 2 – metallicity and ionization parameter, to understand how other parameters may affect the H II region in conjunction with F_* . A further discussion of why we expect temperature changes to be dominated by changes in the gas-phase abundances, particularly of S and O, is included in Section 3.3.2.

For all metallicity cases, we find that increasing F_* or U prompts higher electron temperatures. From each panel of Fig 3.1, we see that the overall electron temperature rises with depletion strength (the purple lines are at the lowest temperature values, and the temperature gradually climbs up to the yellow lines per panel). This is due to the fact that F_* increasingly depletes the gas-phase abundances of coolants.

Moreover, we find that the correlation between electron temperature and ionization parameter is a result of more H photoionizing interactions that heat the gas with higher values of U . In contrast, increasing $(\text{O}/\text{H})/(\text{O}/\text{H})_{\odot}$ cools down the system, as this amplifies the abundance of coolants (compare plotlines of each colour between the three panels in Fig 3.1).

A higher $(\text{O}/\text{H})/(\text{O}/\text{H})_{\odot}$ gives rise to a greater variation in temperature as a function of F_* . This effect is observed in Fig 3.1, where the plot lines span a bigger range of temperatures moving down the panels. Increasing $(\text{O}/\text{H})/(\text{O}/\text{H})_{\odot}$ results in a larger fraction of element abundances being condensed into dust grains i.e. more heating by grains. As such we find that metallicity makes the temperature of the H II region more sensitive to changes in F_* .

For a given $(\text{O}/\text{H})/(\text{O}/\text{H})_{\odot}$, temperature changes become increasingly smaller with F_* . In each panel of Fig 3.1, when comparing the spacing of the plot lines between the different values of F_* , the spacing becomes smaller with F_* . This is a direct result of the depleted fraction of an element X being modeled by an exponentially decreasing function, $10^{B_X + A_X(F_* - z_X)}$ where $A_X, B_X < 0$. Hence for larger F_* values, the temperature of the H II region becomes less sensitive to the depletion strength.

The final observed effect is that the location of the hydrogen ionization front is affected by all three variables F_* , $(\text{O}/\text{H})/(\text{O}/\text{H})_{\odot}$, and U . The H ionization front is the boundary where the neutral ISM (a.k.a H I region) meets the edge of the H II region, and so its location is affected by the abundance of photons available to ionize the gas. In addition, the Strömgren length L of an ionized layer is related to the ionization parameter via the following equation,

$$L = \frac{Uc}{n_p \alpha_B(T_e)}, \quad (3.6)$$

where,

$$\alpha_B(T) = \begin{cases} 2.90 \times 10^{-10} T_e^{-0.77}, & T_e \leq 2.6 \times 10^4 \text{ K} \\ 1.31 \times 10^{-8} T_e^{-1.13}, & T_e > 2.6 \times 10^4 \text{ K} \end{cases}, \quad (3.7)$$

(Bottorff et al., 1998; Ferland, 1980). First of all, our study has confirmed that raising U results in a larger ionized layer, as can be observed from the H front at continuously larger depths going from the right to the left of Fig 3.1. This is understood by the fact that greater ionization parameters expand the H^+ layer by ionizing more H atoms. Secondly, we can see from Fig 3.1, the electron temperatures of our model H II region ranges from 2500 K to 20 000 K. So, for a constant ionization parameter (in the range $10^{-4} \leq U < 10^{-2}$), any positive changes in temperature result in a lengthened L according to equations (3.6) & (3.7) (a result of an increase in the rate of H ionization collisions). This is exactly the result observed in the center and rightmost panels of Fig 3.1. In contrast, our figure shows the opposite trend at $U = 10^{-2}$. At the large U limit of over 10^{-2} , grains dominantly absorb the ionizing photons, instead of hydrogen (Bottorff et al., 1998). Since a larger depletion strength results in a larger dust abundance, a greater fraction of ionizing photons are absorbed by those dust grains, leading to the Strömgren sphere shrinking. This is the trend reflected in the leftmost panels of Fig 3.1, where we observe the H ionization front occurring at

shallower depths with increasing F_* . This is also the trend observed in Chapter 2, in which $\log U = -1.48$. Lastly, since metallicity increases the abundance of dust grains and reduces the temperature, the H ionization front occurs at shallower depths, for any given U and F_* .

We conclude that electron temperature is anticorrelated to metallicity, while directly correlated to the depletion strength and ionization parameter. In addition to the F_* to electron temperature relation already established in Chapter 2, here we include the relations to two additional parameters that are fundamental to H II regions. We shall see in the next two sections (Section 3.3.3 and Section 3.3.2) that these results follow from changes to coolant abundances, with $(\text{O}/\text{H})/(\text{O}/\text{H})_\odot$ and F_* working in tandem. Furthermore, the dependency of the electron temperature on F_* seems to change with F_* itself and $(\text{O}/\text{H})/(\text{O}/\text{H})_\odot$. Moreover, we shall see that the sum of coolant line strengths is affected by depletion strength in a similar trend to how electron temperature is affected by F_* . Finally, we have discovered two regimes of how F_* affects the location of the H ionization front based on the ionization parameter. In Chapter 2, we had already observed the high ionization parameter behaviour – the depth of the H front being anticorrelated to F_* . Here we find the second regime, where at low ionization parameters, the depth of this ionization front is positively correlated to F_* .

3.3.2 Effect of depletion strength on emission line intensities

The heavy element atoms in the gaseous state of H II regions collide with free electrons, and the atomic electrons become excited. An emergent emission line spectrum from the gas results from the deexcitation of these electrons. Since the depletion strength affects the abundance of atoms available for these collisions, and the temperature of the gas which in turn affects the rate of these collisions, we expect that changing F_* will affect the emission spectrum emergent from the H II region. Evidence of this behaviour was presented in Chapter 2, where we found two competing effects in the Orion model. We found that increasing the depletion of heavy elements, weakened the corresponding line intensities i.e. the intensity of S2; increasing the abundance of grains, while depleting coolants, increased the temperature which thereby enhanced the collisionally excited line ratios corresponding to minimally depleted elements i.e. the intensities of R3, N2, and O1. Here, we include a fourth emission line ratio $\log([\text{S III}] \lambda 9530/\text{H}\alpha)$ to confirm the behaviour of emission lines corresponding to ions of sulfur.

In comparing the line ratios of the different ions in Fig 3.2, we observe that the S2 and S3 ratios (which are related by a factor, for all depletion strengths) exhibit different trends to the ratios of other ions. Similar trends were observed for Orion, in Chapter 2. For $(\text{O}/\text{H})/(\text{O}/\text{H})_\odot < 1$, these two lines are more strongly anticorrelated to F_* , than the other lines are. In the previous section, it was found that F_* has little effect on temperature, as seen in Fig 3.1. This is indicative of line ratio trends being predominantly a result of the selective depletions of heavy elements at low metallicities. Hence the emission line ratios corresponding to heavily depleted elements reduce with F_* .

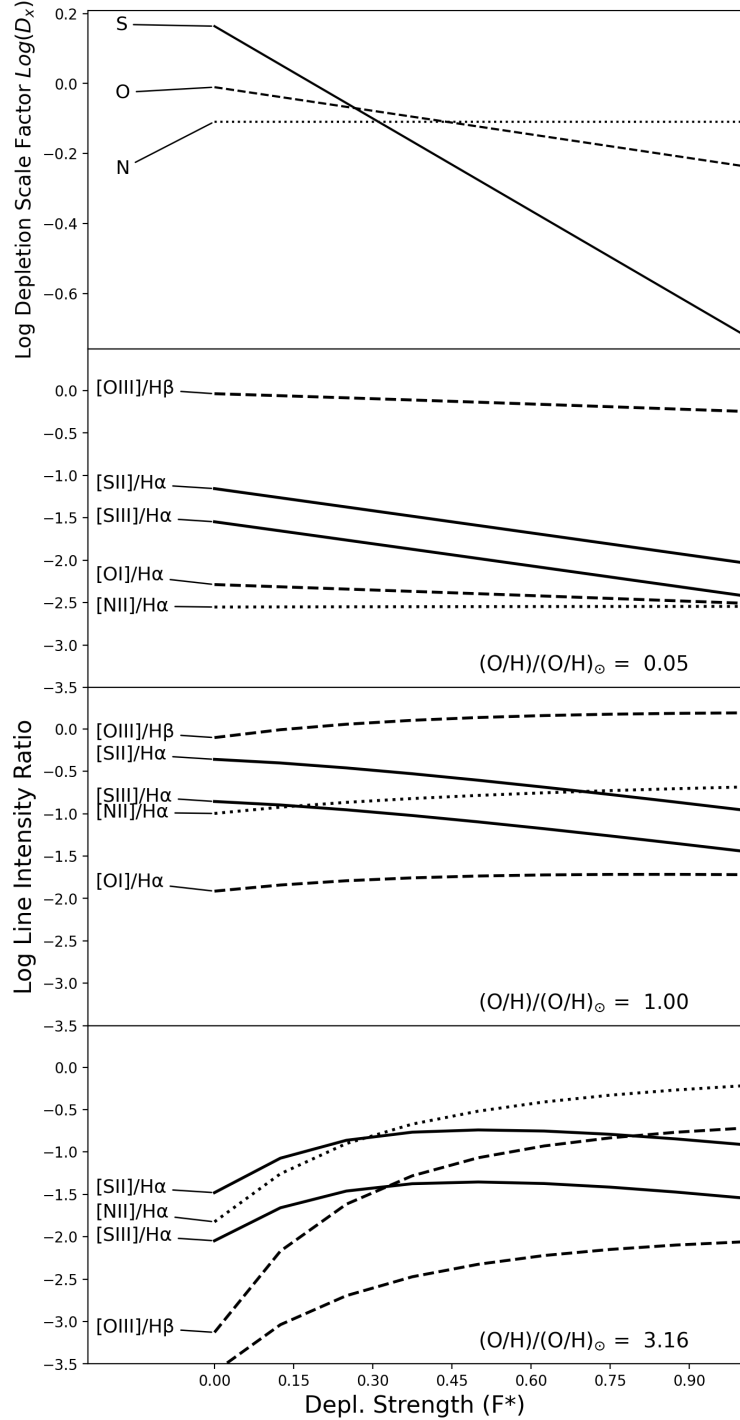


Figure 3.2: Top panel: the depletion scale factor calculated from the Jenkins09 depletion model, and multiplies the reference abundance in logarithm scale as a function of F_* . The depletion scale factor D_X is defined using $(X_{gas}/H)_{F_*} \equiv (X/H)_\odot D_X$. In the case of the Jenkins09 depletion model we have that, $\log(D_X) = B_X + A_X(F_* - z_X)$. Bottom three panels: line ratio intensities obtained from the CLOUDY model predictions as a function of F_* , for the three different metallicity values indicated. These line ratios correspond to fixed ionization parameter at $\log(U) = -3.0$.

At higher metallicities than the reference abundances, N2, O3, and O1 are more strongly correlated with F_* in comparison to S2. Additionally, there is a transition from a linear relation with F_* to a non-linear one. Recall from Section 3.3.1 at high $(\text{O}/\text{H})/(\text{O}/\text{H})_{\odot}$, we observed a significant change in the temperature of the gas with F_* , and that they have a non-linear relation. As the line ratios are seen to reflect the same trend with F_* as the temperature does, at $(\text{O}/\text{H})/(\text{O}/\text{H})_{\odot} > 1$, we find that the temperature of the gas dominantly affects the line ratios. This is evident in the fact that according to the Jenkins09 depletion pattern, F_* does not influence the depletion of nitrogen. However, at the reference and higher metallicities, the N2 line ratio intensifies with an increase in F_* as a result of a higher rate of collisional deexcitations with temperature.

Finally for the highest metallicity case and $\log(U) = -3$, we find that there is a shift in the dominant coolant as sulfur becomes heavily depleted at high F_* . At $(\text{O}/\text{H})/(\text{O}/\text{H})_{\odot} = 3.16$ and $F_* = 0$ our model outputs tell us that sulfur is responsible for 19.8 per cent of the total cooling while oxygen and nitrogen is responsible for < 1 per cent cooling each (the top panel of Fig 3.2 shows that here, there is little to no depletion in S compared to O and N). Increasing F_* to 1, increases the fraction of total cooling by both oxygen and nitrogen to 17.5 per cent each, while sulfur reduces to 5.5 per cent of the cooling (the top panel of Fig 3.2 shows that, here S is much more heavily depleted than O and N). This is apparent in the bottom panel of Fig 3.2. At high $(\text{O}/\text{H})/(\text{O}/\text{H})_{\odot}$ and high F_* , while all other line ratios increase with F_* , both S2 and S3 decrease. As the temperature plateaus with increasing F_* , the total rate of cooling should also plateau with F_* . However, at this level of depletion, sulfur is heavily depleted, making oxygen and other less depleted coolants dominate the cooling mechanisms.

In conclusion, there are two competing effects on the emission line spectra as a function of depletion strength, based on the metallicity. At low metallicities, the dominant effect on the line intensities is caused by the change in abundance pattern with F_* . This was the regime observed in Chapter 2 in the Orion Nebula. While at high metallicities the dominant effect on the line intensities is caused by variations in temperature with F_* . Finally, there is a shift in oxygen and nitrogen becoming one of the dominant coolants as F_* increases and sulfur along with other heavily depleted coolants become unavailable to maintain the rate of cooling.

3.3.3 Effect of depletion strength & ionization parameter on BPT-like diagnostics

The ionization parameter, being the ratio of ionizing photon flux to gas density, directly affects the intensity of H recombination lines. In contrast, depletion strength directly affects the grain abundance in the H II region. Since Hydrogen and dust grains affect the thermal balance of the gas (as seen in Section 3.3.1), we expect U and F_* to exhibit competing effects on the emergent line intensities, thereby affecting BPT diagnostic plots. In Chapter 2, we found that increasing F_* increased the temperature and thus strengthened the collisionally excited lines of minimally depleted elements

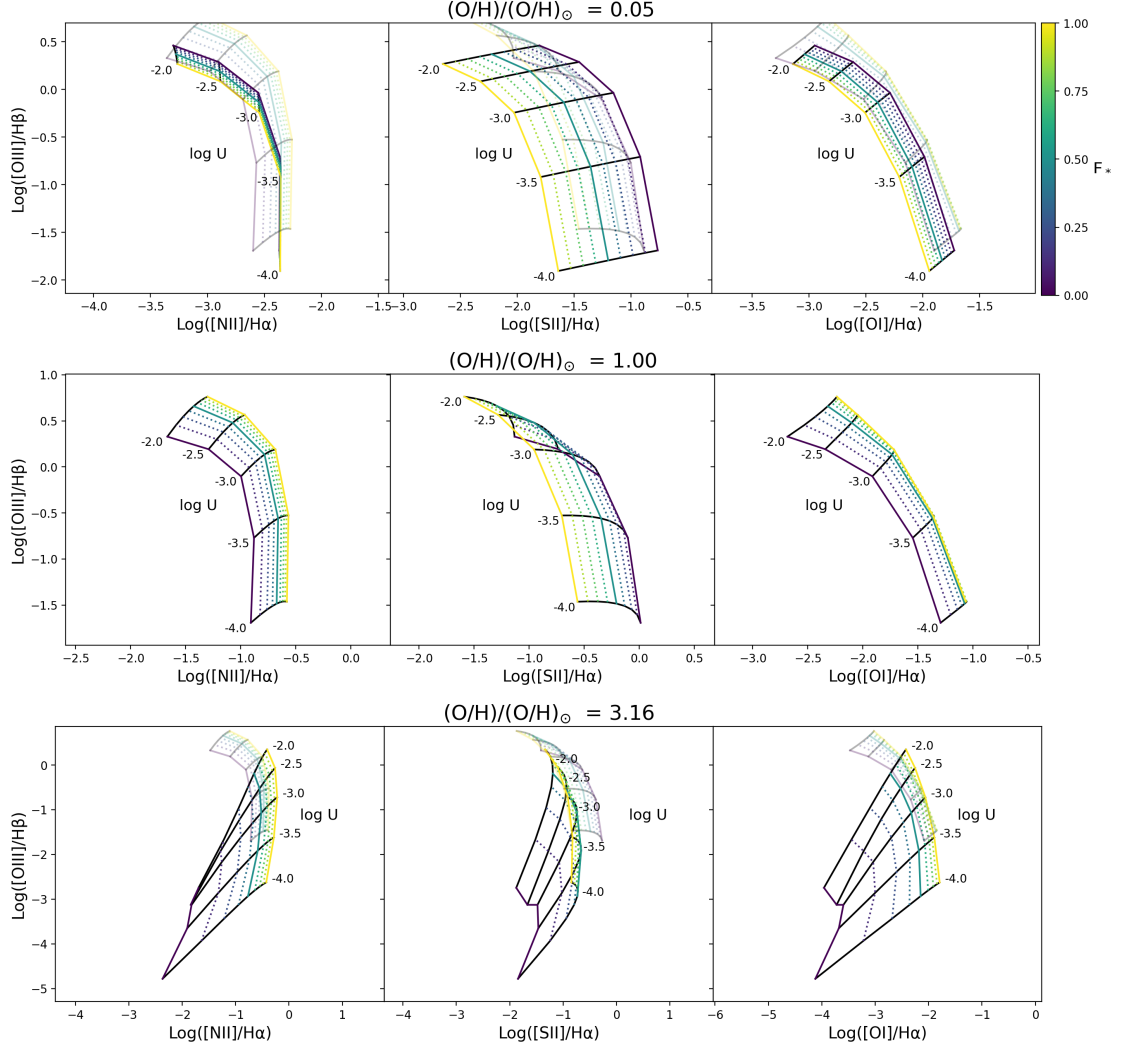


Figure 3.3: BPT-like plots using the spectral line ratio predictions for models of varying $(O/H)/(O/H)_{\odot}$ (top to bottom rows of plots), varying depletion strength F_* (coloured lines), and varying U (black lines) in [N II]-, [S II]-, and [O I]-BPT diagrams. The line ratios for varying F_* are the same ones depicted in Fig 3.2, and the colour coding for models of varying F_* is the same as that in Fig 3.1. Ghost plots of the reference metallicity (middle row) plots are included in the background of the highest (bottom row) and lowest (top row) metallicity plots to facilitate comparisons.

in the Orion Nebula. Here we study the effects of varying an additional parameter U along with F_* on a generalized H II region.

Optical BPT diagnostic diagrams composed of pairs of strong optical emission line ratios are very powerful in distinguishing different ionized regions in galaxies (H II regions, active galactic nuclei, low-ionization nuclear emission line regions, etc.). In order to understand how dust depletion affects this diagnostic diagram in Fig 3.3, we present BPT plots of our models with varying U and F_* in the [N II]-, [S II]-, and [O I]-BPT diagrams. These graphs are constructed for the three metallicities listed as before, and the colour coding for F_* remains the same as that in Fig 3.1. The results for fixed U are represented by the black plot lines, and those for fixed F_* are represented by the coloured plot lines.

Fig 3.3 shows that, at all three metallicities, both U and F_* work in tandem to affect the spectral line ratios. We find that U is more strongly correlated to R3 than the other line ratios presented in this study (the black plot lines span a wider range of R3 intensities than the other line intensities). This is a result of R3 having a much higher ionizing potential than N2, S2, or O1. At low metallicities, since F_* has little effect on R3, we find that varying F_* does little to change the behaviour of the line ratios as a function of U . However, at high metallicity, since both U and F_* are most strongly correlated to R3, the shape of the emission ratio, U plot changes non-trivially with the value of F_* . In this regime, increasing F_* enhances the effects of U on R3, while diminishing its effects on the other emission ratios.

A second prominent feature of this figure is that the $(\text{O}/\text{H})/(\text{O}/\text{H})_{\odot}$ affects whether F_* and U are positively or negatively (anti-) correlated with the emission line ratios. U is anticorrelated to N2, S2, and O1 line strengths at the lowest $(\text{O}/\text{H})/(\text{O}/\text{H})_{\odot}$, while F_* is anticorrelated with only S2 and O1. There is no change in N2 with F_* and R3 increases with both U and F_* . In contrast at the highest $(\text{O}/\text{H})/(\text{O}/\text{H})_{\odot}$, both F_* and U are positively correlated with the line intensity ratios. Increasing the overall degree of ionization in the gas cloud results in more ionized atoms available for collisions with free electrons intensifying the emission lines. At high $(\text{O}/\text{H})/(\text{O}/\text{H})_{\odot}$, the amount in which the low and high-ionization lines are intensified relative to the Balmer lines is greater. Finally, at the reference $(\text{O}/\text{H})/(\text{O}/\text{H})_{\odot}$, N2, and O1 are directly correlated with F_* , and S2 is anticorrelated with F_* – a combination of the effects we see at the high and low $(\text{O}/\text{H})/(\text{O}/\text{H})_{\odot}$ extremes.

In conclusion, we have found that all three parameters – F_* , U , and $(\text{O}/\text{H})/(\text{O}/\text{H})_{\odot}$ affect how variations in the other two parameters change the shape of the BPT-diagnostic plots. Thus, in order to constrain F_* in an ionized region, we must also constrain both metallicity and ionization parameter. In Section 3.4, we provide a discussion on constraining F_* for a set of H II regions obtained from the MaNGA survey, by comparing the observed data to our photoionization model predictions.

3.4 Impact of varying F_* on optical emission-line diagnostics of observed ionized regions

Photoionization models set the theoretical basis for defining the demarcation lines in BPT diagrams (e.g. Kewley et al. (2001, 2006)), and can be used to calibrate the

physical properties of ionized clouds based on the observed ratios of strong emission lines (see Kewley et al. (2019b), and references therein). The intrinsic shapes of the photoionization models in different emission-line ratio spaces also offer a possibility to define new diagnostic diagrams that orient the models in desired positions, thus facilitating constraints on the model parameters (Vogt et al., 2014; Ji and Yan, 2020).

Despite the great success of the BPT diagrams and their variants, the details of the built-in assumptions, including the intrinsic variations in ionizing sources and ionized regions in the same class, are seldom examined carefully. As we have seen in previous sections, variations in the depletion factor F_* result in a non-trivial change in the observed line ratio, depending on the species of ions involved. Quite often a single set of depletion factors is assumed in practices of comparing photoionization models with observational data. This effectively enforces a single F_* value for the entire sample. Therefore, it is important to understand whether a single F_* suffices to describe the general population of a class of ionized regions (e.g. H II regions).

In this section, we aim to select a sample of observed H II regions and constrain F_* by comparing them with the CLOUDY models we computed in this work. Our data are drawn from SDSS-IV MaNGA (Bundy et al., 2015; Yan et al., 2016), which includes a great number of H II regions to large effective radii. The primary sample galaxies in MaNGA are observed out to at least $1.5 R_e$, and the secondary sample galaxies are observed out to at least $2.5 R_e$ (Wake et al., 2017). We use the public data of MaNGA, which is part of the 15th data release of SDSS (Aguado et al., 2019, DR15). Fig. 3.4 shows the distribution of MaNGA’s spatial pixels (spaxels) in the three most widely used BPT diagrams. For these sample spaxels, the signal-to-noise ratios (S/N) of H α , H β , [S II] $\lambda\lambda 6716, 6731$, [N II] $\lambda 6583$, [O I] $\lambda 6300$, and [O III] $\lambda 5007$ are all required to be greater than 3. One can see that the original extreme starburst lines proposed by Kewley et al. (2001) are not very good representations of the upper envelopes of H II or star-forming (SF) regions in these diagrams. As noted by Belfiore et al. (2016) and Law et al. (2021), H II regions residing in large radial positions in galaxies can cross the extreme starburst lines in the [S II]- and [O I]-BPT diagrams. In light of this, we select a sample of H II regions not based on the original BPT diagrams, but using the three-dimensional diagnostic introduced by Ji and Yan (2020). In brief, we inspect the data distribution in a 3D space spanned by $\log([\text{N II}]/\text{H}\alpha)$, $\log([\text{S II}]/\text{H}\alpha)$, and $\log([\text{O III}]/\text{H}\beta)$, and fit a demarcation surface that sits between a fiducial SF photoionization model and a fiducial AGN photoionization model, where at roughly 90 per cent of the H α intensity is contributed by SF. The final sample bounded by the demarcation surface is coloured in green and yellow, while the rest of the spaxels are coloured in black and white. The projected demarcation lines in the original BPT diagrams are further out compared to the demarcation lines of Kewley et al. (2001), Kauffmann et al. (2003), and Stasińska et al. (2006), but close to the empirical demarcations obtained by using the kinematics of ionized gas (Law et al., 2021).

Comparing the three SF models we computed in this work (which are plotted as two dimensional grids spanning a range of metallicities and ionization parameters) to the data, we can see that in the [N II]-BPT diagram, the model with $F_* = 0.5$ is closest to the center of the SF locus. Since the depletion factor of nitrogen is almost independent of F_* , the change of the model grid along the x -axis is purely

a result of changing electron temperature. As F_* becomes larger, T_e increases and thus the model is moving rightwards. The change along the y -axis is only obvious at median-to-high metallicity, which we have already seen in Fig. 3.2. Interestingly, in the [S II]-BPT diagram, the trend with F_* is reversed. The depletion in sulfur overwhelms the increase in T_e . It now appears that the model with zero depletion provides the best-fit. It is noteworthy that in practices of photoionization modelling of H II regions, sulfur is usually assumed to have zero or negligible depletion. While in this work, our adopted relation describes a significant depletion of sulfur even when $F_* = 0.5$. Jenkins09 warned that the determination of the depletion of sulfur through observations of stellar absorption might suffer from saturation of sight lines. Therefore, there are still uncertainties associated with the prescription for sulfur. Regardless, our current set of comparisons shows that the observed H II regions in the [N II]-BPT diagram prefer the model with $F_* = 0.5$, while the same H II regions in the [S II]-BPT diagram prefer the model with $F_* = 0$.

The [O I]-BPT diagram is the most interesting but also the problematic one. First of all, the extreme starburst line cannot bound a large number of H II regions identified using the other two diagrams. In addition, current photoionization models fail to fit this upper envelope of the data as well (see e.g. Law et al. (2021)). Despite the change of the model points at low and high metallicities with increasing F_* , the upper envelopes of the models remain nearly unmoved. This is indicative of a balance between the increasing depletion of oxygen and the decreasing abundance of oxygen at fixed metallicity near the envelope, which also shows that the depletion factor is not the culprit for the mismatch between the models and data.

Fig. 3.5 compares the models to the data distribution in a reprojected BPT diagram. This diagram uses linear combinations of the logarithms of the BPT line ratios ($[\text{N II}]/\text{H}\alpha$, $[\text{S II}]/\text{H}\alpha$, and $[\text{O III}]/\text{H}\beta$) to place photoionization models on a nearly edge-on view, which puts strong constraints on the locations of the models (Ji and Yan, 2020). One can easily see how well the model grids trace the center of the SF locus. The colour coding of the density distribution of the data is the same as in Fig. 3.4. The left-hand panel of Fig. 3.5 compares models with different values of F_* . While the model with $F_* = 0.5$ shows the best consistency with the SF locus, it still shows obvious deviation from the upper part of data locus, which corresponds to H II regions with low metallicities. As F_* increases, the model grid moves down along the P_2 axis but only moves to the right a little at high metallicity. This is because the changes in $[\text{N II}]/\text{H}\alpha$ and $[\text{S II}]/\text{H}\alpha$ have opposite signs and thus add up along P_2 , while canceling out along P_1 . In the meanwhile, the change in $[\text{O III}]/\text{H}\beta$ is only significant at high metallicities due to the competing effect of oxygen depletion and overall cooling efficiency. As a result, the model grid exhibits a nearly vertical motion in the plane. We note that our best-fitting value of F_* is consistent with the work by Kewley et al. (2019a), who adopted $\log(Fe_{gas}/Fe_{total}) = -1.5 dex$ for their ISM models. This value is derived from their observations of H II regions in the Milky Way and Magellanic Clouds using the Wide Integral Field Spectrograph and corresponds to $F_* = 0.43$.

Based on our choice of input parameters, the model with $F_* = 0.5$ still cannot fit H II regions at all metallicities in the MaNGA sample. The uncertainty in the deple-

tion of sulfur might contribute to this offset. If we remove the sulfur depletion entirely from this model but keep the depletion strengths for other elements unchanged, we can improve the model prediction on S2 but worsen the model prediction on N2 (due to the drop in T_e). As a result, the model is shifted up in the re-projected diagram, fitting the low-metallicity SF locus slightly better, but fitting the rest of the SF locus worse. Meanwhile, we note that the sulfur depletion pattern itself, if set as a free parameter, cannot be well determined due to its degeneracy with other nebular parameters.

The choice of the reference abundance set as well as the abundance pattern for the secondary elements could play a role, as it directly influences the overall abundances of different elements. For example, tuning the N/O abundance pattern can compensate the loss in N2 due to the lowered sulfur depletion. In the right-hand panel of Fig. 3.5, we show a model with $F_* = 0.5$ but without sulfur depletion. Using an N/O abundance pattern derived by Schaefer et al. (2020), we are able to make this model fit the whole SF locus much better compared to the models in the left-hand panel. The N/O abundance pattern of Schaefer et al. (2020) was derived using the observed $[\text{N II}] \lambda 6583 / [\text{O II}] \lambda \lambda 3726, 3729$ in MaNGA H II regions. The similarity of the model to the model constructed by Ji and Yan (2020) indicates degeneracy between the depletion pattern and the abundance pattern for N/O. When other model parameters are fixed, as long as the depletion patterns of the major coolants in the optical, in this case N and O, and the input N/O prescriptions prior to depletion produce similar post-depletion abundances for N and O, the resulting relevant line ratios will be similar. Without other independent constraints from observations, it is difficult to break this degeneracy in the model. It is noteworthy that under the depletion scheme we adopted, we need to remove sulfur depletion in the model in order to produce a better fit to the data.

Despite the aforementioned importance of the sulfur depletion, there are few observational constraints on its strength. Sulfur is often considered as an element of zero depletion when modelling the ISM. However, according to Calura et al. (2009), a sulfur depletion of ~ 0.1 dex is needed to explain the N/S ratio of the gamma-ray burst (GRB) host galaxies in their sample. On the other hand, the measurement of the local sulfur depletion in different sight lines suffers from small numbers of reliable determinations. The relation obtained by Jenkins09 using these observations predicts a significant depletion of ~ 0.4 dex for sulfur when F_* is only 0.5. Judging from Fig. 3.4 and Fig. 3.5, it is likely that the depletion of sulfur has been overestimated. Whereas we also need to be aware of the degeneracy between the sulfur depletion strength and the abundance patterns of other elements. As an important coolant in the H II regions, the abundance of sulfur affects the thermal balance of the clouds and thus is also connected to the strength of other collisionally excited lines. Its depletion pattern might also be related to the long standing problem of the overestimation of $[\text{S III}] \lambda \lambda 9069, 9531$ by photoionization models (e.g. Garnett (1989); Badnell et al. (2015); Mingozi et al. (2020)). To fully settle this issue, we need more direct constraints on the abundance of sulfur as well as other elements in H II regions from observations in the future.

Given the degeneracy between the depletion pattern and the N/O prescription we

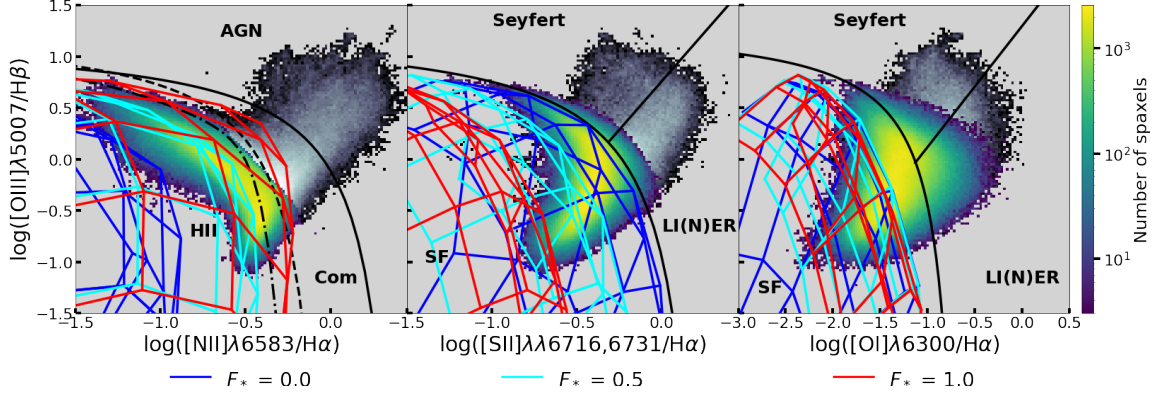


Figure 3.4: Photoionization models with $F_* = 0.0, 0.5,$ and 1.0 plotted in the [N II]-, [S II]-, and [O I]-BPT diagrams. The model grids are plotted by independently varying the metallicity and the ionization parameter. A sample of spatially resolved data from MaNGA is shown in the background, with the SF regions (identified by combining the [N II]- and [S II]-BPT diagrams) coloured from yellow to green, and the rest of the ionized regions coloured from white to black. We also plot demarcation lines from Kewley et al. (2001) (solid black lines), Kewley et al. (2006) (solid black lines), Kauffmann et al. (2003) (dashed black line), and Stasińska et al. (2006) (dash-dotted black line) for comparison.

show, one might wonder whether other input parameters in the photoionization model such as the ionizing spectral energy distribution (SED) could produce degeneracy as well. While changing F_* mainly shifts model along the P_1 axis in the P_1 - P_2 diagram, changing the hardness of the ionizing SED mainly shifts the model grid in a nearly perpendicular direction along P_2 (see e.g. Figure 7 of Ji and Yan (2020)). Specifically, a harder SED for SF regions enhance both the high-ionization lines and low-ionization lines, thereby shifting the model to the right in this diagram and push it away from the SF locus. A similar effect can be seen in the original BPT diagrams (e.g. Byler et al. (2017); D’Agostino et al. (2019)). On the other hand, fixing other parameters while changing the stellar ionizing SED cannot make the model with the F_* depletion pattern to fit the SF locus significantly better compared to what is shown in the left-hand panel of Fig. 3.5. Therefore, the variation in the ionizing SED is unlikely to produce significant degeneracy with the depletion strength and depletion pattern.

Finally, the dust composition is an interesting ingredient in the model which we have not discussed in detail thus far. We discuss the model assumption in the dust composition in the next section.

3.5 Discussions

The grain physics in CLOUDY has its own separate code (see Ferland et al. (2017) Section 5 and Ferland (2006) Section 7.9 for further information). CLOUDY incorporates 20 different standard grain types, some of which are graphite and some are silicates. The grain composition used by CLOUDY is one that is consistent with the

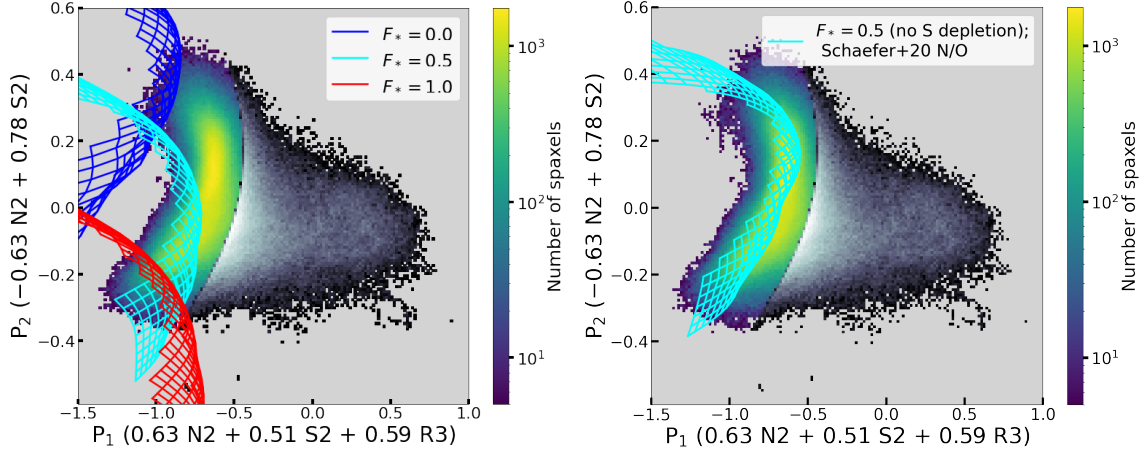


Figure 3.5: Distribution of MaNGA data in a specific projection (P_1 - P_2 projection; Ji and Yan (2020)) of a three-dimensional line ratio space. Here N2, S2, and R3 stand for $\log([\text{N II}]/\text{H}\alpha)$, $\log([\text{S II}]/\text{H}\alpha)$, and $\log([\text{O III}]/\text{H}\beta)$, respectively. The two axes P_1 and P_2 are linear combinations of N2, S2, and R3. The projection was constructed in a way that makes the data locus and the model appear nearly edge-on. The model grids are also projected into this plane but are first interpolated and then truncated so that only the parts of the models that cover the middle 98 percent of the data along the third dimension perpendicular to both P_1 and P_2 axes are shown. *Left:* Model grids with different F_* values. *Right:* A model grid with $F_* = 0.5$ but without depletion of sulfur onto dust grains. In addition, different from the models in the left-hand panel (whose parameters other than F_* are summarized in Table 3.2), it adopts an N/O versus O/H relation derived by Schaefer et al. (2020).

required A_V/n_H (an average for extragalactic H II regions), which is the ratio of total extinction to hydrogen density. A mixture of different grain types provides a composition which helps describe an average of properties of extragalactic H II regions. Although the grain physics in CLOUDY was encoded separately from applying the Jenkins09 depletion model, this model should still be relevant because it simply lets us how to alter the relative amount of depleted material. We then use these post-depleted abundances in the grain physics calculations. Note currently, the depleted abundances from gas-phase are not necessarily consistent with the abundances in dust-phase. It is difficult to make a fully consistent prescription that takes into account both element depletion and grain composition. However the most realistic and self-consistent a treatment to do so thus far, is by scaling the amount of dust based on the F_* value. This is investigated and discussed in the Paper I. The current study utilizes this method for all of the simulations presented.

Checking if the depleted material is consistent with the material forming the grains is a next step. Since Jenkins09 depletion model was originally developed from observations of neutral clouds, we may first need to build a depletion pattern for H II regions similar to the Jenkins09 model – a discussion on this particular fact is also presented in the Paper I.

Finally, note the same analysis as presented in this study can be carried out using

fixed nebular metallicity (i.e. fixed post-depletion gas-phase metallicity). To do this with CLOUDY the F_* value in the command line of the input model can be kept constant while scaling the dust according to various values F_* . The final result will be equivalent to the ones discussed in this investigation.

3.6 Conclusions

The primary objective of this study was to explore how varying the collective depletion strength F_* , affects the predicted line ratios of a generalized photoionization model. The goal is to help us understand how dust depletion may affect spectral observations as well as provide a constraint on the value of F_* when modelling a collection of H II regions.

While it has been long suspected that dust depletion affects the observed line ratios, previous work has not explored the details nor realized the extent of its effects on emission line spectra of H II regions. This study has found that spectral line ratios of ionized regions vary non-trivially with the change in depletion strength, especially in R3, S2, and O1. Furthermore, our model predictions indicate that the line ratios are varied by a balance between metallicity, ionization parameter U , and depletion factor F_* . Metallicity varies the abundance of all elements, while the depletion factor varies fractions of element abundances selectively.

At low metallicities, temperatures of the gas are high compared to those at high metallicities, as a result of low coolant abundances. However, there is little variation in temperature as a function of F_* , so the trends in emission line ratios are dominated by changes to the depletion strength. Likewise, in this regime, the effects of U on the emission line ratios change little with F_* (F_* with S2 and U with R3). Hence the BPT diagrams spanning a smaller range of line ratios than at higher metallicities stipulate that F_* may be constrained independent of U at metallicities lower than the reference set.

At metallicities greater than the reference values, although the electron temperatures are lower, there is significant variation in temperature as a function of depletion strength. In this regime, changes in F_* result in a significant change in the thermal equilibrium of the gas. As a result of this, collisional excitation rates are increased enhancing the emission line ratios. Here, variations in the electron temperature dominate the emission line ratio trends. Unlike at lower metallicities, F_* enhances the trends of the line ratios with U and vice versa. Hence, U must be constrained in order to constrain F_* , as the effects on the BPT diagrams by one parameter is dependent on the other.

There are two regimes based on the ionization parameter how varying F_* impacts the size of the ionized region. For $\log(U) \geq -2$, since grains dominantly absorb the incident ionizing photons, the rise in grain abundance with F_* shrinks the ionizing layer. For $\log(U) < -2$, since H atoms dominate in absorbing the ionizing photons, the gas becoming hotter with F_* expands the ionized region. Due to this effect, we conclude that even at low metallicities, U must be constrained in order to constrain F_* .

Finally, comparing our photoionization models with the data from the MaNGA survey revealed a preferred depletion factor for this collection of H II regions. The best-fitting value of depletion factor for this particular group of H II regions correspond to $F_* \approx 0.5$ as revealed by the [N II]- and the re-projected BPT diagrams. However, our photoionization models in this study still fail to fit the observed N2, S2, and O1 simultaneously, especially at low metallicities. Removing the sulfur depletion and adopting a different N/O pattern make the model with $F_* = 0.5$ fit the data locus better, which also reveals the degeneracy between the depletion pattern and the N/O pattern. To solve this issue, we need direct constraints on the depletion of sulfur and a deeper understanding of the photoionization modelling of sulfur and oxygen lines in future works. Regardless, even though our models do not provide a perfect fit to the data, we have seen that it is still possible to put qualitative constraints F_* by selecting the model which shows the best consistency with the data locus.

The above paragraphs summarize the main conclusions borne from this study. Some additional caveats must be included to provide a complete picture:

1. Sulfur depletion: Since this depletion pattern was developed for H I regions, the depletion pattern of sulfur may not be an accurate estimation for H II regions. However, sulfur being an important coolant affects the thermal balance of the gas and consequently the emission line ratios of other ions.
2. At low values of F_* , some depletion scale factors in the pattern described by Jenkins09 attain values above unity. However, it is not physical for the abundance of any element to increase from its initial value. The present study avoids this unphysical issue by defaulting the depletion scale factors to 1, if the calculation according to Jenkins09 rises above unity at $F_* = 0$. For sulfur, the overestimated abundance could originate from the contamination from H II regions along the sight lines used to measure the sulfur abundances in the H I gas.

Chapter 4 Creating a CLOUDY-Compatible Database with CHIANTI Version 10 Data

4.1 Introduction

In astronomy, we cannot generally conduct direct experiments, so theoretical modeling becomes an essential tool in understanding and explaining observational results. CLOUDY is an open-source modeling software that simulates a broad range of conditions in the interstellar matter and predicts the emitted spectra using ab initio detailed calculations of microphysical processes (Ferland et al., 2017).

Emission line spectra may be produced via collisional excitation followed by de-excitation of atoms and ions of various elements present in the plasmas of distant objects (Spitzer, 1978). Hence atomic and molecular data are required by CLOUDY to conduct these detailed calculations.

CLOUDY currently incorporates three atomic and molecular databases: Stout (Lykins et al., 2015), CHIANTI version 7.1.4 (Young et al., 2013, hereafter Ch7), and LAMDA (Schöier et al., 2005). There have been more recent versions of CHIANTI with more accurate and extensive atomic and molecular data. However, these new versions have made major changes to the formatting of their data files, so none have been incorporated into CLOUDY thus far. CLOUDY would greatly benefit from these improvements, yet they come at the cost of modifying the source code of the software to keep up with the evolving formatting of the data. Thus, the primary goal of this paper is to reformat the latest version of CHIANTI to the format already used by CLOUDY, without having to make any changes to its source code. An ancillary objective is to keep the download size of CLOUDY manageable, requiring us to trim the database to what is essential for the operation of our code.

This paper will be arranged according to the following. In Section 4.1.1, we describe the CHIANTI database and its structure. Since the collisional data in CHIANTI are in Burgess and Tully space, we provide the relevant descaling equations for each of the six transition types. Our method of adapting the latest CHIANTI database to be used by CLOUDY and an analysis of the collisional data is provided in Section 4.2.1. Finally, in Section 4.3 we discuss the changes this new database has made to the test simulations in CLOUDY.

4.1.1 The CHIANTI Database

CHIANTI was originally released in 1996 (Dere et al., 1997). It was created using observational data taken from the best available publications at the time, and theoretical estimates of data unavailable from observations. As more accurate observations and improved atomic models have become available over the years, subsequently ten CHIANTI versions have been released. Of these, we want to include the 2021 release, CHIANTI version 10.0.1 (Del Zanna et al., 2021, hereafter Ch10) in the next CLOUDY release.

Ch10 has become an extensive atomic database containing energy level data, wavelength and radiative data, and electron excitation data for a large number of transitions per ion. The database is organized into three main data files for each ion. Energy level data are stored in files with extension names ‘.elvlc’, containing both the observational and theoretical energies. The observational energies are obtained mainly from the NIST database (Kramida et al., 2022). Transition wavelengths, Einstein A values, and oscillator strengths are stored in files with the extension ‘.wgfa’ and are obtained from the literature. For the transitions where these data are unavailable in the literature, they calculated Einstein A, and gf values using theoretical energies obtained from the literature. Lastly, excitation data containing effective collision strengths are found in the ‘.scups’ files. These data have been gathered from the literature and are recorded in Burgess and Tully space in all versions of CHIANTI (detailed discussion and how to descale provided in Appendix 7). Other auxiliary data files are available in the CHIANTI databases. However, since they are not required for any of the CLOUDY calculations, only the three file types introduced above are adapted to be used by CLOUDY and discussed in the present paper.

The Ch7 database released in 2011 is structured similarly to Ch10, with the exception of the ‘.scups’ files. In Ch7, the electron excitation data are stored in files with extension names ‘.splups’. Their file format change from .splups to .scups was to better capture the structures present in the collision strength-temperature profiles for low temperatures (further details in Section 4.2.1). Moreover, Ch10 contains many transition levels and temperature data in the ‘.scups’ that were not included in Ch7, making the former ~ 26 times the size of the latter even without the auxiliary data files.

4.2 Ingesting a Fluid Atomic Database

4.2.1 A Database Strategy

As more detailed experimental and theoretical works are published, atomic data change. Since improving atomic data will also impact the calculations made by CLOUDY, we must have a strategy for keeping up with these evolving data sets. For our Stout data, we have scripts that easily import the ADF04 ¹ format. Our goal in this work is to adopt a similar strategy for the CHIANTI database. Since CHIANTI formatting undergoes significant changes from version to version, it would take some effort to modify CLOUDY to keep up with these changes. Moreover, changing the CLOUDY source code would require someone proficient in C++ atomic data objects within CLOUDY, and finding such a person is a challenging task. Instead, we developed a strategy of converting the latest version of CHIANTI to the Ch7 format (which we have used for some time Ferland et al. (2017)) using a Python script. As the CHIANTI format changes, we can easily update our script to maintain the Ch7 formatting.

CLOUDY reads in the CHIANTI data character by character of each row of data in each file, as Ch7 has columns of data that run into each other. So our reformatted database must follow the Ch7 character spacing exactly. Table D1 shows there is

little change between the Ch7 and Ch10 formats for the ‘.elvlc’ and ‘.wgfa’ files. Reformatting these files is a simple re-organization of columns. The collisional data files require a bit more work. Unlike Ch7, which implicitly has a regularly spaced temperature grid, the grid in Ch10 is optimized to best map the data with as few points as possible. In the next section, we lay out the steps to convert the three-line Ch10 collision strengths with irregularly spaced scaled temperature into a single line with a regularly spaced grid.

We developed a Python 3 code called `chianti2oldChianti.py`. It is available at <https://gitlab.nublado.org/cloudy/arrack> (accessed on 13 July 2022)². This repository also contains a script to descale the (Burgess and Tully, 1992, hereafter BT) collision strengths and temperatures in physics space for all six CHIANTI transition types (Appendix 7).

4.2.2 Interpolating Effective Collision Strengths

To revert the Ch10 data in the ‘.scups’ files, we must interpolate onto the Ch7 regularly spaced grid while still preserving the collision strength-temperature relation as closely as possible. This can be achieved by increasing the number of spline points used.

Our script does the following, recursively, for each transition:

1. First we use `scipy.interpolate.interpld` to find a best-fit function for the log of $\Upsilon_{BT}-T_{BT}$ relation for each transition of each ion. We omit points with $\Upsilon_{BT} = 0$ and add them back in later.
2. The best-fit function is then used to interpolate the set of Υ_{BT} that corresponds to a set of evenly spaced T_{BT} points. As most of the Ch7 files contained 11 spline points, we begin by using a set of 11 Υ_{BT} points.
3. We find another function to fit the linearly spaced data with the same method as before.
4. Then using the original set of temperature points and the new best-fit function we obtain a recalculation of the original $\Upsilon_{BT}-T_{BT}$ relation.
5. The error (χ) is computed to reveal how well the interpolated data has preserved the $\Upsilon_{BT}-T_{BT}$ relation for that transition,

$$\chi = \frac{1}{N} \left(\sum_i^N \left(\frac{o_i - e_i}{e_i} \right)^2 \right)^{1/2} \quad (4.1)$$

where,

o_i i th recalculated Υ_{BT} in transition;

e_i i th original Υ_{BT} in transition;

N number of points in the transition in Ch10.

Since $T_{BT} = 1$ in BT space represents the $T \rightarrow \infty$ limit, $\Upsilon_{BT}(T_{BT} = 1)$ in Ch10 is taken to be the collision strength at the high-temperature limit. We found that this value does not always smoothly follow from the $\Upsilon_{BT}-T_{BT}$ profile, which then skews our fits. Fitting only the values for which $T_{BT} < 0.8$ provides much improved fits from using the value at the high-temperature limit.

6. Then we repeat the previous steps for the linear $\Upsilon_{BT}-T_{BT}$ relation, and use the fit that corresponds to the smaller of the two absolute relative deviations.
7. Next, a spline point is added after each iteration of this procedure that meets all of the following criteria:
 1. $\chi > 0.005$;
 2. number of spline points ≤ 60 ;
 3. $\Delta\chi/\chi > 0.001$.

The scale (linear or log) that produced the smaller error in the above step is continued to be used in the following iterations of this procedure.

We set $\chi = 0.005$, 60 splines, and 0.001 error convergence as the limits of our reformatted database. We arrived at these values with a parameter-space exploration. Values corresponding to more relaxed criteria did not yield satisfactory fits to the BT collision strength data. On the other hand, increasing the maximum allowed spline points above 60, and the χ threshold below 0.005 did little to improve our fits while increasing the size of the database larger than the original Ch10 database. As the Ch10 database is already many times larger than Ch7, we do not want the reformatting process to make it even larger. Furthermore, there are transitions for which adding more points beyond a certain number does little to improve the quality of the fit. Hence we introduce a relative χ convergence threshold of 0.001 to stop the addition of any more spline points when there is little to no improvement to χ of the interpolation. Transitions that have sharp peaks/troughs in the $\Upsilon_{BT}-T$ profile that are difficult to capture with equidistant step sizes benefit from this criteria. For example, the Ni XVII 15-125 (the transitions are identified in the data files by the lower- and upper-level indices specified in the level energy file) shown in Figure 4.1, is one such transition in which increasing beyond 15 spline points did little to improve the fit for its peak.

Statistical measures for the quality of the interpolated collision strengths in our final database are presented in Figure 4.2. The data presented are for a truncated version of the database, further discussed in Section 4.2.3. The middle panel in Figure 4.2 reveals that only a handful of transitions have $\chi > 0.5$, and fewer still have $\chi > 1.00$. We also see that majority of the data have less than 30 splines.

Our methodology produces several transitions with fewer spline points than the minimum set limit (of 11 splines). There are two main reasons for this occurrence. First, for the transitions with five spline points, the collision strength data in Ch10 is already in an equally spaced temperature grid. Second, in the cases where we remove $\Upsilon_{BT} = 0$, the offset between the point we removed and the next $\Upsilon_{BT} \neq 0$ point is

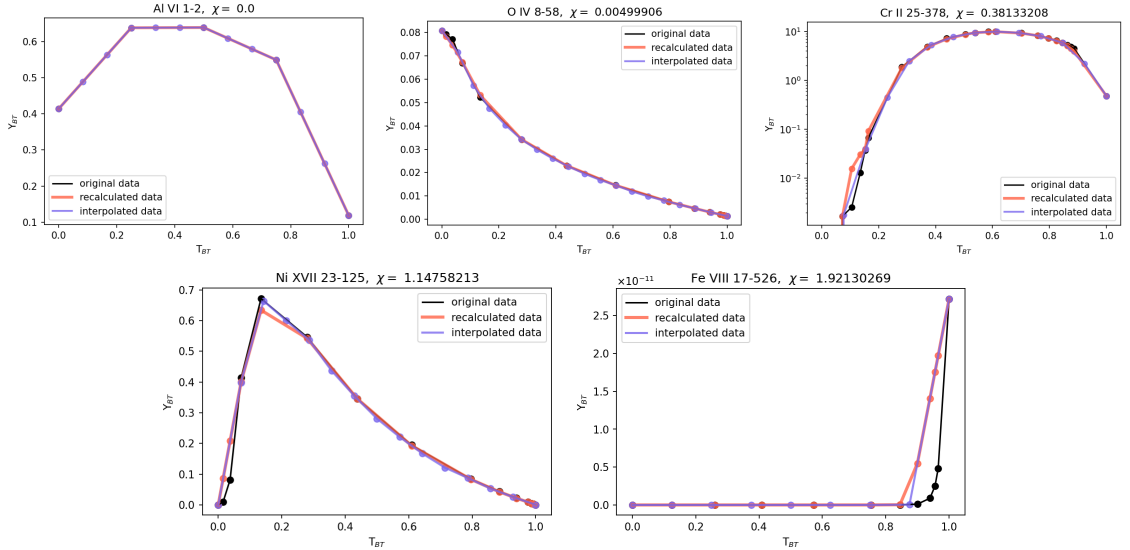


Figure 4.1: Each panel presents the collisional data of an example transition. The black plot line indicates the original data from the Ch10 database. The purple plot line indicates the evenly spaced collisional data interpolated from the original Ch10 transition. The pink plot line shows our best-fit results of the original Ch10 collision strengths.

used as the minimum step size. In some cases, this minimum step size is large enough to lead to fewer than 11 spline points.

Figure 4.1 shows four examples of transitions with varying values of χ , comparing the original set, the interpolated set and the recalculated set of Υ_{BT} and T_{BT} . Fe VIII 17-526 has the greatest χ error in the database. This is an example of a transition where the minimum step size allows for a maximum of only nine spline points. In fact, several other Fe VIII transitions with upper level 526 have this same issue resulting in $\chi > 1.0$. Ni XVII 15-125 also has a high error even though our interpolation has ended with 15 spline points. Likewise, there are several transitions in Ni XVII with upper levels of 123, 124, and 125 with 15 interpolated splines and errors > 0.5 . Due to the particular shape of the peak in these Υ_{BT} - T_{BT} profiles, the absolute relative convergence in χ drops below 0.001 at 15 spline points.

4.2.3 Data Truncation

The full reprocessed database is >15 times the size of Ch7. The larger size of Ch10 is a result of most atomic models having many levels (100–1000). A large number of these levels lie above the ionization limit of that species, and CLOUDY at the moment does not process them.

Omitting these auto-ionizing levels reduces the size of the final database. We incorporated the option to make this cut into `chianti2oldChianti.py`. It follows the procedures for reformatting Ch10 as described in the above sections, but only includes levels up to the ionization limit of that ion.

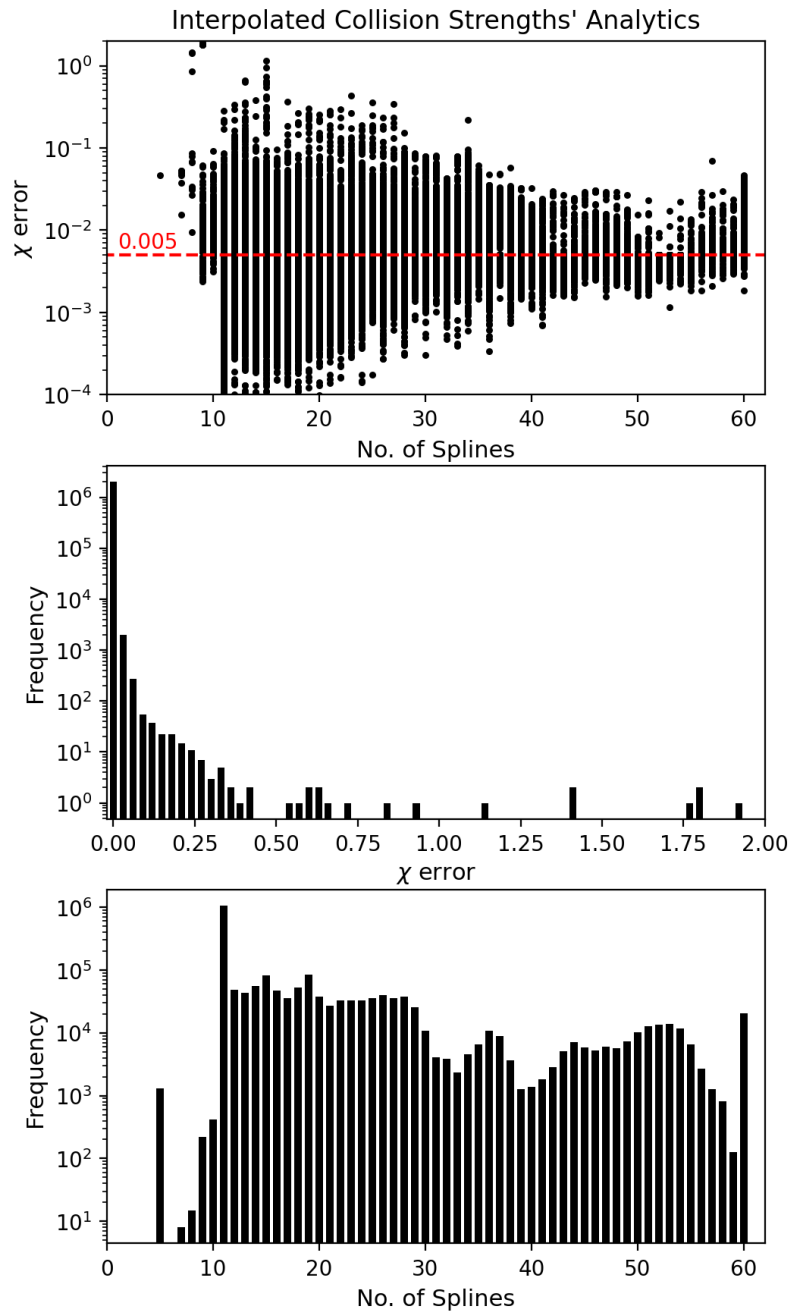


Figure 4.2: Top panel: distribution between the interpolated collision strength χ error and the number of spline points used in the interpolation, per transition. The red line in the top panel indicates the fit error limit that is set in our script that converts Ch10 format to Ch7. Middle panel: histogram of interpolated collision strength fit errors. Bottom panel: histogram of the number of spline points used in the interpolation.

Using this procedure, a truncated and reformatted version of Ch10 (hereafter referred to as NOAI) was formed, which takes up 458 MB of disk space. NOAI is $\sim 3.3\times$ smaller than the full version, $\sim 7\times$ smaller than Ch10, and $\sim 4\times$ larger than Ch07. This is a significant improvement in size and is sufficient for our purposes.

Figure 4.3 shows the quality of fits for the truncated database for transitions with $\Upsilon > 10^{-2}$. The recalculated and original collision strengths are presented here in physical space, converted from BT space using the equations in Appendix 7. This figure reveals our method reproduces the original collision strengths decently well. The middle panel of this figure shows that all the collision strengths >100 deviate by less than 10% from the original value. Although not shown in this figure, a majority of the collision strengths in NOAI deviate by less than 1%. We also find that the collision strengths with relative deviations $> 2\times$ and $\Upsilon > 10^{-2}$ come almost all from two ions—Ni XVII and Cr II. The ionization fraction of Ni XVII peaks at 3.98×10^6 K, whereas the temperature of the high deviation points in Ni XVII lies between 57,793 K and 144,035 K. Similarly, the ionization fraction of Cr II peaks at 25,119 K, while the collision strengths with high deviation for this ion lies at 1500 K. Since for both ions the ionization fraction at the temperatures of the high deviation points is far below their peaks, neither ion has an important impact on the spectral predictions. Moreover, it is only 29 collision strengths out of the total 8.6×10^6 points with $\Upsilon > 10^{-2}$ in the NOAI database that have these large deviations. Hence, this interpolation is sufficient for our simulations.

4.3 Testing the Reformatted Database: Effect on CLOUDY Models

The primary goal of this paper is to adapt the newest version of the CHIANTI atomic database to be used in the CLOUDY spectral predictions. We have accomplished this with the above-described procedures and formed a reprocessed database that can replace the current Ch7 database being used. It is now important to assess the changes this new database will induce in CLOUDY’s output. A test suite built into CLOUDY monitors various observable and physical quantities in a number of different astrophysical scenarios and reports the changes that can result from alterations to the algorithm or the atomic data.

Running the CLOUDY executable test command revealed the wavelengths of 11 electron-excitation lines had changed between Ch7 and Ch10. Since CLOUDY utilizes these wavelengths in its source code, we updated these values. A summary of the wavelength changes is provided in Table 4.1.

Running the test suite with the NOAI revealed multiple changes to physical quantities as a result of changing the atomic data. In CLOUDY, if such a difference exceeds a specified tolerance it is referred to as a ‘botch’. A summary of these variations is provided in Tables 4.2 and 4.3. The following is a discussion of the changes that produced the variation in the physical predictions.

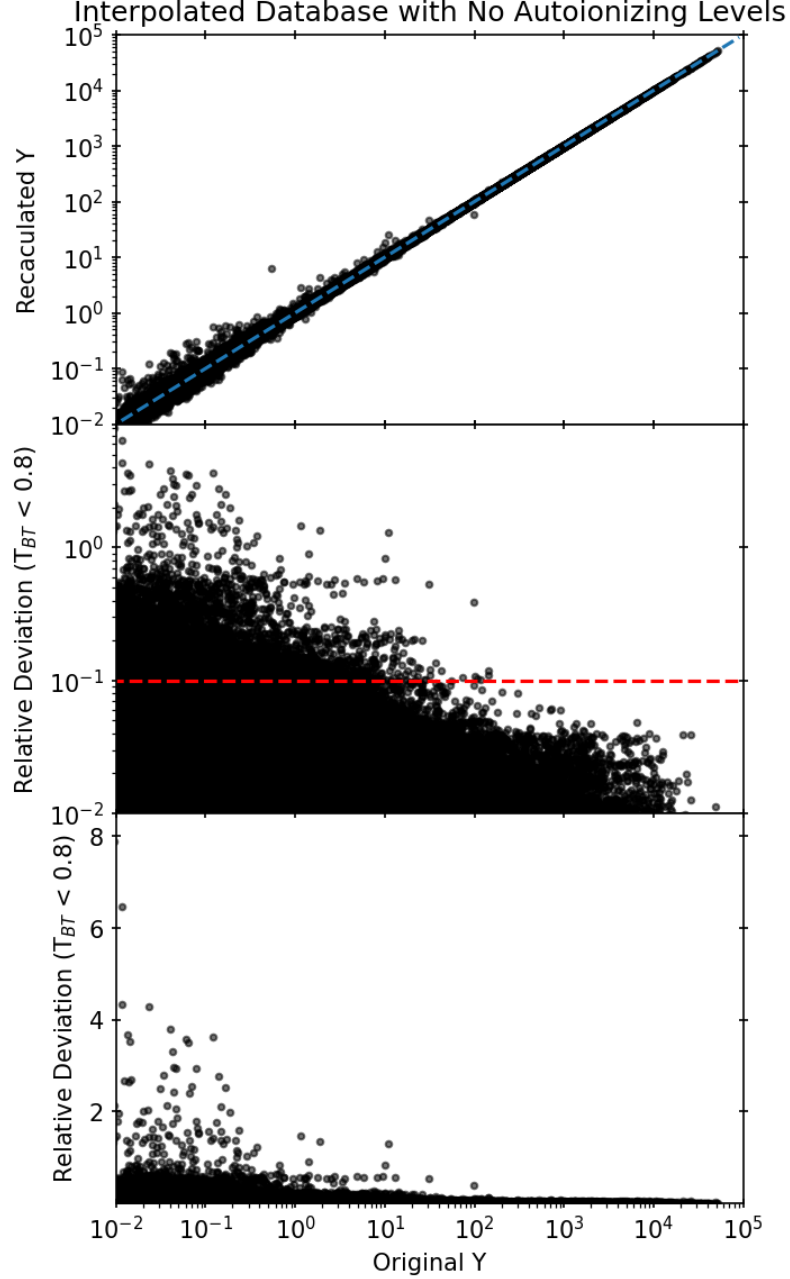


Figure 4.3: Cross-correlation between the recalculated collision strengths $>10^{-2}$ and the original Ch10 collision strengths $>10^{-2}$, both converted to physical space. The blue dashed line in the top panel is the $y = x$ plot, in our case it represents the recalculated Υ and original Υ that are in perfect agreement. The bottom two panels show relative deviation, which is the difference between each recalculated Υ and original Ch10 Υ , and divided by the latter. The red dashed line in the middle panel indicates a relative deviation of 10%. The data contained in the middle and bottom plots are the same, only differing in the scaling of the y-axis (log vs. linear).

Table 4.1: Wavelengths of electron-excitation transitions in the Ch10 database compared with the values in the Ch7 database.

Ion	Ch10 Wavelength	Ch7 Wavelength
Al XII	550.031	550.032
Al XII	568.120	568.122
Ne VIII	770.428	770.410
Ne VIII	780.385	780.325
Ne VII	887.293	887.279
Ne VII	895.191	895.174
O VI	1037.610	1037.620
O IV	1397.230	1397.200
O IV	1399.780	1399.770
O IV	1401.160	1404.780
O IV	1404.810	1404.780
C IV	1550.770	1550.780

Table 4.2: A list of the spectral lines that differ in intensity (the normalization line intensities used are $H\alpha$ & $H\beta$) due to collisional data changes between Ch7 and Ch10, as calculated with the time-steady simulations in the CLOUDY test suite.

Ion	Wavelength	Transition	Time-Steady Simulation	Relative Intensity Change	Source of Change
O IV	25.8863 μ	1-2	limit_lowd0.out	0.472	o_4.splups in CHIANTI 8
			limit_lowdm6.out	0.472	
			nlr_paris.out	0.261	
			pn_ots.out	0.183	
			pn_paris.out	0.181	
Ne V	24.3109 μ	1-2	limit_lowd0.out	-0.441	ne_5.splups in CHIANTI 10
			limit_lowdm6.out	-0.440	
			nlr_paris.out	-0.291	
			pn_ots.out	-0.228	
			pn_paris.out	-0.229	
			pn_paris_cpre.out	-0.224	

Table 4.2 – Continued from previous page.

Ion	Wavelength	Transition	Time-Steady Simulations	Relative Intensity Change	Source of Change
Ne v	14.3178 μ	2-3	limit_lowd0.out	-0.523	ne_5.splups in CHIANTI 10
			limit_lowdm6.out	-0.522	
			nlr_paris.out	-0.411	
Mg IV	4.48711 μ	1-2	pn_fluc.out	-0.167	mg_4.splups in CHIANTI 8
			pn_ots.out	-0.194	
			pn_paris.out	-0.167	
			nlr_paris_cpre.out	-0.192	
			nlr_paris_fast.out	-0.191	

Table 4.3: A list of the spectral transitions that differ in log luminosity due to collisional data changes between Ch7 and Ch10, as calculated by time-dependent test simulations in CLOUDY.

Ion	Wavelength	Transition	Time-Dependent Simulations	Relative Log Lu- minosity Change	Source of Change
Fe12	2405.68 A	1-2	time_cool_cd.out	0.367	fe_12.splups in CHIANTI 10
			time_cool_cd_eq.out	0.367	
Fe12	2169.08 A	1-3	time_cool_cd.out	0.214	fe_12.splups in CHIANTI 10
			time_cool_cd_eq.out	0.214	
Fe12	1349.40 A	1-4	time_cool_cd.out	0.431	fe_12.splups in CHIANTI 10
			time_cool_cd_eq.out	0.432	
Fe12	1242.01 A	1-5	time_cool_cd.out	0.427	fe_12.splups in CHIANTI 10
			time_cool_cd_eq.out	0.428	
Fe13	1.07462 μ	1-2	time_cool_cd.out	-0.223	fe_13.splups in CHIANTI 9
			time_cool_cd_eq.out	-0.223	
Fe13	1.07978 μ	2-3	time_cool_cd.out	-0.315	fe_13.splups in CHIANTI 8
			time_cool_cd_eq.out	-0.316	
Fe14	5303.00 A	1-2	time_cool_cd.out	-0.281	
			time_cool_cd_eq.out	-0.281	

4.3.1 Time-Steady Model Simulations

The results of multiple simulations revealed changes to the line intensities of [O IV] $\lambda 25.8863 \mu\text{m}$, [Ne V] $\lambda 24.3109 \mu\text{m}$, [Ne V] $\lambda 14.3178 \mu\text{m}$, and [Mg IV] $\lambda 4.48711 \mu\text{m}$. The simulations with the prefix ‘pn’ model a planetary nebula, and those with the prefix ‘nlr’ model the narrow line region of an AGN. The planetary nebula model is ionized by a very hot central object, resulting in a large He II abundance. This model, a benchmark for the Paris meeting on photoionization models (198, 1986), is important for assessing the photoionization calculations performed by CLOUDY.

The variations involving electron transitions in O IV, Ne V, and Mg IV are all a result of the updated collision strength data affecting the line intensities:

- O IV: According to the review of CHIANTI 8 in Del Zanna et al. (2015), the collisional data from Liang et al. (2012) replaced those of Aggarwal and Keenan (2008).
- Ne V: According to the review of the Ch10 database in Ch10, a new model used to obtain 304 bound levels replaced a model using R-matrix calculations with only 49 levels.
- Mg IV: According to the review of CHIANTI 8 in Del Zanna et al. (2015), the previous CHIANTI versions contained limited data for this ion due to a lack of accuracy in the data.

As seen in Figures 4.4 and 4.5 changes to O IV, Ne V, and Mg IV collisional data affect the emissivity in these lines. Emissivity (j_ν) is a function of the density of ionized atoms ($n_i(X^{(r)})$ in state i , the kinetic temperature of the gas, and the transition probabilities (A_{ij}),

$$j_\nu = \frac{h\nu_{ij}n_i(X^{(r)})A_{ij}}{4\pi}, \quad (4.2)$$

where ν_{ij} is the frequency at the line center (Spitzer, 1978). Since there is little to no change in the transition probabilities of these transitions between the two databases, the culprit is the population of the upper levels. The excitation rate coefficient is directly proportional to $\Upsilon_{ij}(T)$ and inversely to the square root of the temperature BT,

$$q(j \rightarrow i) = 2\pi^{1/2}a_0\hbar m_e^{-1} \left(\frac{I_\infty}{kT}\right)^{1/2} \frac{\Upsilon_{ij}}{\omega_j} \quad (4.3)$$

where T is the plasma temperature, ω_j is the statistical weight of level j , a_0 is the Bohr radius, m_e is the electron mass, and I_∞ is the Rydberg constant in eV. It is also directly proportional to the deexcitation rate coefficient since one is derived from the other,

$$q(i \rightarrow j) = \left(\frac{\omega_j}{\omega_i}\right) \exp\left(-\frac{E_{ij}}{kT}\right) q(j \rightarrow i), \quad (4.4)$$

where E_{ij} is the transition energy. Naturally, changes to the collision strengths affect both the rate of excitations and deexcitations. The bottom-most panels of Figure 4.4 show that the difference in temperature profiles between the two databases is very

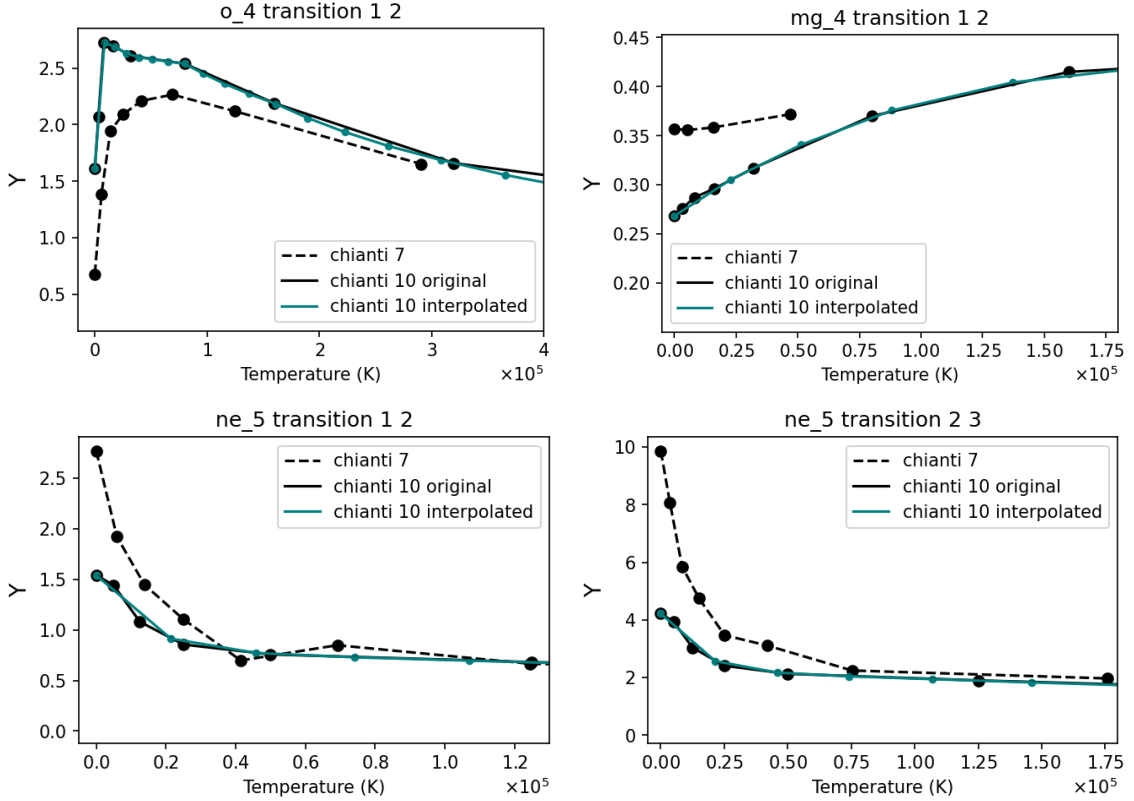


Figure 4.4: Collision strength–temperature profiles in BT space for the botched transitions in the `pn_paris` and `nlr_paris` test simulations.

minimal and only at shallow depths of the cloud. Hence the population of the upper level is affected by variations in Υ_{ij} , and also by changes to the collision strengths of other transitions in that ion to varying degrees.

4.3.2 Time-Dependent Model Simulations

Two time-dependent simulations reveal changes to the luminosities of spectral lines of Fe XII, Fe XIII, and Fe IV. These model time-dependent cooling of a cloud with constant density and are set to predict the time-integrated cumulative energy calculated using the mass. The simulation with the suffix ‘eq’ models only equilibrium cooling (Chatzikos et al., 2015).

These luminosity variations involve transitions in Fe XII, Fe XIII, and Fe XIV are all a result of a cumulative effect on the cooling mechanisms of the plasma (these variations are pertinent to studies involving effects of altering the cooling mechanisms in photoionization models, such as that presented in Gunasekera et al. (2023a)). This is a result of the changes to the collisional data in the Fe XII transitions (collision strength changes shown in Figure 4.6):

- Fe XII: According to the review of the CHIANTI 8 database in Del Zanna et al. (2015), collisional data are obtained from the UK APAP network which

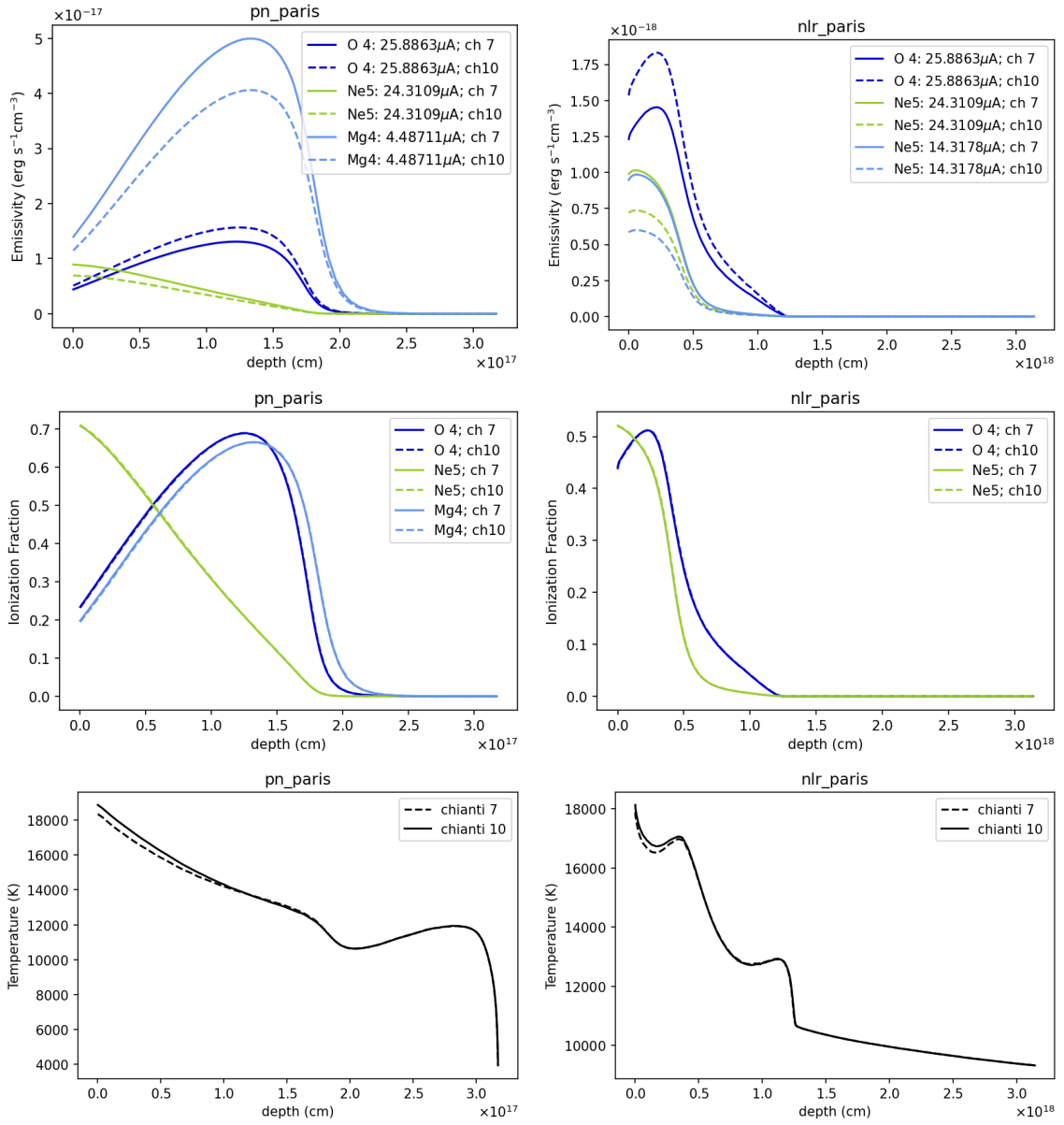


Figure 4.5: CLOUDY outputs of the `pn_paris` and `nlr_paris` test simulations.

includes large R-matrix calculations of 912 levels, replacing the previous R-matrix calculations of only 143 levels.

- Fe XIII: According to the review of the CHIANTI 8 database in Del Zanna et al. (2015), similar to Fe XII, atomic data from a larger R-matrix calculation (749 levels) replaced a smaller one (114 levels).
- Fe XIV: Collisional data for this ion have not changed since Ch7.

The temperature of the plasma and the cooling efficiency in the test simulation that contained the variations to the log luminosities are presented in Figure 4.7. CLOUDY outputs the total cooling as a function of temperature ($L(T)$), which has only a factor of difference from the cooling efficiency ($\Lambda(T)$),

$$\Lambda(T) = \frac{L(T)}{n_e n_p}, \quad (4.5)$$

where n_e and n_p are the electron and proton densities, respectively. We find that at $\sim 10^7$ K the cooling efficiency diverges between the simulations using the Ch7 and the NOAI databases. This results in a divergence in the temperature calculated using these two databases. We also see in Figure 4.7 that at temperatures following the divergence, Fe XII, Fe XIII, and Fe XIV become the dominant coolants (Gnat and Ferland, 2012). Furthermore, for a gas cooling freely at a rate of \dot{M} , the total luminosity in the line is

$$L_\nu = \dot{M} \Gamma(T_{\max}), \quad (4.6)$$

where,

$$\Gamma(T, T_{\max}) = \frac{3}{2} \frac{k_B}{\mu m_p} \int_T^{T_{\max}} \frac{\Lambda_\nu(T')}{\Lambda(T')} dT'. \quad (4.7)$$

is the total emission per unit mass in the line (e.g., Chatzikos et al. (2015)). The other symbols in Equation (4.7) are,

- \dot{M} mass deposition rate;
- k_B Boltzmann constant;
- μ mean molecular weight;
- m_p proton mass;
- $\Lambda_\nu(T)$ frequency-integrated line cooling.

Since the luminosity of the line is a function of the cooling efficiency and temperature, the luminosity of the lines in the above electron transitions has changed as a result of changes to the collision strength data.

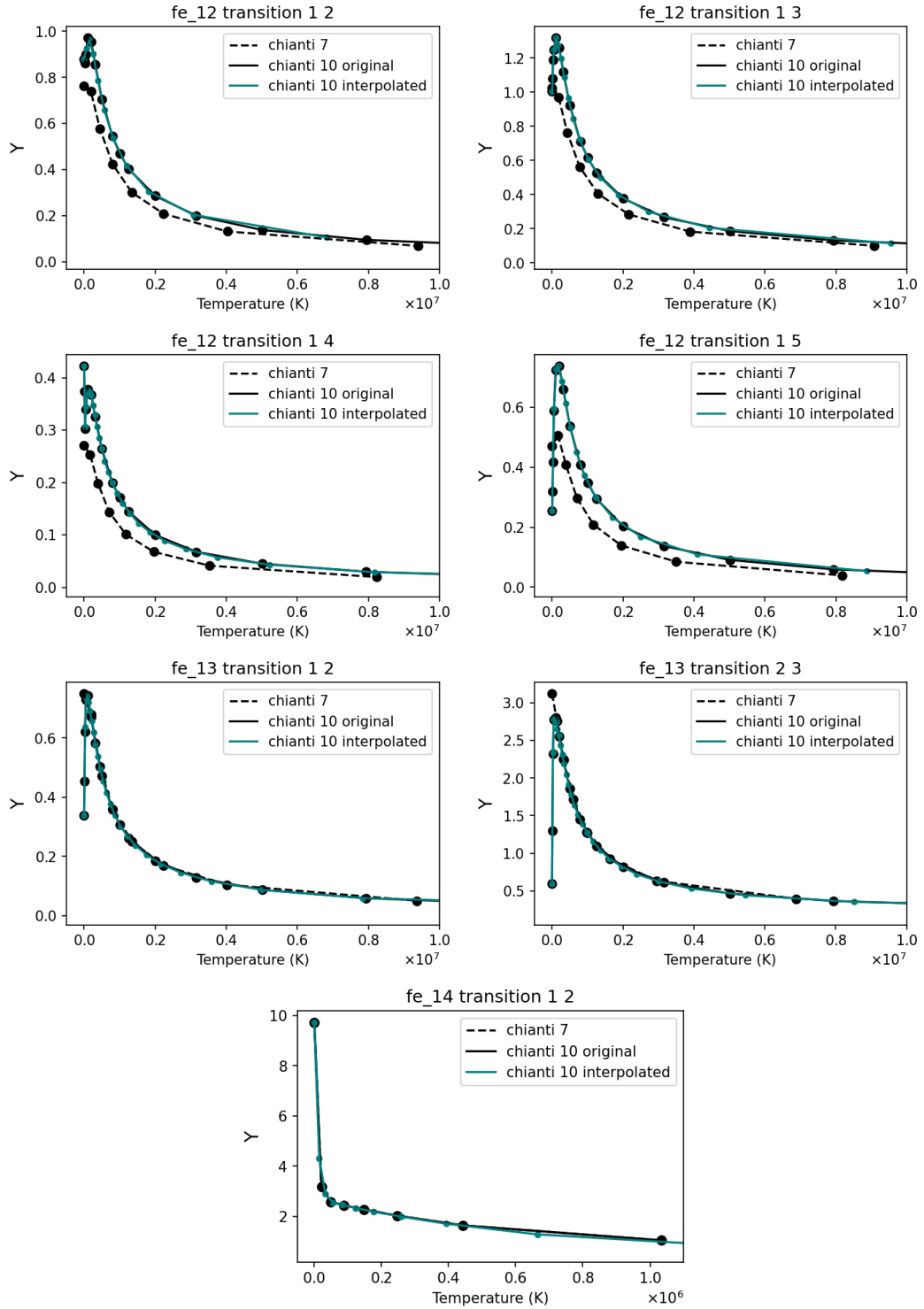


Figure 4.6: Collision strength against temperature in BT space for botched Fe XII, Fe XIII, and Fe XIV electron transitions in the `time_cool_cd` test simulation. Green plot lines indicate equally spaced temperature grid data interpolated from the original source of the Ch10 data. The original data show all but the last data point, which corresponds to the point at the high-temperature limit.

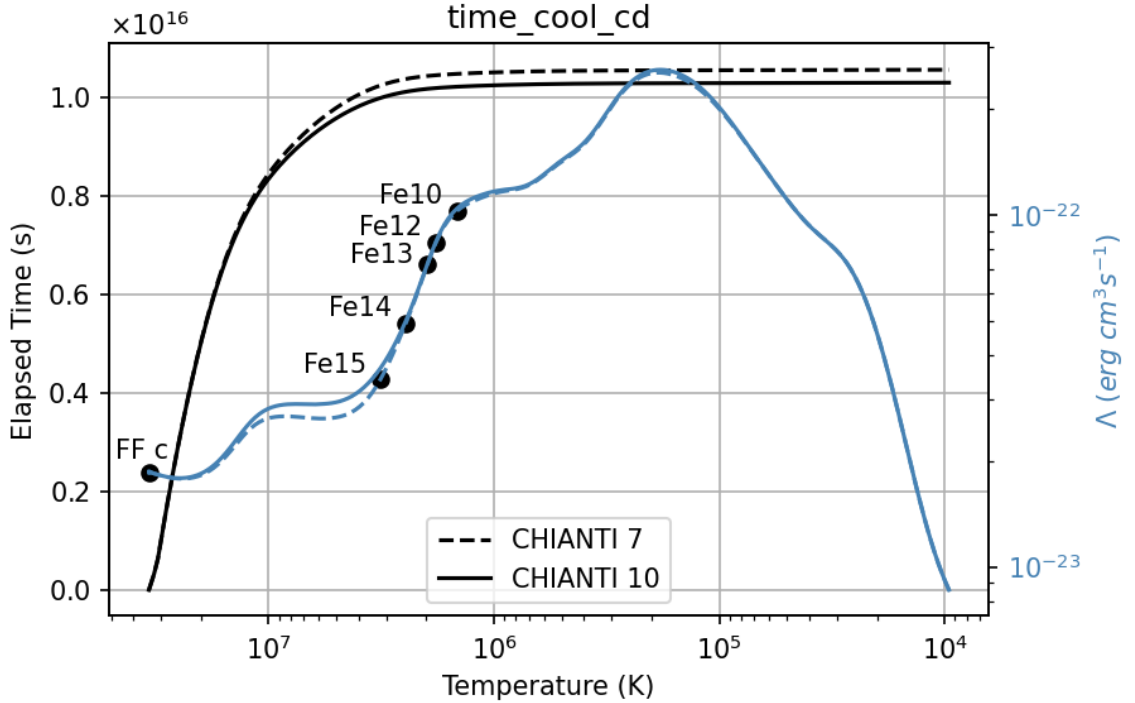


Figure 4.7: Temperature as a function of time (in black), and total cooling as a function of temperature (in blue). Dashed lines indicate the output of the simulation utilizing atomic data from the Ch7 database, and solid lines indicate the output of the simulation utilizing the reprocessed Ch10 database. The black circles indicate the dominant coolant at that temperature and the following temperatures up to the next black circle. Free-free cooling is denominated by ‘FFc’.

4.4 Summary

In adopting the newest version of CHIANTI, we developed a script that will reprocess the Ch10 data to the format of the version currently used by CLOUDY-Ch7. This allows us to use Ch10 data in the CLOUDY calculations, without changing CLOUDY. As future versions of CHIANTI become available, we will be able to account for format changes when adopting to CLOUDY with only minor modifications to our external script.

The `.elvlc` and `.wgfa` files in Ch10 require only minor changes to the spacing between the data and a re-organization of the columns to be converted into the Ch7 format. In contrast, the `.scups` to `.splups` file format conversion required an interpolation of Ch10 collision strength data due to its irregularly spaced temperature grids. Finally, to reduce the size of our atomic database, we omitted all autoionizing levels. This was done since the Ch10 database includes many levels above the ionization limit which are currently not used by CLOUDY. Statistical analyses showed that the resulting truncated and reprocessed database is sufficiently small and accurate enough to be used in the microphysical calculations in CLOUDY.

Changing the collision strength data from Ch7 to Ch10 produced variations in

the intensity of 10 different spectral lines predicted by CLOUDY. Three of these ten line variations were observed in six different time-steady test simulations (modeling planetary nebulae, and narrow-line AGNs). The impact of the change in collision strength data (of O IV, Ne V, and Mg IV) on the upper-level populations of the transitions resulted in significant changes to the line intensities of [O IV] $\lambda 25.8863 \mu$, [Ne V] $\lambda 24.3109 \mu$, [Ne V] $\lambda 14.3178 m$, and [Mg IV] $\lambda 4.48711 \mu A$. The remaining seven line variations were observed in time-dependent test simulations of a cooling isochoric plasma. The impact of the change in collision strength data on the cooling efficiency of the plasma resulted in significant changes to the line luminosities of [Fe XII] $\lambda 2406$, [Fe XII] $\lambda 2169$, [Fe XII] $\lambda 1349$, [Fe XII] $\lambda 1242$, [Fe XIII] $\lambda 1.07462 \mu$, [Fe XIII] $\lambda 1.07978 \mu$, and [Fe XIII] $\lambda 5303$.

Chapter 5 A $\sqrt{\pi}$ Error in Ly α Optical Depth Normalization

5.1 Introduction

I present the C23.01 update to CLOUDY, succeeding C23.00 (Ferland et al., 1998, 2013, 2017; Chatzikos et al., 2023). I correct an error in our use of the Hummer and Kunasz (1980) theory of Ly α destruction that dates back to \sim 1990. The Ly α intensity can change by as much as 0.5 dex for highly ionized dusty clouds.

5.2 Line transfer in dusty media

Resonance lines of abundant atoms often have large optical depths, so the effects of scattering and absorption must be taken into account. Line photons can be lost by either collisional deexcitation, where the photon’s energy is converted into thermal energy, or by absorption by background opacities, where the photon is absorbed by photoelectric or grain opacity (Mihalas, 1970; Elitzur, 1992; Rutten, 2003; Hubeny and Mihalas, 2014).

The escape probability formalization is a powerful treatment of the effects of radiative trapping (Netzer et al., 1985; Elitzur, 1992; Osterbrock and Ferland, 2006). This replaces the net radiative bracket in the radiative transfer equation with the product of the transition rate and the probability that a photon will escape in a single scattering, $\beta_{\text{esc}A_{ul}}$ (Netzer et al., 1985; Elitzur, 1992). Here β_{esc} is the escape probability for a transition with upper and lower levels u, l .

The line profile function $\varphi(x)$ lies at the heart of line transfer physics. Radiative trapping and escape compete with photon destruction through continuous absorption processes, the so-called “background opacity”. The Voigt line profile,

$$H(a, x) = \frac{a}{\pi} \int \frac{dt e^{-t^2}}{(x-t)^2 + a^2},$$

describes how matter absorbs photons, while the redistribution function describes the relation between absorption and subsequent emission. Here, x is the frequency displacement from line-center, and a is the Voigt parameter (Hjerting, 1938; Hummer and Kunasz, 1980).

There are two normalizations of the optical depth, line-center and mean. Optical and ultraviolet spectroscopy conventionally use line-center optical depths (Mihalas, 1970; Rutten, 2003). Mean optical depths are more convenient for very large values of the damping constant, as is typical of allowed lines of high-ionization species in the X-ray regime (Hummer and Kunasz, 1980). For small a , the mean optical depth is a factor of $\sqrt{\pi}$ times larger than the line-center optical depth.

CLOUDY internally works with line-center optical depths throughout. When the code expanded to higher energies, mean optical depths became more useful, and mean optical depths are now reported. CLOUDY treats line overlap and integrates the line optical depth through a medium where the Doppler width will generally be varying,

so it is not straightforward to convert the line-center optical depths used internally to a mean optical depth. To avoid these difficulties, we report a mean optical depth that is exactly a factor $\sqrt{\pi}$ times *larger* than the line-center optical depth. This assumes that the Voigt function at line-center is $H(0, a) \approx 1$. This approximation is valid when the damping parameter a is small, $a \ll 1$ which is generally the case in the IR, optical, and UV wavelength range. This conversion is more approximate in the X-ray regime where a can be much larger.

CLOUDY uses fits to the escape β_{esc} and destruction β_{des} probabilities presented in Hummer and Kunasz (1980, hereafter HK80) for H I Ly α . This theory uses mean optical depths τ , and considers a wide variation in the values of a . The original incorporation of the HK80 theory into CLOUDY, dating back to at least the C80 (circa ~ 1990) release, required a conversion from τ to τ_0 within one routine. We found that this conversion had an erroneous factor of π in the calculation of β_{HK} , a parameter in the HK80 theory. This affected the loss of H I Ly α photons due to “background” opacity, with dust being the dominant opacity absorbing Ly α .

In the following sections, we derive the new calculation of β_{HK} , discuss changes in the simulated spectra, and detail how the C23.01 release can be downloaded.

5.3 Lyman α Escape & Destruction Probability

The starting point of the HK80 theory is the β_{HK} parameter, defined as (Eq. 2.7 of HK80):

$$\beta_{\text{HK}} \equiv k_{\text{c}}/k_{\text{L}}, \quad (5.1)$$

where k_{c} is the continuum opacity of background destruction processes (such as absorption on dust grains), and k_{L} is the line opacity. CLOUDY uses a slightly different definition for β_{HK} that is better behaved in extreme conditions (like hydrogen-deficient and very dust-rich gas, see e.g., Borkowski and Harrington, 1991):

$$\beta_{\text{HK}} \equiv k_{\text{c}}/(k_{\text{L}} + k_{\text{c}}). \quad (5.2)$$

For the range of conditions considered by HK80 ($k_{\text{c}} \ll k_{\text{L}}$), there is very little difference between the two definitions. The opacity of the line is defined as (Eq. 2.3 of HK80):

$$k_{\text{L}} = \frac{N_l B_{lu} h \nu_0}{4\pi \Delta}. \quad (5.3)$$

Here N_l is the lower-level population, B_{lu} is the Einstein-B coefficient for absorption, h is the Planck constant, ν_0 is the central frequency of the line, and Δ is the Doppler width of the line. The Einstein-B coefficient is related to the oscillator strength f_{lu} as follows (Rybicki and Lightman, 1979):

$$B_{lu} = \frac{4\pi^2 e^2}{m_e c h \nu_0} f_{lu}. \quad (5.4)$$

Here e is the elementary charge in electrostatic units, m_e is the mass of the electron, and c is the speed of light. The Doppler width is converted to velocity units Δ_v as

follows:

$$\Delta = \frac{\Delta_v}{c} \nu_0 = \Delta_v \sigma_0, \quad (5.5)$$

where σ_0 is the wavenumber of the line, $\sigma_0 = \nu_0/c$. Substituting Eqs. 5.4 and 5.5 into Eq. 5.3 yields:

$$k_L = N_l \frac{\pi e^2}{m_e c \Delta_v \sigma_0} f_{lu}. \quad (5.6)$$

The opacity constant of the line κ_L is defined in CLOUDY as:

$$\kappa_L = \frac{\sqrt{\pi} e^2}{m_e c} f_{lu} \frac{1}{\sigma_0}. \quad (5.7)$$

Substituting Eq. 5.7 into Eq. 5.6 yields:

$$k_L = N_l \kappa_L \sqrt{\pi} / \Delta_v. \quad (5.8)$$

In the previous CLOUDY code, β_{HK} was calculated using the k_L derived in Equation 5.8 divided by π .

5.4 Changes to Spectra

With this change, k_L is now larger by a factor of π , decreasing β_{HK} by approximately the same factor (assuming $k_c \ll k_L$). Thus, the destruction probability by background opacities is now reduced by approximately the same factor of π .

CLOUDY includes a large test suite which makes autonomous testing possible. These showed that the largest changes occurred for dusty clouds where H Ly α destruction is important. Figure 5.1 shows the H Ly α intensity for a blister H II region model inspired by the Orion H II region, a hydrostatic ionized layer on the surface of a molecular cloud (?). We consider a range of hydrogen densities ($10 \leq n(\text{H}) \leq 10^6 \text{ cm}^{-3}$) and stellar ionizing photon fluxes ($10^{11} \leq \phi(\text{H}) \leq 10^{14} \text{ photons cm}^{-2} \text{ s}^{-1}$). The Figure shows predictions of C23.01 relative to those of C23.00.

Our new calculations have reduced the destruction probability so H Ly α is now stronger. The biggest change occurs at high $\phi(H)$ and low $n(H)$, corresponding to high ionization parameters ($U = \phi(H)/cn(H)$). As we increase U and the ionization, grains proportionately absorb more of the ionizing photons (Bottorff et al., 1998; ?). More highly ionized clouds have less atomic opacity but the same grain opacity, so there is a greater probability of a photon being absorbed by grains rather than scattered from a hydrogen atom. The destruction probability of H Ly α is higher at high U . Reducing the destruction probability by a factor of π results in the greatest enhancement of H Ly α in the lower right corner.

5.5 Summary

The primary result of this update are changes to the H Ly α line in dusty environments at moderate to high ionization parameter. We present an update to CLOUDY, which includes changes in the hydrogen Lyman α escape and destruction probabilities based

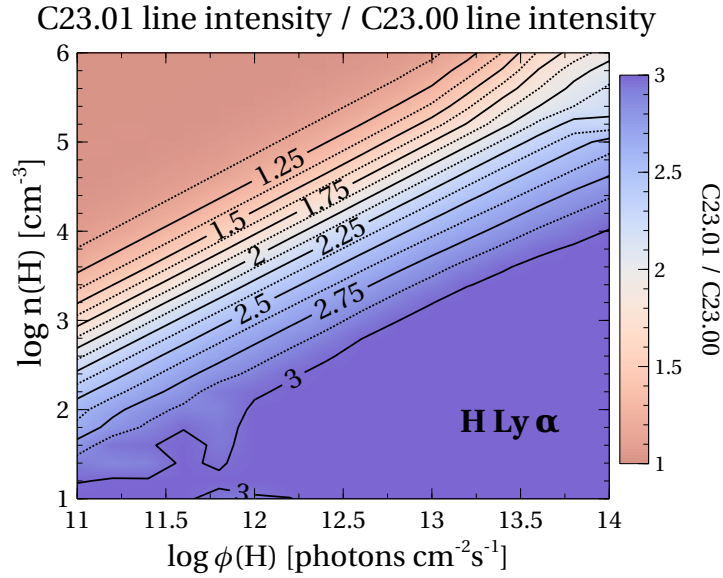


Figure 5.1: A contour plot of H Ly α line intensity predicted by C23.01 relative to the same quantity from C23.00, for the baseline model `orion_hii_open.in` in the CLOUDY test suite. The ratio of ionizing photon flux $\phi(H)$ to hydrogen density $n(H)$ is effectively the ionization parameter U . The lower-right corner of the panels corresponds to high U , and the upper-left corner is low U .

on HK80. Since H Ly α is often the strongest line in the spectrum, significant changes in its physics will have consequences on other physical parameters. A discussion of the changes to the grain emission and other consequences will be presented in the C24 release paper.

This update has been released as C23.01 and is now available to download from wiki.nublado.org. Papers that use this version of CLOUDY should cite both Chatzikos et al. (2023) and Gunasekera et al. (2023b).

Chapter 6 Resolving One-electron fine-structure Lyman lines: Preparing Cloudy for high-resolution X-ray in the microcalorimeter era.

6.1 Introduction

There are a multitude of astrophysical objects that emit X-rays from galaxy clusters to supernova remnants to X-ray binaries and many more. X-ray astronomy has developed into an extensive field of research, and has made significant strides in understanding the hot and energetic Universe. X-ray emissions are mainly produced in cosmic hot plasmas at temperatures from 10^6 to 10^8 K, with energies ranging from 0.1 to 10 keV.

At such high energies, the energy spectral resolution is of consequential importance to observational X-ray studies. The first mission dedicated to X-ray observations was by the *Uhuru* satellite operated by NASA. It was launched in 1970 with a spectral resolution $R = E/\Delta E \sim 10$, using proportional counters (Kellogg et al., 1971; Giacconi et al., 1971). In the 1990s, the HRI camera onboard *ROSAT* using a crossed grid detector observed EUV 62 – 206 eV at 0.1 – 2.5 keV (Frontera et al., 1998). By 1999, *Chandra X-ray Observatory* and *XMM-Newton* whose grating spectrometers observe at $R \sim 60 - 1000$ at 0.4 – 8 keV and $R \sim 300$ from 0.4 – 2.5 keV, respectively (Canizares et al., 2005). Finally, the next generation of X-ray observers using microcalorimeter technology, such as XRISM, have energy resolutions of $R > 1000$. Each advancement in spectral resolution has led to new discoveries in the X-ray Universe.

CLOUDY conducts simulations of non-equilibrium plasmas and predicts X-ray line intensities. The original framework was designed for only one- and two-electron species and used scaling relations along the iso-electronic sequences (Ferland et al., 2013). Priyanka Chakraborty extended the CLOUDY framework on line formation processes for one- and two-electron species that improved upon the accuracy of level energies and line wavelengths to meet the spectral resolution X-ray microcalorimeter missions (Chakraborty et al., 2022, 2021, 2020b,a). However, CLOUDY remains to use and report single energies for the nP level electrons for both iso-sequences.

The 2P shell of H-like ions is split into two fine-structure levels (with $j = 1/2, 3/2$) by the spin-orbit interaction between an atomic nucleus and the atomic electron. Hence, emission lines from the H iso-electronic sequence in astrophysical plasmas with energy spectral resolutions of $E/\Delta E > 1000$ will resolve two energy peaks instead of one.

6.2 One-electron Doublets in Cloudy

Cloudy has long treated one and two-electron systems with great care for several reasons. The first is due to the large abundance of hydrogen and helium which, together, make up 99.9% of the atoms in the universe. The second distinction is that the energy-level structures of one and two-electron systems are quite different from the complex energy structure that is found in many-electron systems like, for instance,

O II and O III. As shown in figure 3 of Ferland et al. (2013), the first excited state of one and two electron systems is roughly 3/4 of the ionization potential and most of the states are very close to the continuum above. These highly-excited levels, called the Rydberg states in atomic physics, mediate the recombination process, so affect the ionization. Hydrogen and helium, in particular, must be treated with great care because they determine the ionization structure of a cloud and their recombination lines are important in determining the composition and ionization of clouds across the universe.

The Rydberg levels pose several interesting problems. An infinite number of them are in the low-density limit, although the number of levels is truncated at finite densities (Alimohamadi and Ferland, 2022). We must sum over all the levels to obtain the total recombination coefficient to predict the ionization correctly. The higher levels collisionally couple to the continuum to bring the atom’s ionization into LTE or STE at high particle or photon densities, so, again, many levels must be included. Many strong optical and infrared lines have upper levels in the Rydberg states, so we must determine their level populations with some precision to predict the spectrum. The fundamental problem is to treat a very large number of levels with the available computer hardware.

Our treatment of the Rydberg levels has changed as computers have become faster. Initially, we used several pseudo-states to represent the closely-spaced Rydberg levels at high principal quantum numbers (Cota, 1987; Ferguson and Ferland, 1997). The pseudo-states allowed the atom to go to LTE and STE limits when the particle or photon densities were sufficiently high (Ferland and Rees, 1988; Ferland and Persson, 1989). A disadvantage to this approach was that the pseudo-states affected the accuracy of the H and He recombination-line intensities. This approach reproduced classical Case B Osterbrock and Ferland (2006) intensities of H and He recombination lines to better than five percent.

Recombination lines must be predicted to high precision for certain applications, such as the Primordial Helium abundance, (Ferland et al., 2010) or for denser environments, where collisional and radiative transfer effects may be important (Ferland, 1999). Classical case B productions do not describe such clouds so detailed radiative transfer must be done simultaneously with the solution of the emission and ionization.

As computers became faster, it became possible to remove the pseudo-states and replace them with models of higher- n shells. This advance was described in a series of papers that focused on measurements of the primordial helium abundance (Bauman et al., 2005; Porter et al., 2005, 2007, 2009, 2012). Ferland et al. (2013) summarises this development. Figure 1 of that paper shows our model for one-electron systems. We use nl -resolved states for low principal quantum numbers. “Collapsed states”, which are not l -resolved, were used for high n where collisions should bring the nl populations into $g = 2l + 1$ statistical equilibrium.

Pseudo-states are not used to describe the recombination and line-producing physics in our final approach. We use a finite number of collapsed and resolved levels with a small amount of “top off” recombination coefficient being added to the highest level to reproduce the total recombination to all levels.

This approach had a problem near photoionization edges such as the Lyman jump.

This is shown in figures 7 and 8 of Ferland et al. (2017). In nature, the very high n Lyman lines merge onto the Lyman continuum above the bound levels, and no discontinuous Lyman jump is present. A finite model produces gaps in the spectrum where unmodelled high- n Lyman lines should add opacity. The continuum can “leak” through the cloud, as shown in Figure 8 of that paper. We dealt with this by adding many “extra” Lyman lines. These added opacity to the cloud but, in the original treatment, did not produce emission.

As outlined above, the original treatment of one-electron systems focused on light species such as H I or He II. As described in the Introduction, high-resolution X-ray spectroscopy will soon become commonplace. The Lyman lines in one-electron systems are doublets. Figure 6.1 below shows that the doublet separation is small for light elements, such as hydrogen and helium, and would not be resolvable for typical astrophysical temperatures ($\sim 10^4$ K). The development so far resolved nl but not j . Figure 6.1 shows that the doublet separation also increases as the nuclear charge Z increases. Future X-ray missions will resolve the Lyman series doublets for elements heavier than silicon. The doublet separation depends on n . It is largest for the 2-1 transition and decreases as n increases. Future X-ray missions will resolve lower- n transitions of higher- Z species.

This investigation further develops the extra Lyman lines described in Ferland et al. (2017) to predict doublet emission. C17 considered absorption by these “extra” Lyman lines for all one and two-electron systems. We use the existing level and ionization population solvers, which are not j resolved, to determine the populations of upper np_j levels and include the emission that results. We should produce synthetic spectra of the *Hitomi* Perseus cluster spectrum.

6.2.1 Radiative transfer

We know the individual opacities and optical depths for the j -resolved lines and need to get this information into the solver self-consistently.

$$n_{2p}A_{21}\beta_{net} = \sum_j n_{2pj}A_{2pj}\beta_j \quad (6.1)$$

where β is the escape probability.

6.3 Energy Calculations

6.3.1 Fine-Structure Splitting

Consider a single electron orbiting an atomic nucleus of Z . An accelerating charge sets up a magnetic field. So magnetic field caused by the positive nucleus exerts a torque on the magnetic moment of the electron in the direction of aligning it along the field. Hence the general Hamiltonian of the electron in the magnetic field of the nucleus is,

$$H = \mu_e \cdot \mathbf{B}_N. \quad (6.2)$$

The magnetic field of the nucleus is related to the orbital angular momentum of the electron. In the rest frame of electron, the magnetic field can be approximated by a current loop. The current then is given by $I = Ze/T$, where T is the period of the orbit. Since this is the same orbital period of the electron which relates to its orbital angular momentum, $\mathbf{B}_N \propto \mathbf{L}_e$.

The magnetic dipole moment of a spinning charge is related to its spin angular momentum. So we have that $\mu_e = -\frac{e}{m}\mathbf{S}_e$.

Hence $H \propto \mathbf{S}\cdot\mathbf{L}$, which is the spin-orbit interaction. The eigenvalues of this term are given by $j(j+1) - l(l+1) + s(s+1)$. For an electron we have that $s = 1/2$ so there is no s dependence. Additionally, the relativistic correction cancels out the orbital angular momentum quantum numbers, leaving only a dependence on the quantum number j . The total energy levels of these atoms with the fine structure included are,

$$E_n^0 + E_{nj}^{FS} = m_e c^2 \left[1 + \left(\frac{\alpha Z}{n - k + \sqrt{k^2 - \alpha^2 Z^2}} \right)^2 \right]^{-\frac{1}{2}} - m_e c^2 \quad (6.3)$$

where, $j \in \{|1/2 - l|, \dots, (1/2 + l)\}$, $k = j + 1/2$, n is the principal quantum number, α is the fine structure constant and m_e is the mass of the electron. This interaction can be thought of as a perturbation, and so it partially lifts the degeneracy of the energy states by splitting the levels with different l .

For the H iso-electronic sequence, since $l = 1$ for the 2P states we have a doublet with $j = 1/2, 3/2$.

6.3.2 nP Level Energy Corrections

The total energy for the nP levels in a Hydrogen-like atom is the binding energy of an electron E_{nP} .

$$E_{nP} = E_n^0 + E_{nj}^{FS} + E_{n,l=1,j}^{LS} + E_{nj}^M, \quad (6.4)$$

where E_n^0 is the unperturbed energy,

$$E_n^0 = -\frac{\mu}{m_e} \frac{Z^2 Ry}{n^2}. \quad (6.5)$$

Here $Ry = hcR_\infty$ is the Rydberg unit of energy, and $\mu = m_e m_N / (m_e + m_N)$ is the reduced mass of the electron, where m_N is the nuclear mass. For our calculations, we use the ionizing potentials of the one-electron ion already given within CLOUDY to determine E_n^0 . E_{nj}^{FS} is the fine-structure correction that resolves the levels with different j given in Eq. 6.3.

$E_{n,l>0,j}^{LS}$ is the Lamb Shift correction which resolves the levels with different l ,

$$E_{n,l>0,j}^{LS} = \frac{8Z^4 \alpha^3}{3\pi n^3} Ry \left[\log \frac{Z^2 Ry}{K_0(n, l)} + \frac{3}{8} \frac{c_{lj}}{2l + 1} \right], \quad (6.6)$$

$$c_{lj} = \begin{cases} (l + 1)^{-1}, & j = l + 1/2, \\ -l^{-1}, & j = l - 1/2. \end{cases} \quad (6.7)$$

where, $\log K_0(n, l = 1)/Z^2 Ry$ is the Bethe logarithm calculated using Equation 1. The numerical value of $K_0(n, l = 1)$ is difficult to evaluate for a large number of n , during each run of CLOUDY. So an approximation of the Bethe logarithm used in the present study, and is further discussed in 7. This is sufficient to achieve the accuracy needed for the present purpose.

Lastly, E_{nj}^M is the nuclear mass recoil correction

$$E_{nj}^M = m_e c^2 \frac{m_e}{m_N} \frac{(\alpha Z)^2}{2N^2} - \mu c^2 \left(\frac{m_e}{m_N} \right) \frac{(\alpha Z)^2}{2n^2} \quad (6.8)$$

$$N = \left(\left(n - k + \sqrt{k^2 - \alpha^2 Z^2} \right)^2 + \alpha^2 Z^2 \right)^{1/2} \quad (6.9)$$

where $k = j + 1/2$ as before (Yerokhin and Shabaev, 2015).

6.4 Incorporating into Cloudy

The current CLOUDY infrastructure uses only n-resolved energy levels. To fit the j-resolved fine structure calculations around the already existing n-resolved infrastructure, we will take the following steps. First, we will copy the single array that contains the primary “extra” Lyman lines into two separate $l = 1$ energy level arrays, for $j = 1/2$ and $j = 3/2$. Using the energy level solver, we will then populate the upper levels of this array, with the appropriate population densities. The CLOUDY solver will then be able to evaluate the doublet emission lines from 2P up to $^n P$. The main advantage of this method is the ability to recover line optical depths of the j-sublevels.

By considering the current and near-future instrumental limitations in spectral energy resolution, we need to consider which H-like atoms reasonably require us to resolve the fine-structure energies, and the highest principal quantum number (n) in which the energy differences remain observable. It is also necessary to determine if j-changing collisions are important in the density domain utilized by CLOUDY. The following subsections discuss our analysis and determinations of each of these values.

6.4.1 Energy Resolution & Accuracy

Figure 6.1 shows a contour map of the spectral energy resolution (top panel), and the required resolving power (bottom panel) for fine-structure splitting in the 2P shell of heavy-metals up to Zn ($Z=30$) and n up to 16. The energy difference in the split fine-structure levels become rapidly smaller at higher n levels, but rapidly larger with heavier atomic nuclei.

XRISM has an energy resolution of 5 eV for the energy range 0.3-12 keV, while *Athena* is expected to have a resolution of 2eV. So to meet the upcoming instrumental requirements, according to figure 6.1 we need to resolve the nP shells into doublets for atoms heavier than Phosphorous ($Z=15$) and for $n < 5$. However, we will be using Equations 6.3-6.9 to re-define the energies in CLOUDY, for all the available Z and n .

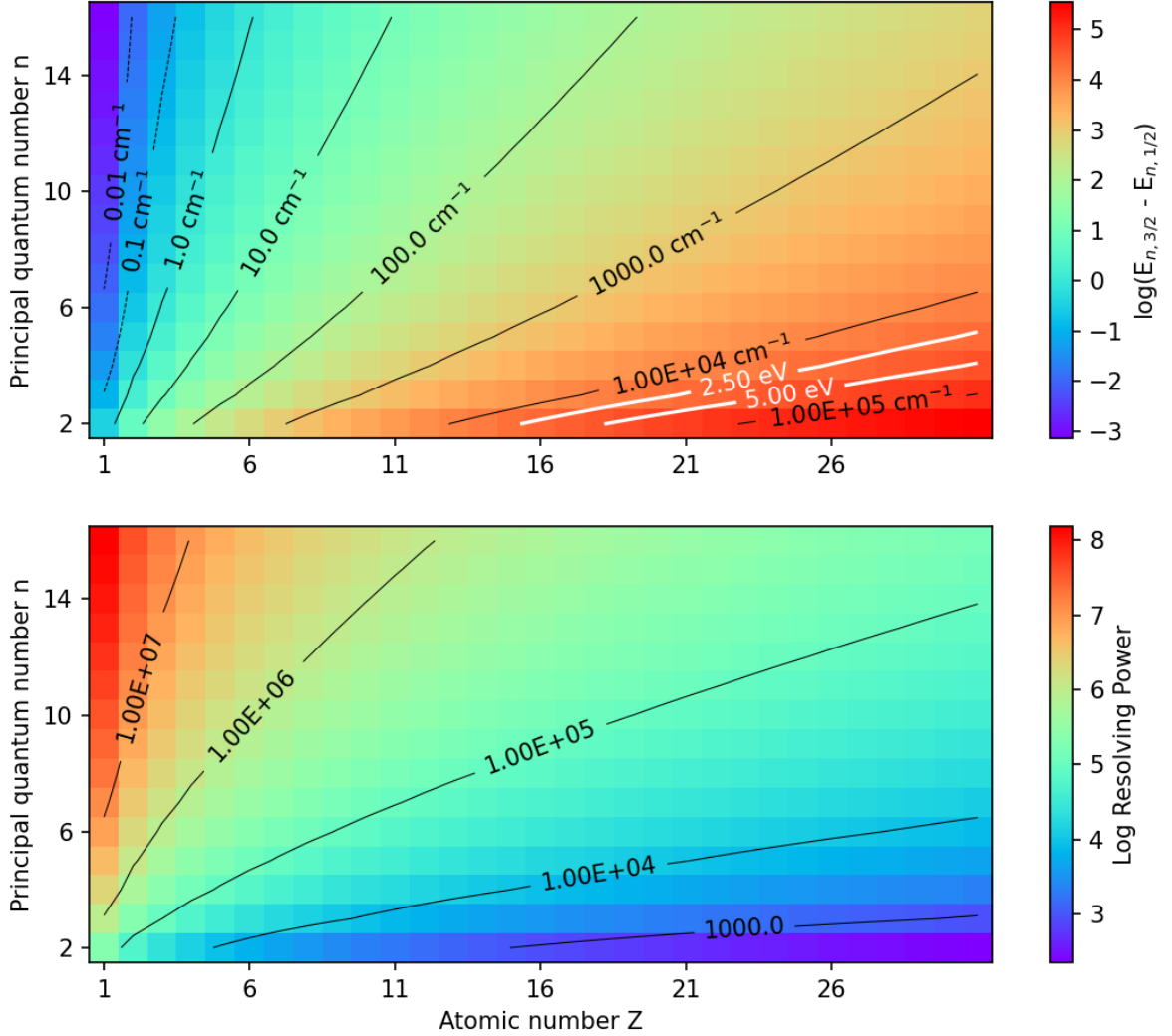


Figure 6.1: *Top*: Contour plot of energy separation between the $nP_{1/2}$ and $nP_{3/2}$ levels. The white plot lines indicate the spectral resolution of the current microcalorimeter mission *XRISM* ($R \sim 5 \text{ eV}$) and future mission *Athena* ($R \sim 2.5 \text{ eV}$). *Bottom*: Contour plot showing the resolving power required to distinguish between the $2S_{1/2}-nP_{1/2}$ and $2S_{1/2}-nP_{3/2}$ transition energies, where $E_{2S_{1/2}} = 0$. For both plots the y-axis is the range of principle quantum numbers used in CLOUDY calculations, and the x-axis is the range of elements with atomic number Z used.

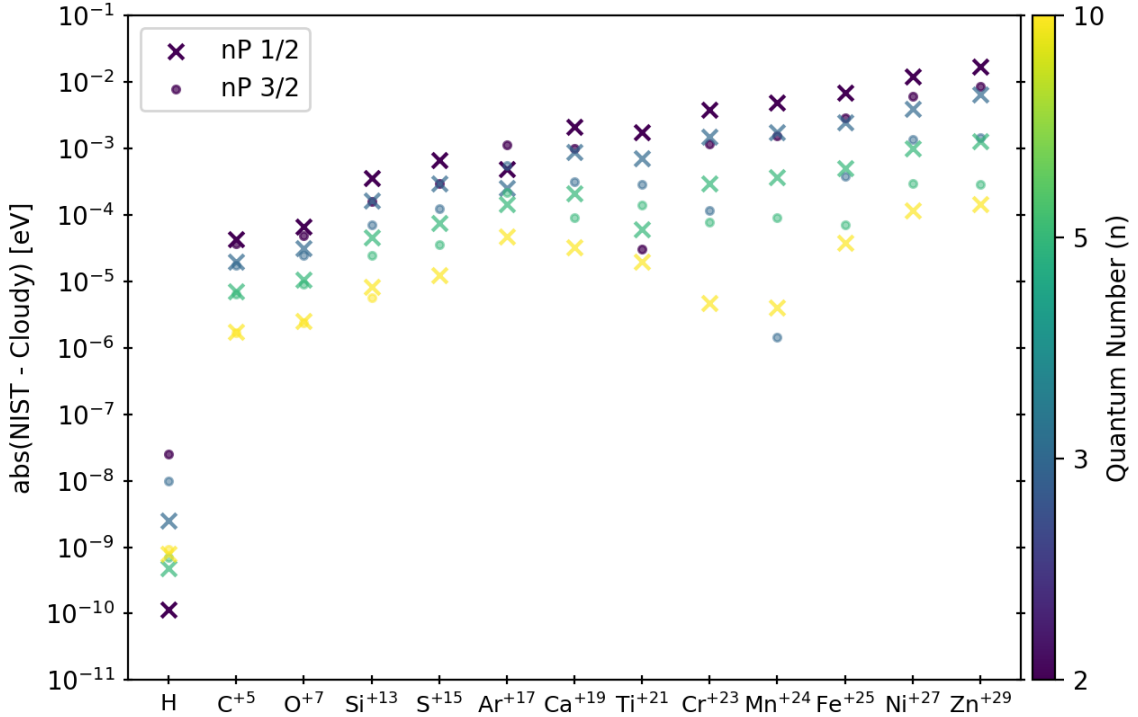


Figure 6.2: Energy scale accuracy of the updated $nP_{1/2}$ and $nP_{3/2}$ levels for H-like species in CLOUDY, using NIST as the authority. The expected accuracy for *XRISM* is 0.5 eV, which is well above those for any of our new H-like nP_j energy calculations. The dots indicate the accuracy for $j = 1/2$, and crosses indicate those for $j = 3/2$. The colors going from purple to green indicate increasing principle quantum number n .

Additionally, *XRISM* is expected to have an energy scale accuracy of 0.5 eV. Figure 6.2 provides the difference between our total level energies and those in NIST, in units of eV for various one-electron atoms. We find that our largest energy error is 0.01 eV, which is a factor of 10 better than *XRISM*'s expected energy accuracy. Thus, fulfilling the energy accuracy and resolution requirements for the up-coming X-ray missions and beyond.

6.4.2 Transition Probabilities

CLOUDY uses the complete non-relativistic calculations to determine transition probabilities (a.k.a Einstein A values) (Drake, 2006). These computations are not j-resolved, since the correction factors evaluate to unity in our simple case. Although, they differ from the NIST Einstein As which include relativistic corrections, by at most ~ 2 per cent (Jitrik and Bunge, 2004), this accuracy is sufficient for our current

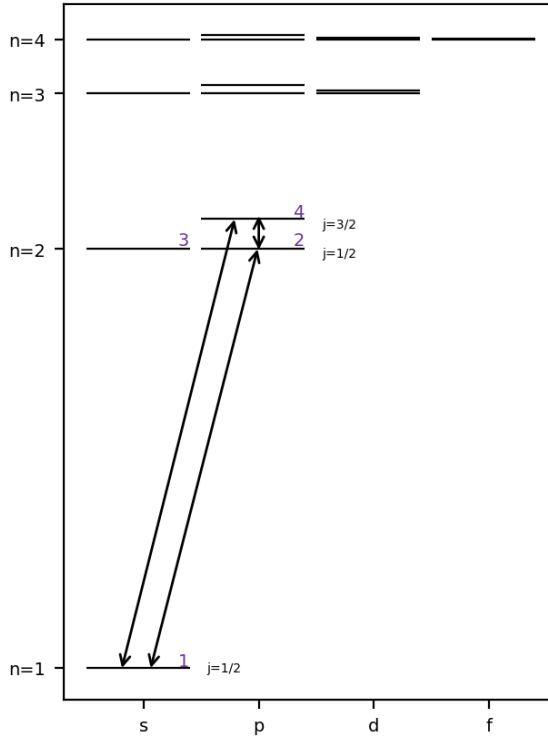


Figure 6.3: Energy level diagram showing the fine-structure levels of angular momentum quantum number $l > 1$. Note, the level ordering is consistent with energy levels of lighter H-like species. For higher- Z 1-electron atomic species, energy of level $2P_{1/2}$ is higher than that of $2P_{3/2}$, although this swap is not predicted in Yerokhin and Shabaev (2015).

instrumental needs. So we leave them as they are for now. Future work will involve including relativistic corrections to the CLOUDY computed transition probabilities.

6.4.3 Doublet Line Intensities

Emission line intensities are determined by the population density of the corresponding upper level u of the transition (n_u), and the probability of spontaneous emission (A_{ul}) of the transition $u \rightarrow l$. So, to determine the nP fine-structure line intensities, we need to first determine the population densities of the $nP_{j=1/2}$ and $nP_{j=3/2}$ levels. Figure 6.3 shows an energy level diagram of a one-electron atom, with the key electron transitions that need to be considered. In concurrence with Figure 6.3, for the remainder of this manuscript, we will denote energy levels $1S_{1/2}$, $2P_{1/2}$, $2S_{1/2}$, and $2P_{3/2}$ simply as levels 1,2,3 and 4 respectively. Here we discuss the prescriptions for $n = 2$ levels for simplicity, however, the same framework is extended for levels $n > 2$.

The presence of fine-structure transitions is determined by the density of the ionized gas (n_{gas}). In steady state, $\frac{dn_u}{dt} = 0$ results in two possible limits based on how the ionized gas density compares with the critical density (n_{crit}),

$$n_{\text{crit}} = A_{ul}/q_{lu}. \quad (6.10)$$

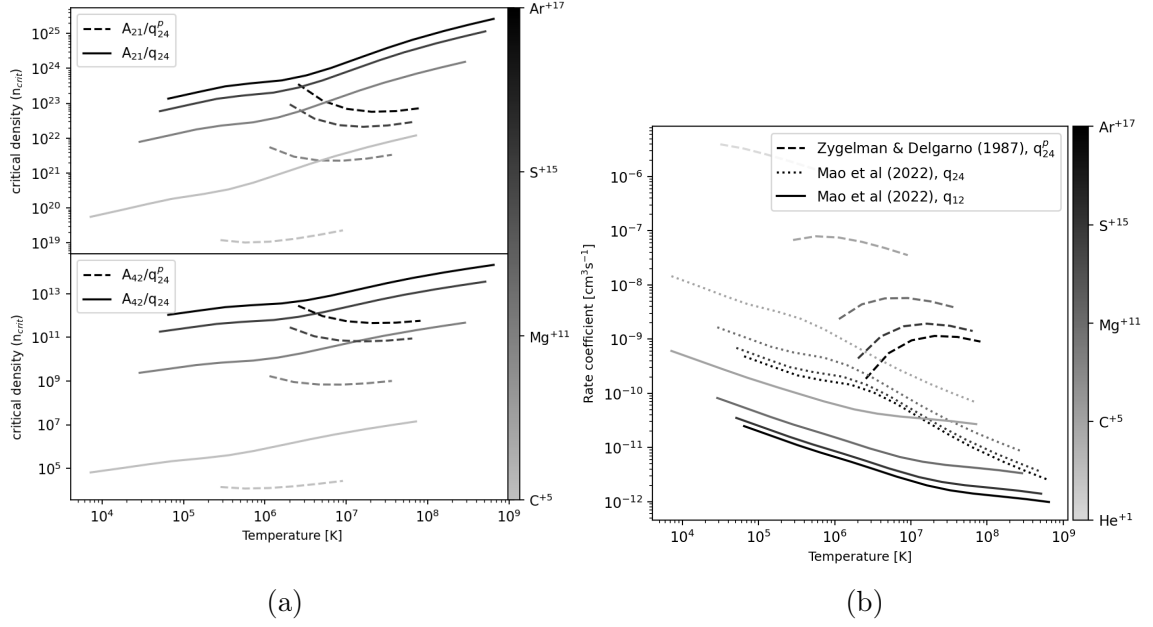


Figure 6.4: (a) The ratio between transition probability (A_{ul}) for the 1S–2P transition to collisional rate coefficients (q_{ul}) for j -changing collisions as a function of temperature for four different H-like ions. *Top panel:* ratio involving Einstein A values for $2Pj = 3/2$, *bottom:* for $j = 3/2$. The dashed lines indicate the ratio involving proton-impact j -changing collisions (indicated with q_{ul}^p), the solid lines are for electron-impact collisions. (b) Transition rate coefficient as a function of temperature. The dashed, dotted, and solid lines indicate values corresponding to proton-impact 2–4 transition, electron-impact 2–4 transition and electron-impact 1–2 transition, respectively. The electron-impact data was obtained from Mao et al. (2022) and the proton-impact values from Zygelman and Dalgarno (1987).

In the low density limit ($n_{\text{gas}} < n_{\text{crit}}$), radiative emission is faster than the rate of collisions. Hereby we will call this the radiative limit. Here, the density of our gas is sufficiently low enough to ignore collisional transitions, so the j -changing transitions are negligible. On the other hand, the limit in which the rate of collisions are much faster than spontaneous emissions is at thermodynamic equilibrium ($n_{\text{gas}} > n_{\text{crit}}$). We will refer to this limit as the collisional limit. Here, n_2/n_4 becomes equal to the ratio of the statistical weights of the corresponding levels.

Figure 6.4a shows n_{crit} for proton- and electron-impact collisions for four one-electron ions (C VI, Mg XII, S XVI, Ar XVIII), and Figure 6.4b shows the rate coefficients used to compute n_{crit} . The lack of proton collision rates is a pressing atomic data need for the next generation of X-ray observatories. Electron collisional data with fine structure given in Mao et al. (2022) was used to calculate the electron rates q_{ul} with the following well-known relation

$$q_{lu} = \frac{8.63 \times 10^{-6} \Omega(l, u)}{g_u T^{1/2}} \text{cm}^3 \text{s}^{-1}, \quad (6.11)$$

where g_u is the statistical weight of the upper level, and T is the temperature of the ionized gas. However, expect proton rates to be more important at lower temperatures (Bahcall and Wolf, 1968; Zygelman and Dalgarno, 1987). We can see this by extrapolating the plot-lines in Figure 6.4b, where for most one-electron species $q_{24} > q_{24}^p$ at lower T . A general theory for ion-ion collisions is given by Walling and Weisheit (1988) and Igarashi et al. (2003) give cross sections of proton-impact excitation between the $n = 2$ fine-structure levels of hydrogenic ions.

As all of CLOUDY is designed for densities lower than 10^{20} cm^3 , Figure 6.4a confirms we may reasonably assume the radiative limit and that j-changing collisions can be ignored. The critical densities for all hydrogenic species heavier than C VI shown in Figure 6.4a is above 10^{20} cm^3 . We also show that $A_{21} > A_{42}$ for all species, as expected. For example, the gas densities of typical H II regions are $\sim 10^4 \text{ cm}^3$ which is well below the above-mentioned values of n_{crit} .

6.4.4 Escape & Destruction Probabilities

The escape probability is an approximation that treats the effects of radiative trapping on resonant lines. The code uses various theories to calculate the escape probability, depending on the classification of the line (see, e.g., Section 3.4 in Rutten, 2003). For hydrogen Ly α , the code uses fits to the results presented in Hummer and Kunasz (1980, hereafter HK80), which takes the Voigt line profile into account. During the present study we found a simple coding error in the normalization of the Voigt line profile, which has been present in the code since at least the 1990s. The correction has been published in the C23.01 sub-release (Gunasekera et al., 2023b).

A problem with the HK80 theory is that it implicitly assumes the line to be single, i.e., it does not consider the line overlap problem for the two fine-structure components of the Ly α line. Below, we will show how we modify the theory to deal with this problem.

The starting point of the theory presented in HK80 is the β parameter, which is defined as (Eq. 2.7 of HK80):

$$\beta \equiv k_c/k_L, \quad (6.12)$$

The line opacity is defined as (Eq. 2.3 of HK80):

$$k_L = \frac{N_1 B_{12} h \nu_0}{4\pi \Delta}. \quad (6.13)$$

This can be simplified to (Eq. 8 of [cite C23.01]):

$$k_L = N_1 \kappa_L \sqrt{\pi} / \Delta_v. \quad (6.14)$$

The line profile $k(x)$ that needs to be entered into the fine opacity array (see Shaw et al., 2005 for a more detailed discussion of the fine opacity array) is given by:

$$k(x) = k_L \frac{1}{\sqrt{\pi}} H(a, x) = \frac{N_1 \kappa_L}{\Delta_v} H(a, x), \quad (6.15)$$

where a and x are defined in HK80, and $H(a, x)$ is the familiar Voigt function defined by Eq. 2.4 of the same paper. Since $H(a, 0) = \exp(a^2) \operatorname{erfc}(a) \approx 1$ for $a \ll 1$, we get:

$$k_L \approx k(0)\sqrt{\pi}. \quad (6.16)$$

This latter equation can be used to generalise the treatment for overlapping lines. Instead of using Eq. 6.14 to calculate β , as was done in previous versions of the code¹, we will now use Eq. 6.16. This version will automatically treat line overlap when $k(0)$ is taken from the fine opacity array after all lines have been added into it. One drawback of this approach is that in general the overlapping lines will no longer have the shape of a Voigt profile, which is implicitly assumed by HK80. However, since the fine-structure components are very closely spaced in H Ly α , and in most environments the H Ly α lines will strongly dominate over other blended lines, this is expected to be a minor problem. We are not aware of a theory that presents a full treatment of line overlap in this context.

The calculations of the destruction probabilities due to the continuum opacity suffer the same problem of not allowing for overlapping lines. It is the lines from high-charge ions with transitions from nP_j to lower n levels that exhibit line overlapping. For these lines, we simply treat the doublets as two separate lines by adding the opacity of the two j -components to calculate the β for the destruction probability.

6.5 Results of Simulating high-resolution X-ray spectra

Figure 6.5, shows the CLOUDY predicted total emission spectra for the energy range 0.1 - 10 keV, for a model of the Perseus Cluster. Predictions from both before and after resolving the one-electron fine-structure Lyman lines are shown for comparison. This energy range is covered by the *XRISM* mission, and includes the important Fe $K\alpha$ doublet. The y-axis here has been scaled by the thickness of the cloud Δr , since the line intensities can depend on the Δr . νF_ν is the total emitted continuum and is the observed emission if the photoionized clouds were to cover the continuum source uniformly. The input script for this photoionization model is provided in Appendix 7.

With the spectral resolution implemented (1/10 of *Athena*'s energy resolution, $R \sim 0.25$ eV) we see that CLOUDY now predicts Lyman doublets for all H-like species heavier than nitrogen. Since this update provides an energy accuracy beyond the current and future X-ray microcalorimeter spectral resolution (as shown by Figure 6.2), the improved CLOUDY spectra will be in excellent agreement with microcalorimeter observations.

¹In the process of implementing this, we discovered a bug in CLOUDY versions C23.00 and before where the factor $\sqrt{\pi}$ was placed in the denominator rather than the numerator. This bug only affected the calculation of β (and hence the destruction probability), not the line profile given in Eq. 6.15. This bug was fixed in version C23.01.

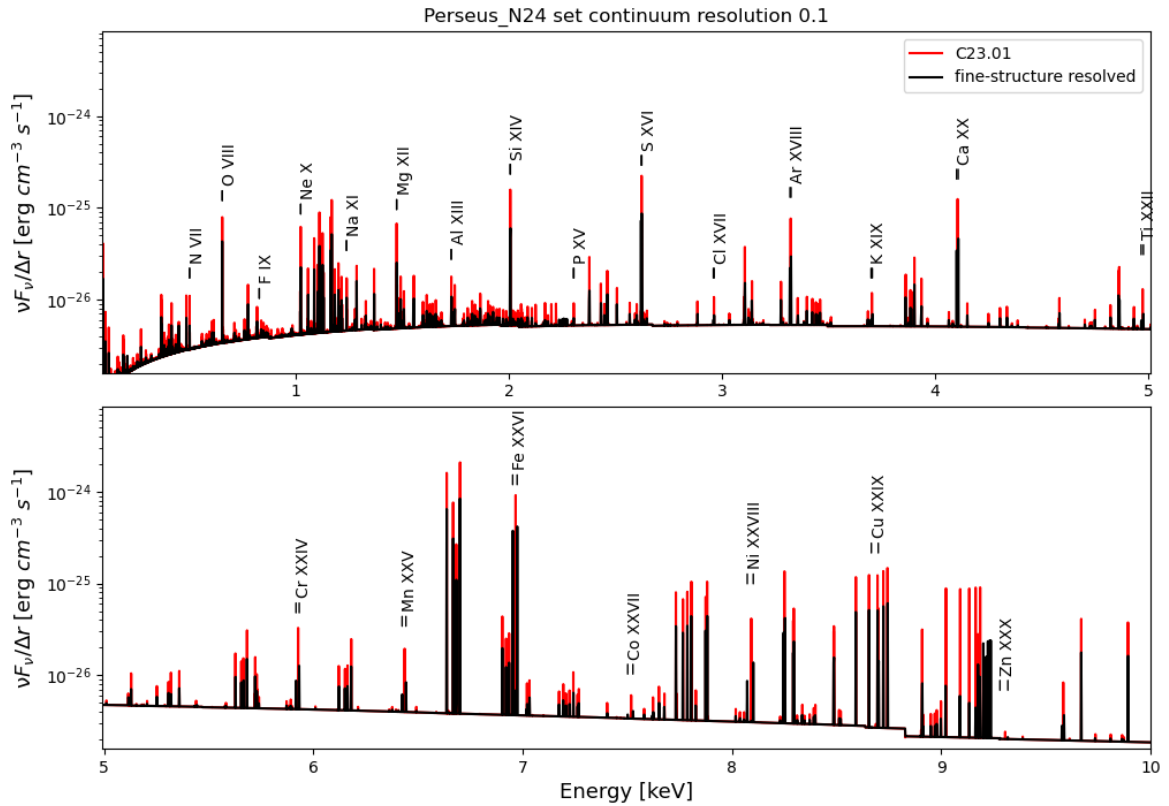


Figure 6.5: Cloudy predicted X-ray spectra of the Perseus Cluster. *Red*: Spectra simulated using the C23.01 release of CLOUDY that does not have H-like fine-structure splitting of the nP levels. *Black*: Spectra simulated using the current development version of CLOUDY with the one-electron fine-structure Lyman doublets.

Chapter 7 Conclusions

In my PhD thesis, I improved micro-physical calculations involved in spectral modeling, discussed processes that affect the chemical evolution of the cosmos, and developed tools to keep up with the ever-improving atomic databases. This work involved multiple developments to the spectral simulation code CLOUDY and simulating spectra of extragalactic star-forming H II regions to compare with observations of the MaNGA survey.

I found that the intensity of line ratios in a model of the Orion Nebula are significantly affected by depletions onto dust grains. I found that adjusting dust abundances along with depletion affects the structure and the overall temperature of the H⁺ layer across the H II region.

I found that the depletion strength has a non-trivial effect on predicted emission lines and the thermal balance of the ionized interstellar cloud. I found that the amount by which elements deplete also affects the coolant abundances in the gas. Furthermore, I found that each of the parameters - metallicity, ionization parameter U and depletion strength F_* have degenerate effects on the emission-line strengths, and thermal balance of the interstellar medium (ISM). Finally, comparing the results to a sample of data obtained MaNGA survey I found that the best-fit F_* was approximately 0.5 for star-forming extragalactic H II regions. However, this best-fit value does not work well for all metallicities. I found that removing the sulfur depletion and changing the nitrogen abundance pattern can improve the fit. As a result, extra observational evidence is required to verify the choices of parameters and better constrain the typical depletion strength in galaxies.

I developed a script that will allow CLOUDY to keep up with future changes to the CHIANTI database with no changes to its source code, (the script is open-access at <https://gitlab.nublado.org/cloudy/arrack>). I found that updating the atomic database improved the line wavelengths of several electron-excitation transitions, and also improved the spectral line intensities predicted by CLOUDY.

I have successfully identified and corrected a factor of π error in CLOUDY's normalisation of the H Ly α optical depth. This affects the destruction of H I Ly α by background opacities. The largest effect is upon the Ly α intensity in high-ionization dusty clouds, where the predicted intensity is now up to three times stronger. Other properties that depend on Ly α destruction, such as grain infrared emission, change in response. These effects will be presented and discussed in the next C24.00 release of CLOUDY.

I resolved the H-like Lyman lines in CLOUDY. Starting by providing new fine-structure energy level calculations for the nP_j states, I self-consistently expanded the micro-physical calculations conducted by CLOUDY to predicting j-resolved Lyman doublets for all one-electron atom/ions. This project was motivated by the launch of the high-resolution microcalorimeter mission *XRISM* (R > 1000). The present updates has achieved predicted spectral resolution to reaching beyond the needs of present and future microcalorimeter observational missions.

Copyright© Chamani M. Gunasekera, 2024.

Appendices

Appendix A: Bethe Logarithm

The Bethe logarithm $\ln(K_0/Z^2 Ry)$ is a dimensionless quantity, where $K_0(n, l)$ represents the mean excitation energy for the Lamb Shift. It was first introduced by Hans Bethe in 1947 as part of his theory of the Lamb shift (Bethe and Salpeter, 1957). For one-electron atoms with $l \neq 0$, the Bethe logarithm requires the evaluation of oscillator strengths for transitions $nl \rightarrow n', l \pm 1$. Such a calculation can become tedious when evaluating the Bethe logarithm for a large number n . Since $K_0(n, l \neq 0)/Z^2 Ry$ varies slowly with n , and does not reduce much smaller than unity for $n \rightarrow \infty$, we can approximate it with a negative exponential. Using an optimized curve fit to the numerical evaluations of the Bethe logarithm presented in Drake and Swainson (1990), for $l = 1$, we find the following approximation,

$$\frac{K_0(n, l = 1)}{Z^2 Ry} \approx 0.0495e^{-0.543n} + 0.953. \quad (1)$$

Figure 1 shows our fit evaluated for n up to $n = 20$ and compared with the values in Drake and Swainson (1990). We find that Equation 1 provides a sufficiently good fit, especially for low $n < 10$, with a mean square error of order 10^{-7} .

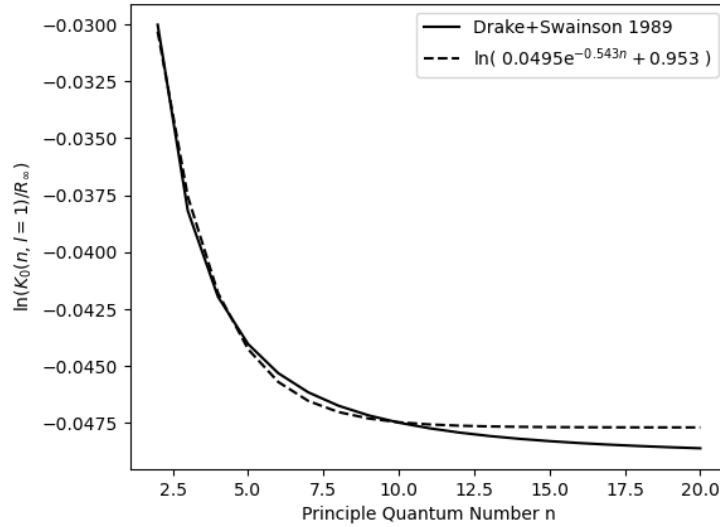


Figure 1: Log fit of the exponential of the Bethe logarithm values presented in Drake and Swainson (1990) for orbital angular quantum number $l = 1$.

Appendix B: Perseus Photoionization Model

```
set save prefix "Perseus_N24"
constant temperature 4.7e7K
iterate
hden -1.5
set continuum resolution 0.1
metal solar 0.65 linear
stop column density 24
turbulence 150km/s
species "Fe+25" levels=all
save emitted continuum intensity ".econ" last no hash
```

Appendix C: Burgess and Tully Scaling

CLOUDY utilizes collisional data from various sources for its microphysical calculations. The collisional data in the CHIANTI database, however, are scaled using the BT method. CLOUDY has to convert the CHIANTI collisional data from BT space to physical units. Below I review the equations for BT scaling, which I use in our analysis in Section 4.2.3.

The BT method describes a way to scale electron-impact collision strengths of positive ions in a compact form. In this procedure, both collision strengths and temperatures are mapped onto a finite range of values, based on the type of transition BT. For temperature, this is an interval of (0, 1) for all transition types. Although the original BT publication discusses only four types of transitions (optically allowed non-zero gf, allowed small gf, forbidden, and exchange), work on CHIANTI has introduced two additional transition types.

The classification of the transitions and the descaling equations are as follows:

Type 1 Optically allowed transitions with non-zero oscillator strengths.

$$\Upsilon = \Upsilon_{BT} \ln \left(\frac{kT}{E_{ij}} + \exp 1 \right)$$

Type 2 Optically forbidden transitions induced by an electric or a magnetic multipole interaction.

$$\Upsilon = \Upsilon_{BT}$$

Type 3 Transition induced by exchange between incident and bound electrons resulting in a change in the spin of the ion.

$$\Upsilon = \frac{\Upsilon_{BT}}{\frac{kT}{E_{ij}} + 1}$$

Type 4 Similar to Type 1 transition: an optically allowed transition but with a very low oscillator strength.

$$\Upsilon = \Upsilon_{BT} \ln \left(\frac{kT}{E_{ij}} + C \right)$$

Type 5 Transition involving dielectronic recombination excitation.

$$\Upsilon = \frac{\Upsilon_{BT}}{kT/E_{ij}}$$

Type 6 Forbidden type proton transitions.

$$\Upsilon = 10^{\Upsilon_{BT}}$$

where,

$$\frac{kT}{E_{ij}} = \begin{cases} \exp\left(\frac{\ln(C)}{1-T_{BT}}\right) - C, & \text{Transition Type 1 \& 4} \\ C\left(\frac{T_{BT}}{1-T_{BT}}\right), & \text{Transition Type 2 \& 3} \\ T_{BT}, & \text{Transition Type 6.} \end{cases}$$

and the notation is as follows,

Υ descaled collision strength;

Υ_{BT} collision strength in BT space;

C scaling parameter;

E_{ij} transition energy of $i \rightarrow j$ in unit K.

Appendix D: CHIANTI File Formats

Table D1: Format variation from Ch10 to Ch7.

.elvlc files			
	Ch10	Ch7	Character Columns in Ch7
Column 1	Level Index	Level Index	1-3
Column 2	Level Configuration	Level Configuration	5-26
Column 3	-	Level Label String	omitted
Column 4	Spin Multiplicity ($2S + 1$)	Spin Multiplicity ($2S + 1$)	27
Column 5	Orbital Angular Momentum Symbol (L)	Orbital Angular Momentum Integer (L)	30
Column 6	Total Angular Momentum (J)	Orbital Angular Momentum Symbol (L)	32
Column 7	Observed Energy (cm^{-1})	Total Angular Momentum (J)	35-37
Column 8	Theoretical Energy (cm^{-1})	Statistical Weight ($2J + 1$)	40
Column 9	-	Observed Energy (cm^{-1})	41-55
Column 10	-	Observed Energy (Ry)	56-70
Column 11	-	Theoretical Energy (cm^{-1})	71-85
Column 12	-	Theoretical Energy (Ry)	86-100

Table D1 – continued from previous page

.wgfa files			
	Ch10	Ch7	Character Columns in Ch7
Column 1	Lower Level Index	Lower Level Index	1–5
Column 2	Upper Level Index	Upper Level Index	6–10
Column 3	Wavelength (Angstroms)	Wavelength (Angstroms)	11–25
Column 4	gf Value (weighted oscillator strength)	gf Value	32–40
Column 5	Einstein A (radiative decay rate) (s^{-1})	Einstein A (s^{-1})	47–55
Column 6	Level Configuration	Level Configuration	omitted
.scups and .splups files			
Row 1, Column 1	Lower Level Index	Z (atomic number)	1–3
Row 1, Column 2	Upper Level Index	ion (no. of missing electrons)	4–6
Row 1, Column 3	Energy of Transition (Ry)	Lower Level Index	7–9
Row 1, Column 4	gf Value	Upper Level Index	10–12
Row 1, Column 5	High Temperature Limit (K)	BT92 Transition Type	15
Row 1, Column 6	Number of Scaled Temperatures	gf Value	17–25
Row 1, Column 7	BT Transition Type	Energy of Transition (Ry)	27–35
Row 1, Column 8	BT Scaling Parameter	BT92 Scaling Parameter	37–45
Row 1, Column 9+	-	Scaled Effective Collision Strengths (BT scale)	47+
Row 2	Scaled Temperatures (BT scale)	-	-
Row 3	Scaled Effective Collision Strengths (BT scale)	-	-

Bibliography

- (1986). *Model nebulae*. l'Observatoire de Paris.
- Aguado, D. S., Ahumada, R., Almeida, A., Anderson, S. F., Andrews, B. H., Anguiano, B., Aquino Ortíz, E., Aragón-Salamanca, A., and et al. (2019). The Fifteenth Data Release of the Sloan Digital Sky Surveys: First Release of MaNGA-derived Quantities, Data Visualization Tools, and Stellar Library. *ApJS*, 240(2):23.
- Alimohamadi, P. and Ferland, G. J. (2022). A Practical Guide to the Partition Function of Atoms and Ions. *PASP*, 134(1037):073001.
- Amayo, A., Delgado-Inglada, G., and Stasińska, G. (2021). Ionization correction factors and dust depletion patterns in giant H II regions. *MNRAS*, 505(2):2361–2376.
- Arellano-Córdova, K. Z., Esteban, C., García-Rojas, J., and Méndez-Delgado, J. E. (2021). On the radial abundance gradients of nitrogen and oxygen in the inner Galactic disc. *MNRAS*, 502(1):225–241.
- Badnell, N. R., Ferland, G. J., Gorczyca, T. W., Nikolić, D., and Wagle, G. A. (2015). Bootstrapping Dielectronic Recombination from Second-row Elements and the Orion Nebula. *ApJ*, 804(2):100.
- Bahcall, J. N. and Wolf, R. A. (1968). Fine-Structure Transitions. *ApJ*, 152:701.
- Baldwin, J. A., Ferland, G. J., Martin, P. G., Corbin, M. R., Cota, S. A., Peterson, B. M., and Slettebak, A. (1991). Physical Conditions in the Orion Nebula and an Assessment of Its Helium Abundance. *ApJ*, 374:580.
- Baldwin, J. A., Phillips, M. M., and Terlevich, R. (1981). Classification parameters for the emission-line spectra of extragalactic objects. *PASP*, 93:5–19.
- Bauman, R. P., Porter, R. L., Ferland, G. J., and MacAdam, K. B. (2005). J-Resolved He I Emission Predictions in the Low-Density Limit. *ApJ*, 628(1):541–554.
- Belfiore, F., Maiolino, R., Maraston, C., Emsellem, E., Bershadsky, M. A., Masters, K. L., Yan, R., Bizyaev, D., Boquien, M., Brownstein, J. R., Bundy, K., Drory, N., Heckman, T. M., Law, D. R., Roman-Lopes, A., Pan, K., Stanghellini, L., Thomas, D., Weijmans, A.-M., and Westfall, K. B. (2016). SDSS IV MaNGA - spatially resolved diagnostic diagrams: a proof that many galaxies are LIERs. *MNRAS*, 461(3):3111–3134.
- Bethe, H. A. and Salpeter, E. E. (1957). *Quantum Mechanics of One- and Two-Electron Atoms*. Springer Science & Business Media, 2013.
- Borkowski, K. J. and Harrington, J. P. (1991). A Grain-heated, Dusty Planetary Nebula in M22. *ApJ*, 379:168.

- Bottorff, M., Lamothe, J., Momjian, E., Verner, E., Vinković, D., and Ferland, G. (1998). Luminosity Indicators in Dusty Photoionized Environments. *PASP*, 110(751):1040–1045.
- Bundy, K., Bershad, M. A., Law, D. R., Yan, R., Drory, N., MacDonald, N., Wake, D. A., Cherinka, B., Sánchez-Gallego, J. R., Weijmans, A.-M., Thomas, D., Tremonti, C., Masters, K., Coccatto, L., Diamond-Stanic, A. M., Aragón-Salamanca, A., Avila-Reese, V., Badenes, C., Falcón-Barroso, J., Belfiore, F., Bizyaev, D., Blanc, G. A., Bland-Hawthorn, J., Blanton, M. R., Brownstein, J. R., Byler, N., Cappellari, M., Conroy, C., Dutton, A. A., Emsellem, E., Etherington, J., Frinchaboy, P. M., Fu, H., Gunn, J. E., Harding, P., Johnston, E. J., Kauffmann, G., Kinemuchi, K., Klaene, M. A., Knapen, J. H., Leauthaud, A., Li, C., Lin, L., Maiolino, R., Malanushenko, V., Malanushenko, E., Mao, S., Maraston, C., McDermid, R. M., Merrifield, M. R., Nichol, R. C., Oravetz, D., Pan, K., Parejko, J. K., Sanchez, S. F., Schlegel, D., Simmons, A., Steele, O., Steinmetz, M., Thanjavur, K., Thompson, B. A., Tinker, J. L., van den Bosch, R. C. E., Westfall, K. B., Wilkinson, D., Wright, S., Xiao, T., and Zhang, K. (2015). Overview of the SDSS-IV MaNGA Survey: Mapping nearby Galaxies at Apache Point Observatory. *ApJ*, 798:7.
- Burgess, A. and Tully, J. A. (1992). On the analysis of collision strengths and rate coefficients. *A&A*, 254:436–453.
- Byler, N., Dalcanton, J. J., Conroy, C., and Johnson, B. D. (2017). Nebular Continuum and Line Emission in Stellar Population Synthesis Models. *ApJ*, 840(1):44.
- Calura, F., Dessauges-Zavadski, M., Prochaska, J. X., and Matteucci, F. (2009). Constraining the Star Formation Histories of Gamma-Ray Burst Host Galaxies from their Observed Abundance Patterns. *ApJ*, 693(2):1236–1249.
- Canizares, C. R., Davis, J. E., Dewey, D., Flanagan, K. A., Galton, E. B., Huenemoerder, D. P., Ishibashi, K., Markert, T. H., Marshall, H. L., McGuirk, M., Schattenburg, M. L., Schulz, N. S., Smith, H. I., and Wise, M. (2005). The Chandra High-Energy Transmission Grating: Design, Fabrication, Ground Calibration, and 5 Years in Flight. *PASP*, 117(836):1144–1171.
- Chakraborty, P., Ferland, G. J., Chatzikos, M., Fabian, A. C., Bianchi, S., Guzmán, F., and Su, Y. (2022). X-Ray Spectroscopy in the Microcalorimeter Era 4: Optical Depth Effects on the Soft X-Rays Studied with CLOUDY. *ApJ*, 935(2):70.
- Chakraborty, P., Ferland, G. J., Chatzikos, M., Guzmán, F., and Su, Y. (2020a). X-Ray Spectroscopy in the Microcalorimeter Era. I. Effects of Fe XXIV Resonant Auger Destruction on Fe XXV $K\alpha$ Spectra. *ApJ*, 901(1):68.
- Chakraborty, P., Ferland, G. J., Chatzikos, M., Guzmán, F., and Su, Y. (2020b). X-Ray Spectroscopy in the Microcalorimeter Era. II. A New Diagnostic on Column Density from the Case A to B Transition in H- and He-like Iron. *ApJ*, 901(1):69.

- Chakraborty, P., Ferland, G. J., Chatzikos, M., Guzmán, F., and Su, Y. (2021). X-Ray Spectroscopy in the Microcalorimeter Era. III. Line Formation under Case A, Case B, Case C, and Case D in H- and He-like Iron for a Photoionized Cloud. *ApJ*, 912(1):26.
- Chatzikos, M., Bianchi, S., Camilloni, F., Chakraborty, P., Gunasekera, C. M., Guzmán, F., Milby, J. S., Sarkar, A., Shaw, G., van Hoof, P. A. M., and Ferland, G. J. (2023). The 2023 Release of Cloudy. *Rev. Mex. Astron. Astrofis.*, 59:327–343.
- Chatzikos, M., Williams, R. J. R., Ferland, G. J., Canning, R. E. A., Fabian, A. C., Sanders, J. S., van Hoof, P. A. M., Johnstone, R. M., Lykins, M., and Porter, R. L. (2015). Implications of coronal line emission in NGC 4696*. *MNRAS*, 446(2):1234–1244.
- Cota, S. A. (1987). *The Astrophysics of Nebulae and Active Galactic Nuclear Emission-Line Regions: New Methods and Applications*. PhD thesis, The Ohio State University.
- Cowie, L. L. and Songaila, A. (1986). High-resolution optical and ultraviolet absorption-line studies of interstellar gas. *ARA&A*, 24:499–535.
- Crinklaw, G., Federman, S. R., and Joseph, C. L. (1994). The Depletion of Calcium in the Interstellar Medium. *ApJ*, 424:748.
- D’Agostino, J. J., Kewley, L. J., Groves, B., Byler, N., Sutherland, R. S., Nicholls, D., Leitherer, C., and Stanway, E. R. (2019). Comparison of Theoretical Starburst Photoionization Models for Optical Diagnostics. *ApJ*, 878(1):2.
- de Souza, R. S., Dantas, M. L. L., Costa-Duarte, M. V., Feigelson, E. D., Killedar, M., Lablanche, P. Y., Vilalta, R., Krone-Martins, A., Beck, R., and Gieseke, F. (2017). A probabilistic approach to emission-line galaxy classification. *MNRAS*, 472(3):2808–2822.
- Del Zanna, G., Dere, K. P., Young, P. R., and Landi, E. (2021). CHIANTI—An Atomic Database for Emission Lines. XVI. Version 10, Further Extensions. *ApJ*, 909(1):38.
- Del Zanna, G., Dere, K. P., Young, P. R., Landi, E., and Mason, H. E. (2015). CHIANTI - An atomic database for emission lines. Version 8. *A&A*, 582:A56.
- Dere, K. P., Landi, E., Mason, H. E., Monsignori Fossi, B. C., and Young, P. R. (1997). CHIANTI - an atomic database for emission lines. *A&AS*, 125:149–173.
- Dopita, M. A., Groves, B. A., Sutherland, R. S., Binette, L., and Cecil, G. (2002). Are the Narrow-Line Regions in Active Galaxies Dusty and Radiation Pressure Dominated? *ApJ*, 572:753–761.

- Dopita, M. A., Sutherland, R. S., Nicholls, D. C., Kewley, L. J., and Vogt, F. P. A. (2013). New Strong-line Abundance Diagnostics for H II Regions: Effects of κ -distributed Electron Energies and New Atomic Data. *ApJS*, 208:10.
- Draine, B. T. (2011). *Physics of the Interstellar and Intergalactic Medium*. Princeton University Press.
- Drake, G. W. F. (2006). *Springer Handbook of Atomic, Molecular, and Optical Physics*. Springer Science & Business Media, 2006.
- Drake, G. W. F. and Swainson, R. A. (1990). Bethe logarithms for hydrogen up to $n=20$, and approximations for two-electron atoms. *Phys. Rev. A*, 41(3):1243–1246.
- Duley, W. W. (1985). The abundance of argon as a tracer of accretion efficiency and elemental depletions in diffuse clouds. *ApJ*, 297:296–301.
- Elitzur, M. (1992). *Astronomical masers*, volume 170. Springer Netherlands.
- Ferguson, J. W. and Ferland, G. J. (1997). Accurate Hydrogen Spectral Simulations with a Compact Model Atom. *ApJ*, 479(1):363–370.
- Ferland, G. (1999). The Spectrum of a Single Photoionized Cloud. In Ferland, G. and Baldwin, J., editors, *Quasars and Cosmology*, volume 162 of *Astronomical Society of the Pacific Conference Series*, page 147.
- Ferland, G. J. (1980). Hydrogenic emission and recombination coefficients for a wide range of temperature and wavelength. *PASP*, 92:596–602.
- Ferland, G. J. (2006). *Hazy, A Brief Introduction to Cloudy 06.02*. University of Kentucky Internal Report.
- Ferland, G. J., Chatzikos, M., Guzmán, F., Lykins, M. L., van Hoof, P. A. M., Williams, R. J. R., Abel, N. P., Badnell, N. R., Keenan, F. P., Porter, R. L., and Stancil, P. C. (2017). The 2017 Release Cloudy. *Rev. Mex. Astron. Astrofis.*, 53:385–438.
- Ferland, G. J., Izotov, Y., Peimbert, A., Peimbert, M., Porter, R. L., Skillman, E., and Steigman, G. (2010). What is ^4He from H II regions? What needs to be done to better understand the systematic errors? In Charbonnel, C., Tosi, M., Primas, F., and Chiappini, C., editors, *Light Elements in the Universe*, volume 268 of *Proceedings of the International Astronomical Union*, pages 163–167.
- Ferland, G. J., Korista, K. T., Verner, D. A., Ferguson, J. W., Kingdon, J. B., and Verner, E. M. (1998). CLOUDY 90: Numerical Simulation of Plasmas and Their Spectra. *PASP*, 110(749):761–778.
- Ferland, G. J. and Persson, S. E. (1989). Implications of CA II Emission for Physical Conditions in the Broad-Line Region of Active Galactic Nuclei. *ApJ*, 347:656.

- Ferland, G. J., Porter, R. L., van Hoof, P. A. M., Williams, R. J. R., Abel, N. P., Lykins, M. L., Shaw, G., Henney, W. J., and Stancil, P. C. (2013). The 2013 Release of Cloudy. *Rev. Mex. Astron. Astrofis.*, 49:137–163.
- Ferland, G. J. and Rees, M. J. (1988). Radiative Equilibrium of High-Density Clouds, with Application to Active Galactic Nucleus Continua. *ApJ*, 332:141.
- Ferrière, K. M. (2001). The interstellar environment of our galaxy. *Reviews of Modern Physics*, 73(4):1031–1066.
- Frontera, F., Greiner, J., Antonelli, L. A., Costa, E., Fiore, F., Parmar, A. N., Piro, L., Boller, T., and Voges, W. (1998). High resolution imaging of the X-ray afterglow of GRB970228 with ROSAT. *A&A*, 334:L69–L72.
- Garmire, G. P., Bautz, M. W., Ford, P. G., Nousek, J. A., and Ricker, George R., J. (2003). Advanced CCD imaging spectrometer (ACIS) instrument on the Chandra X-ray Observatory. In Truemper, J. E. and Tananbaum, H. D., editors, *X-Ray and Gamma-Ray Telescopes and Instruments for Astronomy.*, volume 4851 of *Society of Photo-Optical Instrumentation Engineers (SPIE) Conference Series*, pages 28–44.
- Garnett, D. R. (1989). The Abundance of Sulfur in Extragalactic H II Regions. *ApJ*, 345:282.
- Giacconi, R., Kellogg, E., Gorenstein, P., Gursky, H., and Tananbaum, H. (1971). An X-Ray Scan of the Galactic Plane from UHURU. *ApJ*, 165:L27.
- Gnat, O. and Ferland, G. J. (2012). Ion-by-ion Cooling Efficiencies. *ApJS*, 199(1):20.
- Grevesse, N., Asplund, M., Sauval, A. J., and Scott, P. (2010). The chemical composition of the Sun. *Ap&SS*, 328(1-2):179–183.
- Gunasekera, C. M., Ji, X., Chatzikos, M., Yan, R., and Ferland, G. (2022). Self-consistent grain depletions and abundances I: the Orion Nebula as a test case. *MNRAS*, 512(2):2310–2317.
- Gunasekera, C. M., Ji, X., Chatzikos, M., Yan, R., and Ferland, G. (2023a). Self consistent grain depletions and abundances II: Effects on strong-line diagnostics of extragalactic H II regions. *MNRAS*, 520(3):4345–4355.
- Gunasekera, C. M., van Hoof, P. A. M., Chatzikos, M., and Ferland, G. J. (2023b). The 23.01 Release of Cloudy. *Research Notes of the American Astronomical Society*, 7(11):246.
- Hafez, I. (2010). *Abd al-Rahman al-Sufi and his book of the fixed stars: a journey of re-discovery*. PhD thesis, James Cook University, Australia.
- Harris, A. W., Gry, C., and Bromage, G. E. (1984). The correlation of interstellar element depletions with mean gas density. *ApJ*, 284:157–160.
- Harrison, T. G. (1984). The Orion Nebula - where in History is it? *QJRAS*, 25:65–79.

- Hensley, B. S. and Draine, B. T. (2021). Observational Constraints on the Physical Properties of Interstellar Dust in the Post-Planck Era. *ApJ*, 906(2):73.
- Herschel, W. (1786). Catalogue of One Thousand New Nebulae and Clusters of Stars. By William Herschel, LL.D. F. R. S. *Philosophical Transactions of the Royal Society of London Series I*, 76:457–499.
- Herschel, W. (1802). Catalogue of 500 new nebulae, nebulous stars, planetary nebulae, and clusters of stars; with remarks on the construction of the heavens. *Philosophical Transactions of the Royal Society of London*, 92:477–528.
- Hillier, D. J. and Miller, D. L. (1998). The Treatment of Non-LTE Line Blanketing in Spherically Expanding Outflows. *ApJ*, 496(1):407–427.
- Hjerting, F. (1938). Tables Facilitating the Calculation of Line Absorption Coefficients. *ApJ*, 88:508.
- Ho, L. C., Filippenko, A. V., and Sargent, W. L. W. (1997). A Search for “Dwarf” Seyfert Nuclei. III. Spectroscopic Parameters and Properties of the Host Galaxies. *ApJS*, 112(2):315–390.
- Hubble, E. P. (1922). The source of luminosity in galactic nebulae. *ApJ*, 56:400–438.
- Hubeny, I. and Mihalas, D. (2014). *Theory of Stellar Atmospheres*. Princeton University Press.
- Huggins, W. (1868). Further Observations on the Spectra of Some of the Stars and Nebulae, with an Attempt to Determine Therefrom Whether These Bodies are Moving towards or from the Earth, Also Observations on the Spectra of the Sun and of Comet II., 1868. *Philosophical Transactions of the Royal Society of London Series I*, 158:529–564.
- Huggins, W. and Miller, W. A. (1864). On the Spectra of Some of the Nebulae. By William Huggins, F.R.A.S. A Supplement to the Paper “On the Spectra of Some of the Fixed Stars William Huggins F.R.A.S., and W. A. Miller, M.D., LL.D., Treas. and V.P.P.S.”. *Philosophical Transactions of the Royal Society of London Series I*, 154:437–444.
- Hummer, D. G. and Kunasz, P. B. (1980). Energy loss by resonance line photons in an absorbing medium. *ApJ*, 236:609–618.
- Igarashi, A., Ohsaki, A., and Nakazaki, S. (2003). Proton-Impact Excitations between the n=2 Fine-Structure Levels of Hydrogenic Ions. *Journal of the Physical Society of Japan*, 72(5):1073.
- Jenkins, E. B. (1987). Element Abundances in the Interstellar Atomic Material. In Hollenbach, D. J. and Thronson, Harley A., J., editors, *Interstellar Processes*, volume 134, page 533.

- Jenkins, E. B. (2009). A Unified Representation of Gas-Phase Element Depletions in the Interstellar Medium. *ApJ*, 700(2):1299–1348.
- Jenkins, E. B., Drake, J. F., Morton, D. C., Rogerson, J. B., Spitzer, L., and York, D. G. (1973). Spectrophotometric Results from the Copernicus Satellite. V. Abundances of Molecules in Interstellar Clouds. *ApJ*, 181:L122.
- Jenkins, E. B., Savage, B. D., and Spitzer, L., J. (1986). Abundances of Interstellar Atoms from Ultraviolet Absorption Lines. *ApJ*, 301:355.
- Ji, X. and Yan, R. (2020). Constraining photoionization models with a reprojected optical diagnostic diagram. *MNRAS*, 499(4):5749–5764.
- Ji, X., Yan, R., Riffel, R., Drory, N., and Zhang, K. (2020). Upper boundaries of AGN regions in optical diagnostic diagrams. *MNRAS*.
- Jitrik, O. and Bunge, C. F. (2004). Transition Probabilities for Hydrogen-Like Atoms. *Journal of Physical and Chemical Reference Data*, 33(4):1059–1070.
- Kauffmann, G., Heckman, T. M., Tremonti, C., Brinchmann, J., Charlot, S., White, S. D. M., Ridgway, S. E., Brinkmann, J., Fukugita, M., Hall, P. B., Ivezić, Ž., Richards, G. T., and Schneider, D. P. (2003). The host galaxies of active galactic nuclei. *MNRAS*, 346(4):1055–1077.
- Kellogg, E. M., Gursky, H., Leong, C., Tananbaum, H., and Giacconi, R. (1971). X-Ray Emission from the M-87 Region as seen from Uhuru. In *Bulletin of the American Astronomical Society*, volume 3, page 236.
- Kewley, L. J., Dopita, M. A., Sutherland, R. S., Heisler, C. A., and Trevena, J. (2001). Theoretical Modeling of Starburst Galaxies. *ApJ*, 556:121–140.
- Kewley, L. J., Groves, B., Kauffmann, G., and Heckman, T. (2006). The host galaxies and classification of active galactic nuclei. *MNRAS*, 372:961–976.
- Kewley, L. J., Nicholls, D. C., Sutherland, R., Rigby, J. R., Acharya, A., Dopita, M. A., and Bayliss, M. B. (2019a). Theoretical ISM Pressure and Electron Density Diagnostics for Local and High-redshift Galaxies. *ApJ*, 880(1):16.
- Kewley, L. J., Nicholls, D. C., and Sutherland, R. S. (2019b). Understanding Galaxy Evolution Through Emission Lines. *ARA&A*, 57:511–570.
- Kramida, A., Yu. Ralchenko, Reader, J., and and NIST ASD Team (2022). NIST Atomic Spectra Database (ver. 5.10), [Online]. Available: <https://physics.nist.gov/asd> [2017, April 9]. National Institute of Standards and Technology, Gaithersburg, MD.
- Kroupa, P. (2001). On the variation of the initial mass function. *MNRAS*, 322(2):231–246.

- Law, D. R., Ji, X., Belfiore, F., Bershady, M. A., Cappellari, M., Westfall, K. B., Yan, R., Bizyaev, D., Brownstein, J. R., Drory, N., and Andrews, B. H. (2021). SDSS-IV MaNGA: Refining Strong Line Diagnostic Classifications Using Spatially Resolved Gas Dynamics. *ApJ*, 915(1):35.
- Leitherer, C., Ekström, S., Meynet, G., Schaerer, D., Agienko, K. B., and Levesque, E. M. (2014). The Effects of Stellar Rotation. II. A Comprehensive Set of Starburst99 Models. *ApJS*, 212(1):14.
- Leitherer, C., Schaerer, D., Goldader, J. D., Delgado, R. M. G., Robert, C., Kune, D. F., de Mello, D. F., Devost, D., and Heckman, T. M. (1999). Starburst99: Synthesis Models for Galaxies with Active Star Formation. *ApJS*, 123(1):3–40.
- Lodders, K. (2003). Solar System Abundances and Condensation Temperatures of the Elements. *ApJ*, 591(2):1220–1247.
- Lodders, K. and Palme, H. (2009). Solar System Elemental Abundances in 2009. *Meteoritics and Planetary Science Supplement*, 72:5154.
- Lykins, M. L., Ferland, G. J., Kisielius, R., Chatzikos, M., Porter, R. L., van Hoof, P. A. M., Williams, R. J. R., Keenan, F. P., and Stancil, P. C. (2015). Stout: Cloudy’s Atomic and Molecular Database. *ApJ*, 807(2):118.
- Mao, J., Del Zanna, G., Gu, L., Zhang, C. Y., and Badnell, N. R. (2022). R-matrix Electron-impact Excitation Data for the H- and He-like Ions with $Z = 6-30$. *ApJS*, 263(2):35.
- Mayall, N. U. (1939). The Crab Nebula, a Probable Supernova. *Leaflet of the Astronomical Society of the Pacific*, 3(119):145.
- Messier, C. (1781). Catalogue des Nébuleuses et des Amas d’Étoiles (Catalog of Nebulae and Star Clusters). *Connaissance des Temps ou des Mouvements Célestes, for 1784*, p. 227-267.
- Mihalas, D. (1970). *Stellar atmospheres*. W H Freeman & Co.
- Mingozzi, M., Belfiore, F., Cresci, G., Bundy, K., Bershady, M., Bizyaev, D., Blanc, G., Boquien, M., Drory, N., Fu, H., Maiolino, R., Riffel, R., Schaefer, A., Storch-Bergmann, T., Telles, E., Tremonti, C., Zakamska, N., and Zhang, K. (2020). SDSS IV MaNGA: Metallicity and ionisation parameter in local star-forming galaxies from Bayesian fitting to photoionisation models. *A&A*, 636:A42.
- Morton, D. C., Drake, J. F., Jenkins, E. B., Rogerson, J. B., Spitzer, L., and York, D. G. (1973). Spectrophotometric Results from the Copernicus Satellite. II. Composition of Interstellar Clouds. *ApJ*, 181:L103.
- Muench, A., Getman, K., Hillenbrand, L., and Preibisch, T. (2008). Star Formation in the Orion Nebula I: Stellar Content. In Reipurth, B., editor, *Handbook of Star Forming Regions, Volume I*, volume 4, page 483.

- Netzer, H., Elitzur, M., and Ferland, G. J. (1985). Bowen fluorescence and He II lines in active galaxies and gaseous nebulae. *ApJ*, 299:752–762.
- Neugebauer, G., Habing, H. J., van Duinen, R., Aumann, H. H., Baud, B., Beichman, C. A., Beintema, D. A., Boggess, N., Clegg, P. E., de Jong, T., Emerson, J. P., Gautier, T. N., Gillett, F. C., Harris, S., Hauser, M. G., Houck, J. R., Jennings, R. E., Low, F. J., Marsden, P. L., Miley, G., Olton, F. M., Pottasch, S. R., Raimond, E., Rowan-Robinson, M., Soifer, B. T., Walker, R. G., Wesselius, P. R., and Young, E. (1984). The Infrared Astronomical Satellite (IRAS) mission. *ApJ*, 278:L1–L6.
- Osterbrock, D. E. and Ferland, G. J. (2006). *Astrophysics of gaseous nebulae and active galactic nuclei*. University Science Books.
- Pauldrach, A. W. A., Hoffmann, T. L., and Lennon, M. (2001). Radiation-driven winds of hot luminous stars. XIII. A description of NLTE line blocking and blanketing towards realistic models for expanding atmospheres. *A&A*, 375:161–195.
- Peimbert, M. and Torres-Peimbert, S. (1977). Chemical composition of the Orion Nebula. *MNRAS*, 179:217–234.
- Polletta, M., Tajer, M., Maraschi, L., Trinchieri, G., Lonsdale, C. J., Chiappetti, L., Andreon, S., Pierre, M., Le Fèvre, O., Zamorani, G., Maccagni, D., Garcet, O., Surdej, J., Franceschini, A., Alloin, D., Shupe, D. L., Surace, J. A., Fang, F., Rowan-Robinson, M., Smith, H. E., and Tresse, L. (2007). Spectral Energy Distributions of Hard X-Ray Selected Active Galactic Nuclei in the XMM-Newton Medium Deep Survey. *ApJ*, 663(1):81–102.
- Porter, R. L., Bauman, R. P., Ferland, G. J., and MacAdam, K. B. (2005). Theoretical He I Emissivities in the Case B Approximation. *ApJ*, 622(1):L73–L75.
- Porter, R. L., Ferland, G. J., and MacAdam, K. B. (2007). He I Emission in the Orion Nebula and Implications for Primordial Helium Abundance. *ApJ*, 657(1):327–337.
- Porter, R. L., Ferland, G. J., MacAdam, K. B., and Storey, P. J. (2009). Uncertainties in theoretical He I emissivities: H II regions, primordial abundance and cosmological recombination. *MNRAS*, 393(1):L36–L40.
- Porter, R. L., Ferland, G. J., Storey, P. J., and Detisch, M. J. (2012). Improved He I emissivities in the case B approximation. *MNRAS*, 425(1):L28–L31.
- Raymond, J. C. and Smith, B. W. (1977). Soft X-ray spectrum of a hot plasma. *ApJS*, 35:419–439.
- Rogerson, J. B., Spitzer, L., Drake, J. F., Dressler, K., Jenkins, E. B., Morton, D. C., and York, D. G. (1973a). Spectrophotometric Results from the Copernicus Satellite. I. Instrumentation and Performance. *ApJ*, 181:L97–L102.

- Rogerson, J. B., York, D. G., Drake, J. F., Jenkins, E. B., Morton, D. C., and Spitzer, L. (1973b). Spectrophotometric Results from the Copernicus Satellite. III. Ionization and Composition of the Intercloud Medium. *ApJ*, 181:L110.
- Rogerson, J. B., York, D. G., Drake, J. F., Jenkins, E. B., Morton, D. C., and Spitzer, L. (1973c). Spectrophotometric Results from the Copernicus Satellite. III. Ionization and Composition of the Intercloud Medium. *ApJ*, 181:L110.
- Rubin, R. H., Simpson, J. P., Haas, M. R., and Erickson, E. F. (1991). Axisymmetric Model of the Ionized Gas in the Orion Nebula. *ApJ*, 374:564.
- Rudd, M. E. (1993). The Long and the Short of It: Telescopes of the Seventeenth Century. *Journal of the Antique Telescope Society*, 4:12–19.
- Rutten, R. J. (2003). *Radiative Transfer in Stellar Atmospheres*. Springer Science & Business Media, 2003.
- Rybicki, G. B. and Lightman, A. P. (1979). *Radiative processes in astrophysics*. John Wiley & Sons, Inc.
- Salpeter, E. E. (1977). Formation and destruction of dust grains. *ARA&A*, 15:267–293.
- Savage, B. D. and Bohlin, R. C. (1979). The depletion of interstellar gaseous iron. *ApJ*, 229:136–146.
- Savage, B. D. and Mathis, J. S. (1979). Observed properties of interstellar dust. *ARA&A*, 17:73–111.
- Schaefer, A. L., Tremonti, C., Belfiore, F., Pace, Z., Bershady, M. A., Andrews, B. H., and Drory, N. (2020). SDSS-IV MaNGA: Variations in the N/O-O/H Relation Bias Metallicity Gradient Measurements. *ApJ*, 890(1):L3.
- Schöier, F. L., van der Tak, F. F. S., van Dishoeck, E. F., and Black, J. H. (2005). An atomic and molecular database for analysis of submillimetre line observations. *A&A*, 432(1):369–379.
- Shaw, G., Ferland, G. J., Abel, N. P., Stancil, P. C., and van Hoof, P. A. M. (2005). Molecular Hydrogen in Star-forming Regions: Implementation of its Microphysics in CLOUDY. *ApJ*, 624(2):794–807.
- Spitzer, L. (1978). *Physical processes in the interstellar medium*. Wiley.
- Spitzer, L., Drake, J. F., Jenkins, E. B., Morton, D. C., Rogerson, J. B., and York, D. G. (1973a). Spectrophotometric Results from the Copernicus Satellite. IV. Molecular Hydrogen in Interstellar Space. *ApJ*, 181:L116.
- Spitzer, L., Drake, J. F., Jenkins, E. B., Morton, D. C., Rogerson, J. B., and York, D. G. (1973b). Spectrophotometric Results from the Copernicus Satellite. IV. Molecular Hydrogen in Interstellar Space. *ApJ*, 181:L116.

- Stasińska, G., Cid Fernandes, R., Mateus, A., Sodré, L., and Asari, N. V. (2006). Semi-empirical analysis of Sloan Digital Sky Survey galaxies - III. How to distinguish AGN hosts. *MNRAS*, 371(2):972–982.
- Strüder, L., Briel, U., Dennerl, K., Hartmann, R., Kendziorra, E., Meidinger, N., Pfeffermann, E., Reppin, C., Aschenbach, B., Bornemann, W., Bräuninger, H., Burkert, W., Elender, M., Freyberg, M., Haberl, F., Hartner, G., Heuschmann, F., Hippmann, H., Kastelic, E., Kemmer, S., Kettenring, G., Kink, W., Krause, N., Müller, S., Oppitz, A., Pietsch, W., Popp, M., Predehl, P., Read, A., Stephan, K. H., Stötter, D., Trümper, J., Holl, P., Kemmer, J., Soltau, H., Stötter, R., Weber, U., Weichert, U., von Zanthier, C., Carathanassis, D., Lutz, G., Richter, R. H., Solc, P., Böttcher, H., Kuster, M., Staubert, R., Abbey, A., Holland, A., Turner, M., Balasini, M., Bignami, G. F., La Palombara, N., Villa, G., Buttler, W., Gianini, F., Lainé, R., Lumb, D., and Dhez, P. (2001). The European Photon Imaging Camera on XMM-Newton: The pn-CCD camera. *A&A*, 365:L18–L26.
- Takahashi, T., Kokubun, M., Mitsuda, K., Kelley, R. L., Ohashi, T., Aharonian, F., Akamatsu, H., Akimoto, F., Allen, S. W., Anabuki, N., Angelini, L., Arnaud, K., Asai, M., Audard, M., Awaki, H., Axelsson, M., Azzarello, P., Baluta, C., Bamba, A., Bando, N., Bautz, M. W., Bialas, T., Blandford, R., Boyce, K., Brenneman, L. W., Brown, G. V., Bulbul, E., Cackett, E. M., Canavan, E., Chernyakova, M., Chiao, M. P., Coppi, P. S., Costantini, E., O’Dell, S., DiPirro, M., Done, C., Dotani, T., Doty, J., Ebisawa, K., Eckart, M. E., Enoto, T., Ezoe, Y., Fabian, A. C., Ferrigno, C., Foster, A. R., Fujimoto, R., Fukazawa, Y., Funk, S., Furuzawa, A., Galeazzi, M., Gallo, L. C., Gandhi, P., Gilmore, K., Giustini, M., Goldwurm, A., Gu, L., Guainazzi, M., Haas, D., Haba, Y., Hagino, K., Hamaguchi, K., Har-rus, I. M., Hatsukade, I., Hayashi, T., Hayashi, K., Hayashida, K., den Herder, J.-W., Hiraga, J. S., Hirose, K., Hornschemeier, A., Hoshino, A., Hughes, J. P., Ichinohe, Y., Iizuka, R., Inoue, H., Inoue, Y., Ishibashi, K., Ishida, M., Ishikawa, K., Ishimura, K., Ishisaki, Y., Itoh, M., Iwai, M., Iwata, N., Iyomoto, N., Jewell, C., Kaastra, J., Kallman, T., Kamae, T., Kara, E., Kataoka, J., Katsuda, S., Katsuta, J., Kawaharada, M., Kawai, N., Kawano, T., Kawasaki, S., Khangulyan, D., Kilbourne, C. A., Kimball, M., King, A., Kitaguchi, T., Kitamoto, S., Kitayama, T., Kohmura, T., Konami, S., Kosaka, T., Koujelev, A., Koyama, K., Koyama, S., Kretschmar, P., Krimm, H. A., Kubota, A., Kunieda, H., Laurent, P., Lee, S.-H., Leutenegger, M. A., Limousin, O., Loewenstein, M., Long, K. S., Lumb, D., Madejski, G., Maeda, Y., Maier, D., Makishima, K., Markevitch, M., Masters, C., Matsumoto, H., Matsushita, K., McCammon, D., Mcguinness, D., McNamara, B. R., Mehdipour, M., Miko, J., Miller, E. D., Miller, J. M., Mineshige, S., Minesugi, K., Mitsuishi, I., Miyazawa, T., Mizuno, T., Mori, H., Mori, K., Moroso, F., Moseley, H., Muench, T., Mukai, K., Murakami, H., Murakami, T., Mushotzky, R. F., Nagano, H., Nagino, R., Nakagawa, T., Nakajima, H., Nakamori, T., Nakano, T., Nakashima, S., Nakazawa, K., Namba, Y., Natsukari, C., Nishioka, Y., Nobukawa, K. K., Nobukawa, M., Noda, H., Nomachi, M., Odaka, H., Ogawa, H., Ogawa, M., Ogi, K., Ohno, M., Ohta, M., Okajima, T., Okamoto, A., Okazaki, T., Ota, N.,

- Ozaki, M., Paerels, F., Paltani, S., Parmar, A., Petre, R., Pinto, C., de Plaa, J., Pohl, M., Pontius, J., Porter, F. S., Pottschmidt, K., Ramsey, B., Reynolds, C., Russell, H., Safi-Harb, S., Saito, S., Sakai, K., Sakai, S.-i., Sameshima, H., Sasaki, T., Sato, G., Sato, K., Sato, R., Sato, Y., Sawada, M., Schartel, N., Serlemitsos, P. J., Seta, H., Shibano, Y., Shida, M., Shidatsu, M., Shimada, T., Shinozaki, K., Shirron, P., Simionescu, A., Simmons, C., Smith, R. K., Sneiderman, G., Soong, Y., Stawarz, L., Sugawara, Y., Sugita, S., Sugita, H., Szymkowiak, A., Tajima, H., Takahashi, H., Takeda, S., Takei, Y., Tamagawa, T., Tamura, T., Tamura, K., Tanaka, T., Tanaka, Y., Tanaka, Y. T., Tashiro, M. S., Tawara, Y., Terada, Y., Terashima, Y., Tombesi, F., Tomida, H., Tsuboi, Y., Tsujimoto, M., Tsunemi, H., Tsuru, T. G., Uchida, H., Uchiyama, H., Uchiyama, Y., Ueda, S., Ueda, Y., Ueno, S., Uno, S., Urry, C. M., Ursino, E., de Vries, C. P., Wada, A., Watanabe, S., Watanabe, T., Werner, N., Wik, D. R., Wilkins, D. R., Williams, B. J., Yamada, S., Yamada, T., Yamaguchi, H., Yamaoka, K., Yamasaki, N. Y., Yamauchi, M., Yamauchi, S., Yaqoob, T., Yatsu, Y., Yonetoku, D., Yoshida, A., Yuasa, T., Zhuravleva, I., and Zoghbi, A. (2018). Hitomi (ASTRO-H) X-ray Astronomy Satellite. *Journal of Astronomical Telescopes, Instruments, and Systems*, 4:021402.
- Tashiro, M. S. (2023). XRISM: X-ray imaging and spectroscopy mission. In *The Sixteenth Marcel Grossmann Meeting. On Recent Developments in Theoretical and Experimental General Relativity*, pages 95–103.
- Veilleux, S. and Osterbrock, D. E. (1987). Spectral classification of emission-line galaxies. *ApJS*, 63:295–310.
- Vogt, F. P. A., Dopita, M. A., Kewley, L. J., Sutherland, R. S., Scharwächter, J., Basurrah, H. M., Ali, A., and Amer, M. A. (2014). Galaxy Emission Line Classification Using Three-dimensional Line Ratio Diagrams. *ApJ*, 793(2):127.
- Wake, D. A., Bundy, K., Diamond-Stanic, A. M., Yan, R., Blanton, M. R., Bershady, M. A., Sánchez-Gallego, J. R., Drory, N., Jones, A., Kauffmann, G., Law, D. R., Li, C., MacDonald, N., Masters, K., Thomas, D., Tinker, J., Weijmans, A.-M., and Brownstein, J. R. (2017). The SDSS-IV MaNGA Sample: Design, Optimization, and Usage Considerations. *AJ*, 154(3):86.
- Walling, R. S. and Weisheit, J. C. (1988). Bound-state excitation in ion-ion collisions. *Phys. Rep.*, 162(1):1–43.
- Weisskopf, M. C., Brinkman, B., Canizares, C., Garmire, G., Murray, S., and Van Speybroeck, L. P. (2002). An Overview of the Performance and Scientific Results from the Chandra X-Ray Observatory. *PASP*, 114(791):1–24.
- Woods, P. (2023). Cloudy. *Nature Astronomy*, 7:1002–1002.
- Yan, R., Bundy, K., Law, D. R., Bershady, M. A., Andrews, B., Cherinka, B., Diamond-Stanic, A. M., Drory, N., MacDonald, N., Sánchez-Gallego, J. R., Thomas, D., Wake, D. A., Weijmans, A.-M., Westfall, K. B., Zhang, K., Aragón-Salamanca, A., Belfiore, F., Bizyaev, D., Blanc, G. A., Blanton, M. R., Brownstein,

- J., Cappellari, M., D'Souza, R., Emsellem, E., Fu, H., Gaulme, P., Graham, M. T., Goddard, D., Gunn, J. E., Harding, P., Jones, A., Kinemuchi, K., Li, C., Li, H., Maiolino, R., Mao, S., Maraston, C., Masters, K., Merrifield, M. R., Oravetz, D., Pan, K., Parejko, J. K., Sanchez, S. F., Schlegel, D., Simmons, A., Thanjavur, K., Tinker, J., Tremonti, C., van den Bosch, R., and Zheng, Z. (2016). SDSS-IV MaNGA IFS Galaxy Survey—Survey Design, Execution, and Initial Data Quality. *AJ*, 152(6):197.
- Yerokhin, V. A. and Shabaev, V. M. (2015). Lamb Shift of $n = 1$ and $n = 2$ States of Hydrogen-like Atoms, $1 \leq Z \leq 110$. *Journal of Physical and Chemical Reference Data*, 44(3):033103.
- Young, P. R., Landi, E., Del Zanna, G., Dere, K. P., and Mason, H. E. (2013). CHIANTI 7.1: a new database release for SDO data analysis. In *SDO-3: Exploring the Network of SDO Science*, page 58.
- Zygelman, B. and Dalgarno, A. (1987). Impact excitation of the $n=2$ fine-structure levels in hydrogenlike ions by protons and electrons. *Phys. Rev. A*, 35(10):4085–4100.

Vita

Chamani M. Gunasekera

Place of Birth:

- Peradeniya, Sri Lanka

Education:

- University of Kentucky, Lexington, KY, USA
M.A. in Physics & Astronomy, Dec. 2021
- College of Saint Benedict & Saint John's University, St. Joseph, MN, USA
B.S. in Physics, May 2017

Professional Positions:

- Graduate Research Assistant, University of Kentucky Fall 2020–Fall 2023
- Graduate Teaching Assistant, University of Kentucky Spring 2018–Spring 2020

Publications & Preprints:

- Gunasekera, C. M., van Hoof, P. A. M., Chatzikos, M., Ferland, G. J. (2023). “The 23.01 release of Cloudy”, *Research Notes of the American Astronomical Society*, 7, 246. doi:10.3847/2515-5172/ad0e75
- Gunasekera, C. M., Ji, X., Chatzikos, M., Yan, R., Ferland, G. J. (2023). “Self-consistent grain depletions and abundances II: Effects on strong-line diagnostics of extragalactic H II regions”, *Monthly Notices of the Royal Astronomical Society*, 520, 4345. doi:10.1093/mnras/stad322
- Gunasekera, C. M., Chatzikos, M., Yan, R., Ferland, G. J. (2022). “Creating a CLOUDY Compatible Database with CHIANTI version 10 Data”, *Astronomy*, 1, 255. doi:10.3390/astronomy1030015
- Gunasekera, C. M., Ji, X., Chatzikos, M., Yan, R., Ferland, G. J. (2022). “Self-consistent grain depletions and abundances I: The Orion Nebula as a test case”, *Monthly Notices of the Royal Astronomical Society*, 512, 2310. doi:10.1093/mnras/stac022